A MICROSCALE CHEMICAL SENSOR PLATFORM FOR ENVIRONMENTAL MONITORING

A Thesis
Presented to
The Academic Faculty

by

Stuart B. Truax

In Partial Fulfillment
of the Requirements for the Degree
Doctor of Philosophy in the
School of Electrical and Computer Engineering

Georgia Institute of Technology
December 2011

A MICROSCALE CHEMICAL SENSOR PLATFORM FOR ENVIRONMENTAL MONITORING

Approved by:

Professor Oliver Brand, Advisor
School of Electrical and Computer Engineering
Georgia Institute of Technology

Professor Jiri Janata
School of Chemistry and Biochemistry
Georgia Institute of Technology

Professor Mark Allen
School of Electrical and Computer Engineering
Georgia Institute of Technology

Professor William Hunt
School of Electrical and Computer Engineering
Georgia Institute of Technology

Professor Bernard Kippelen
School of Electrical and Computer Engineering
Georgia Institute of Technology

Date Approved: 3 August 2011

"A water-clerk need not pass an examination in anything under the sun, but he must have Ability in the abstract and demonstrate it practically."

-Joseph Conrad, from *Lord Jim*

ACKNOWLEDGEMENTS

Many people have contributed their time to the completion of this thesis and the engineering work it describes. I will try my best to acknowledge at least the major contributors, with the stipulation that there are potentially many more I have forgotten or were not aware of.

I thank my advisor, Dr. Oliver Brand, who hosted me in his lab and provided support for this research. I also thank him for allowing me to explore my interests both inside and outside the lab. His persistently positive and supportive attitude has been a boon for me.

I thank my thesis committee: Dr. Mark Allen, Dr. Bernard Kippelen, Dr. Jiri Janata, and Dr. Bill Hunt, for taking the time to read my thesis. Their broad experience was helpful in putting this thesis work in the proper technical context.

I also thank the members of Dr. Brand's lab, both past and present, who provided the tribal knowledge necessary for this thesis work. I thank my predecessor, Jae-Hyeong Seo, who's work on the disk devices provided the basis for the research presented in this thesis. I thank Kemal S. Demirci, who helped me with much of the testing. I thank Luke Beardslee, who helped with the device fabrication during the latter phases of the work. I thank Juan Cesaretti for being a good friend. I also thank Jin-jyh Su, Spyros Pavlidis, Chris Carron, Jonathan Lehmann, Karl Peterson and Kianoush Naeli.

During the completion of this thesis work, I was hosted by several labs for extended stays. Amongst them was the BEL lab under Dr. Andreas Hierlemann of the ETH Zurich. I thank Dr. Hierlemann for his comments, humor, and guidance regarding chemical sensors and the gas manifold system. I also thank Nils Gödecke, Urs Frey, Thomas Lanz, and Jörg Rothe.

I thank Dr. Isabelle Dufour of the IMS lab at the Université Bordeaux 1 for providing theory, intellect, humor, and the motion analysis system used for many of the measurements in this thesis. I also thank Dr. Cedric Ayela and Étienne Lemaire of the same lab.

I thank Dr. Boris Mizaikoff and Yulia Luzinova of the ASR lab for their chemical sensor

knowledge and expertise.

I thank the people, programs and facilities at the Georgia Institute of Technology that helped with this thesis work. I thank the organized intellects of Dr. Minami Yoda, Dr. Andrew Zangwill, and Dr. Jerry Ginsberg for teaching excellent courses. I thank the TI:GER program for exposing me to technology commercialization. I also thank the NRC cleanroom staff for their hard work in providing world-class fabrication facilities.

Lastly, I thank my parents for raising me, and for providing me with wide open spaces in which to grow. Every boy needs to play with dangerous things to know how they can be mastered.

With respect to applying one's own ability, a man from an earlier time said it is better to be impetuous than cautious. There are many who would prefer that I be strictly cautious. However, this austere discipline requires some degree of impetuousness.

TABLE OF CONTENTS

LIST OF TABLES

LIST OF FIGURES

SUMMARY

The objective of this research is to apply micromachined silicon-based resonant gravimetric sensors to the detection of gas-phase volatile organic compounds (VOCs). This is done in two primary tasks: 1) the optimization and application of silicon disk resonators to the detection of gas-phase VOCs, and 2) the development and application of a novel gravimetric-capacitive multisensor platform for the detection of gas-phase VOCs.

In the first task, the design and fabrication of a silicon-based disk resonator structure utilizing an in-plane resonance mode is undertaken. The resonance characteristics of the disk resonator are characterized and optimized. The optimized characteristics include the resonator Q-factor as a function of geometric parameters, and the dynamic displacement of the in-plane resonance mode. The Q-factors of the disk resonators range from 2600 to 4360 at atmosphere for disk silicon thicknesses from 7 μm to 18 μm, respectively. Allan variances range from 1.64×10^{-8} down to 7.25×10^{-9} at atmosphere for resonators with silicon thicknesses from 7 μm to 18 μm, respectively. The in-plane displacement of the in-plane resonance mode is hundreds of nanometers, compared to an out-of-plane displacement of nanometers for the same resonance mode. The resonance frequency of the in-plane resonance mode ranges from 260 kHz up to 750 kHz for disk radii ranging from 200 μm to 130 μm, respectively.

The disk resonators are applied to the sensing of gas-phase VOCs using (poly)isobutylene as a sensitive layer. Limits of detection for benzene, toluene and m-xylene vapors of 5.3 ppm, 1.2 ppm, and 0.6 ppm are respectively obtained. Finally, models for the limits of detection and chemical sensitivity of the resonator structures are developed for the case of the polymer layers used.

In the second task, a silicon-based resonator is combined with a capacitive structure to produce a multisensor structure for the sensing of gas-phase VOCs. Fabrication of the multisensor structure is undertaken, and the sensor is theoretically modeled. The baseline

capacitance of the capacitor component of the multisensor is estimated to be 170 fF. Finally, initial VOC detection results for the capacitive aspect of the sensor are obtained.

CHAPTER I

ENVIRONMENTAL MONITORING AND MICROSCALE CHEMICAL SENSORS

1.1 Introduction

Chemical sensors are becoming increasingly pervasive due to the general technological trend towards a networked and monitored world. The ability to analyze chemical compositions and concentrations has numerous applications, including bio-chemical weapon detection, air quality assurance, industrial process control, medical diagnosis, food inspection, and environmental monitoring [1]. Given the pervasive need for chemical sensing, miniaturized chemical sensors have great economic potential and act as a powerful facilitating technology in these application domains. The advantages of MEMS-based chemical sensors include lower power consumption, reduced size, and the ability to batch-fabricate many sensors at once.

A particular application domain of interest is environmental monitoring, which includes the monitoring of laboratories, workplaces, streams, public spaces, and consumables. A class of pollutants of particular concern in this area is volatile organic compounds (VOCs). The classic trio of benzene, toluene, and xylenes (collectively referred to as BTX) constitute the most widely studied VOCs, and they are widely used as standard test analytes for chemical sensors. BTX belongs to a particular subgroup of VOCs known as aromatic VOCs. Due to their toxic and carcinogenic nature (as in the case of benzene), monitoring for traces of aromatic VOCs is a desired capability.

The ability to unobtrusively place many sensors in critical locations presents numerous advantages, as it enables in-situ sensor networks and comprehensive location-specific monitoring. With these capabilities, present and future environmental monitoring policies can be fully realized. The environmental monitoring application thus suits the characteristics of microfabricated MEMS-based chemical sensors. The following section will examine the

processes and technologies currently employed in environmental monitoring. The section thereafter will describe some of the design considerations in implementing chemical sensors for the environmental monitoring role. Following the outline of design considerations, a literature review encompassing the relevant classes of microscale chemical sensors will be presented with an emphasis on VOC detection. This will then be followed by a discussion of system-level design considerations for multi-transducer systems.

1.2 Environmental Monitoring

Sustainability has become increasingly important in developed countries since the middle of the 20th century. Monitoring of environmental pollutants has consequently been mandated through legislation in the major industrialized nations, including the United States. Airborne VOCs and numerous other airborne pollutants are regulated in the U.S. under the Clean Air Act [2].

Although many organizations give suggested maximum exposure limits of gas-phase VOCs, the U.S. Occupational Safety and Health Administration (OSHA) gives regulatory limits for the maximum time-averaged exposure permissible for a worker over the course of a 40-hour workweek. These maximum exposure limits are called permissible exposure limits (PELs). An even lower limit, the lowest observed adverse effect level (LOAEL), is the minimum vapor exposure level for which adverse health effects are observed in humans. LOAELs are compiled by the U.S. Agency for Toxic Substances and Disease Registry (ATSDR). The PELs and LOAELs give an idea of the specifications a microscale chemical sensor platform would have to meet to be competitive in the monitoring of VOC vapors in a workplace safety application. Both the OSHA PELs and LOAELs for key gas-phase VOCs are summarized in Table 1 [3–5]. In the context of chemical analysis, the vapor of interest is referred to as the *analyte*.

The average concentration of BTX vapors in the ambient environment varies with geographic location. Outdoor city and indoor office environments in the U.S. and other developed countries have average atmospheric concentrations of benzene, toluene, and m/p-xylene on the order of single parts per billion (ppb) [6–9]. In close proximity to petrol

Table 1: OSHA PELs and LOAELs for Gas-Phase VOCs

Analyte	PEL (mg/m^3)	PEL (ppm)	LOAEL (mg/m^3)	LOAEL (ppm)
Benzene	3.2	1	1.7	0.53
Xylenes	435	100	61	14
Toluene	754	200	332	88

Table 2: EPA Maximum Contaminant Levels (MCLs) for VOCs in Drinking Water

Analyte	MCL (mg/L)	MCL (ppb)
Benzene	0.005	6.0
Toluene	1.0	1150
Xylenes (total)	10.0	11627
Trichloroethylene	0.005	3.4
Ethylbenzene	0.7	807
Dichloromethane	0.005	3.7

stations, concentrations of benzene vapor can reach the 10's of pbb [10, 11], and areas with a high density of motor vehicles can have ambient benzene vapor concentrations of 100's of ppb [12]. In this latter case, the ambient benzene vapor concentration approaches the level of a health risk.

The sensing of VOCs is not restricted to VOC vapors. Liquid-phase VOCs pose a threat to water sources. Due to this, environmental monitoring addresses VOC sensing in the both the liquid and gas phases.

In the U.S., the monitoring of waterborne pollutants is standardized and regulated by the Environmental Protection Agency (EPA). The maximum allowable amount of a given contaminant per unit volume of water is referred to as the maximum contaminant level (MCL). Table 2 shows a list of MCLs for some VOCs in drinking water [13]. The MCLs of Table 2 represent the maximum allowable level of a contaminant within a drinking water sample.

To reliably detect contaminants at the limits outlined in Tables 1 and 2, the technical capabilities of the analysis system employed must also be considered. The lowest concentration of an analyte an analysis system can detect is referred to as the limit of detection (LOD). The LOD of the analysis system must be below the limits listed in Tables 1 and

2 in order to conduct a statistically reliable analysis of the sample. This further raises the requirements of the analysis system employed beyond that of simply being able to detect analytes *at* the limits listed.

The current U.S. regulations generally mandate the use of gas chromatography-mass spectrometry (GC/MS) for analysis of drinking water and gas-phase VOC samples. GC/MS is a technique whereby analyte samples are first separated in a chromatographic column and then analyzed using mass spectrometry. Chromatography employs a capillary column to separate an analyte mixture based on the transit time of individual analytes through the column. The subsequent mass spectrometer stage of the system then ionizes the analyte molecules to identify them based on their mass-to-charge ratio. The combination of the two stages allows GC/MS to attain very high selectivities and low limits of detection.

GC/MS systems can attain very low LODs, demonstrating 0.2 pptr (parts per trillion) LODs for gaseous benzene using a preconcentrator unit [14]. However, GC/MS systems are physically large. Both the chromatography and mass spectrometer stages of GC/MS systems are currently difficult to miniaturize, limiting their use to lab-based analyses. Research efforts have been focused on optimizing the sample collection and analysis procedures for GC/MS systems [15, 16] and the miniaturization of GC/MS systems [17].

The procedure for collecting and analyzing gas samples for VOCs illustrates how in-situ microscale chemical sensors could drastically improve the sample analysis process. The sample collection and preparation procedure for workplace VOC vapor analysis is specified by OSHA [18–20] and key aspects are outlined in the following list:

- Samples are collected by flowing the ambient air through sampling tubes with a charcoal matrix. Typically 10 L of air must be passed through the matrix of the collection tube. This must be done at flow rates as low as 50 mL/min, taking up to 4 hours to collect a sample.

- The samples are transported to the lab where the GC/MS analysis is to be carried out. This step carries the risk of changing the concentration of analyte in the collection matrix during transport.

- The samples are extracted from the charcoal collection matrix using carbon disulfide.
- The extracted sample is analyzed using a GC/MS system.

The sample analysis is typically conducted at a commercial or government laboratory. As of this writing, a single GC/MS analysis for a wide spectrum of analytes costs an average of $130 per sample [21]. In-situ microscale sensors could optimize this process, eliminating many steps in the above procedure by conducting the analyses in real-time at the sample collection location. Additionally, in-situ sensors could wirelessly transmit their results from the collection site, possibly eliminating the need for manual sample collection.

An in-situ sensor system would, however, have to compete with the low limits of detection and inherent selectivity of a GC/MS system. GC/MS systems represent the current gold standard of chemical analysis, in terms of their LODs and selectivity. Emerging chemical analysis systems and microsensors thus have to overcome formidable technical barriers to adoption, in addition to many political obstacles. However, there exist many application areas where microsensor technologies do not have to directly compete with GC/MS systems. These include environmental monitoring of unregulated analytes that have high concentration thresholds and do not pose an immediate health risk. It is in these application domains that emerging chemical microsensors can gain an immediate foothold.

The remainder of this thesis focuses on the detection of gas-phase VOCs. In the chemical sensor overview of this chapter, liquid-phase VOCs will be mentioned for the purpose of comparison only. It should be kept in mind that liquid-phase detection limits are often lower than those for gas-phase detection of a given analyte.

1.3 Chemical Sensor Design

A chemical sensor can be decomposed into two components: a chemically sensitive layer, and a transducer. The chemically sensitive layer directly interacts with the analyte that is being sensed. The presence of an analyte will affect a physical change in the sensitive layer (e.g. increasing the density of the sensitive layer). This physical change in the sensitive layer is in turn converted into a signal by the transducer. The transducer output signal

should lend itself to mathematical transformations and storage, and is therefore typically electrical.

In designing a chemical sensor system, the design choices of sensitive layer and transducer offer a range of possible combinations. Each of these combinations must be evaluated using several metrics. These include sensitivity, selectivity, limit of detection, long-term stability, and calibration requirements.

Sensitivity describes the magnitude of the sensor signal per unit of analyte concentration in the analyzed sample. For a given amount of noise, greater sensitivity is preferred in a chemical sensor system.

Selectivity is the ability of a chemical sensor system to detect the analyte of interest while rendering negligible the signals attributed to other analytes and effects. Depending on the application, a sensor with selectivity to a single analyte or single class of analytes is preferred. A sensor may achieve selectivity by producing distinctly different signals corresponding to different analytes. The case should be avoided where a given signal can be attributed to more than one analyte or combination of analytes (i.e. correlated responses).

Limit of detection (LOD) describes the smallest amount of analyte that is reliably detectable by a chemical sensor system. This limit is dependent on the noise in the sensor signal and the sensitivity of the sensor. In order to distinguish a signal produced by an analyte from the signal generated by the sensor's baseline noise, the LOD is typically defined as 3 times the noise-equivalent analyte concentration. High sensitivity paired with low noise yields a low limit of detection, which is desirable.

Long-term stability can describe two aspects of a sensor system's performance. In one sense, it describes the ability of a sensor system to give a constant signal with no underlying change in analyte concentration. Sensor signals can drift due to ambient physical effects such as changes in temperature, pressure, humidity, and the buildup of residues on, or fouling of, the sensor surface. Ideally, the sensor output signal should not change with environmental changes that are not attributable to the presence of an analyte. In another sense, stability refers to the ability of a sensor to keep all of the critical sensor metrics, such as LOD and sensitivity, constant with time. In any sense, long-term stability is necessary

for the proper interpretation of the sensor output signal when operating the sensor for long periods of time.

The *calibration requirements* of a sensor system describe the need to apply extra mathematical transformations to the sensor signal to properly interpret it. For example, chemical sensors with an offset in their output signal must be initially tested to quantify the offset so it can be mathematically removed. Ideally, sensors should have no calibration requirements, as this allows them to be manufactured and put into use without a potentially expensive initial calibration step.

The ideal chemical sensor system gives high sensitivity, high selectivity, a low limit of detection, good long-term stability, and has no need for calibration. While these objectives together may be difficult to achieve in a single device, using many different devices in a single system makes some of these objectives more feasible. By constructing an array of sensors with differing selectivities and sensitivities, and combining the aggregate information from this array, one can increase the analytical power of a sensing system [22]. The array can be composed of devices with differing sensitive layers or different transducers utilizing different transduction principles. The ability to array sensors adds another dimension to the chemical sensor system design space [22].

In summary, the chemical sensor design space allows for choices of sensitive layer and transducer, with the added option of arraying. These choices are undertaken to meet specifications for sensitivity, selectivity, limit of detection, long-term stability, and need for calibration.

1.4 Overview of Chemical Microsensor Technologies

The ability to microfabricate a sensor system places additional constraints on sensor design, as only certain sensor types can be readily microfabricated. In the paragraphs that follow, the different classes of chemical microsensor technologies will be reviewed. Emphasis will be placed on the sensing of VOCs.

1.4.1 Optical Sensors

Optical sensors for chemical detection can be most generally classified into three categories: spectroscopic, interferometric, and surface plasmon resonance (SPR). The most widely used optical techniques are spectroscopic. Spectroscopy relies on the fact that molecules have electromagnetic resonance frequencies in the IR to UV frequency range. By scanning a frequency range and analyzing the absorbed frequencies (absorption spectroscopy) or emitted frequencies (fluorescence spectroscopy), the composition of an analyte sample can be accurately determined due the specific frequencies of molecular vibrations and rotations of the analyte [23]. Since any given analyte adsorbs and emits only certain frequencies of light, unique signals can be obtained for a given analyte. This property imparts an inherent level of selectivity to spectroscopic sensors.

Spectroscopic sensors require a light source that emits the appropriate range of electromagnetic frequencies, a medium to transmit the light to and from the analyte molecules, and a photodetector to collect the spectral response for processing. In practice, and in particular for IR range sensors, this scheme is implemented with a laser light source using a fiber-optic transmission medium and a detector at the opposite end of the medium [24] [25]. In instances where VOC detection has been the goal, a polymer membrane is applied to the transmitting medium (e.g. a waveguide [26]) to adsorb the VOC analytes. The analytes thenceforth sitting in the polymer matrix interact with the evanescent field around the waveguide, generating a unique output spectrum. UV-visible spectroscopy has been applied to detect benzene at concentrations of 15-20 ppb in water and 3-6 ppb in air using a poly-dimethylsiloxane (PDMS) polymer membrane [27]. More recent research using IR sensors has achieved limits of detection for benzene, toluene, and xylenes in the liquid phase of 45 ppb, 80 ppb, and 20 ppb respectively using an ethylene/propylene copolymer (EPCO) membrane [26].

Although spectroscopic approaches yield good limits of detection, there are several drawbacks to this approach. The requirement of a light source places a limit on the minimum size of any given spectroscopic system, as light sources tend to be bulky and not amenable to microfabrication. The use of quantum cascade lasers (QCLs) may solve this problem in

future work [24]. The need for data processing systems to interpret the sensor signal also adds additional bulk to spectroscopic systems.

1.4.2 Calorimetric Sensors

Calorimetric sensors rely on changes of enthalpy to detect an analyte. The process of absorption and desorption of an analyte to and from a polymer membrane generates a heat of condensation or heat of evaporation, respectively, which results in a temperature change that can be measured by a microcalorimeter. Since all the required components can be easily implemented using a CMOS fabrication process, microcalorimeters lend themselves to integration with their readout circuitry [28]. These sensors have demonstrated toluene vapor detection in the 100s of ppm range [29].

Integrated calorimetric sensors typically require two transducers: one without a sensitive layer to act as a reference, and the other with a sensitive layer. This increases the footprint of the sensor and adds to system complexity. Also, calorimetric sensors only produce signals in response to changes in enthalpy. Therefore once the analyte sorption has ceased and the environment is at an equilibrium state, a zero signal results. To obtain an absolute analyte concentration, the sensor signal must be integrated with respect to time.

1.4.3 Gravimetric Sensors

A gravimetric sensor detects mass changes on its surface, thus acting as a miniature "scale" by "weighing" analyte molecules. In the context of chemical sensing, this can be accomplished by chemical binding of the analyte to the sensor surface or sorption of the analyte into a sensitive layer.

Since the addition of mass to the sensor surface has primarily mechanical consequences, gravimetric sensors can be classified according to their mechanical operation mode: resonant vs. static. Using the analogy of a spring-mass harmonic oscillator, resonant sensors output a change in resonance frequency when interacting with an analyte. The addition of the analyte's mass to the resonant structure results in a decrease of the structure's resonance frequency. Static sensors detect added mass through stress-induced deflections of the sensor structure due to interaction with an analyte.

Resonant sensors (also called acoustic sensors) constitute the larger category of gravimetric devices, and come in variations corresponding to the resonant mode shape, frequency, and device geometry employed. Resonant sensors can be classified according to their frequency of operation. High-frequency resonant sensors are generally surface acoustic wave (SAW) devices, thickness shear mode resonators (TSMR), or quartz crystal microbalances (QCMs). These higher-frequency devices typically employ piezoelectric materials in their transduction mechanisms. Lower-frequency resonant sensors come in two main categories: flexural-plate wave devices and resonating cantilevers.

The earliest resonant gravimetric sensor was the quartz crystal microbalance (QCM) developed by Sauerbrey in 1959. The piezoelectric properties of quartz crystals allow them to be used as mechanical resonators, whose resonance frequency can be tracked with electronic circuity. The first reported use of the QCM in a chemical sensing application was by King in 1964 [30]. In Kings study, the QCM was used for the detection of VOCs. In more recent research, QCMs have shown limits of detection of 12 ppm for toluene vapor [31].

SAW devices utilize piezoelectric materials like quartz and ZnO to propagate acoustic waves along the surface of a piezoelectric substrate. The substrate acts as a resonator or delay-line element in an oscillator circuit, whose frequency is tracked. SAW sensors are generally classified according to the wave mode shape that is excited in the substrate [32]. SAW sensors utilizing shear-horizontal mode shapes, where the wave propagates and oscillates parallel to the sensor surface, are ideal candidates for chemical sensing in viscous media [33]. SAW sensors have been applied to liquid-phase detection of VOCs, with liquid-phase limits of detection of 25 ppb for ethylbenzene, 30 ppb for xylenes, and 75 ppb for toluene [34] [35]. In the gas phase, SAW devices have demonstrated limits of detection of 2.1 ppm for n-octane [36].

The chief drawback of the mentioned high-frequency devices is their use of piezoelectric materials. Tools for depositing piezoelectric materials are not a standard feature of CMOS fabrication processes. Therefore CMOS readout circuitry cannot be readily integrated onto the same substrate as the sensors. This in turn results in greater packaging cost due to the need for the packaging to house two separate dies: one for circuitry, one for sensors.

Lower frequency resonant gravimetric chemical sensors are mainly micromachined cantilever structures. In this discussion, cantilever structures are meant to describe beam structures with either one or two fixed ends. Thus, a variety of different structures can be interpreted as being cantilevers, as they can still be mathematically described by classical beam theory (given the proper equivalent parameters). Flexural plate or Lamb wave devices are plate structures with transverse vibration modes, and occupy a smaller portion of the literature.

In comparison to other gravimetric sensors, cantilever-type structures allow a larger degree of engineering flexibility in choice of fabrication materials and actuation schemes, and also allow the possibility of CMOS integration [37].

The cantilever configuration allows operation in a dynamic or static mode. In the dynamic mode of operation, one of the resonance modes of the cantilever is excited and sensed in the same manner as a QCM or SAW sensor, with downward frequency changes corresponding to analyte-induced mass uptake.

A static mode cantilever does not resonate, but merely bends in response to a surface stress increase. This bending is affected by the binding or adsorption of an analyte to the surface of the cantilever, which in turn induces a differential surface stress. The static mode approach can be successfully applied in viscous media, where dynamic mode cantilevers are susceptible to degraded limits of detection due to viscous damping [38] [39]. Static mode cantilevers have demonstrated low limits of detection for certain analytes in specific application domains. Examples include a limit of detection of 20 ppt of TNT [40] and 10 ppb of methylphosphate vapor [41]. Both of these cases involved the use of a single integrated piezoresistor to detect the static bending. This approach however requires significant calibration to appropriately gauge the amount of mass adsorption that has occurred.

Dynamic mode cantilevers are more common than static mode cantilevers in chemical sensing applications, and have demonstrated improved performance in recent years. Higher performance cantilever-based systems often utilize optical actuation and sensing. This is typically implemented by pulse-heating the cantilever at its resonance frequency with a laser and sensing the resulting vibration using reflected laser light. A notable accomplishment in

mass detection is the use of a laser-tracked and actuated silicon carbide cantilever to achieve a mass limit of detection of 7 zeptograms ($7 \times 10^{-21} g$) in vacuum [42]. Concentrations of analytes such as dimethylmethylphosphonate have been sensed with a limit of detection of 20 ppb with electrostatically actuated cantilevers [43], and individual carbon nanotube molecules have been sensed using pairs of optically actuated cantilevers [44]. CMOS integrated cantilevers have been applied to the detection of VOCs in the gas and liquid phases. Notable limits of detection are 2.5 ppm in the gas phase for n-octane [45], and 6 ppm in the liquid phase for xylenes [46].

1.4.4 Electrochemical Sensors

Electrochemical sensors detect charge transport or changes in electrical properties resulting from chemical interactions on the sensor's surface. They can be classified into three categories: potentiometric, voltammetric, and conductometric [47].

Potentiometric sensors detect charge transport between a sensing electrode and a reference electrode. The charge transport is caused by ionic reactions, and is related to the concentration of the ionic analyte by the Nernst equation. Ion selective electrodes (ISEs) represent an implementation of this concept typically used for aqueous solutions. ISEs are readily integrable with CMOS electronics, but thus far have only been used to sense ionic analytes and to make pH determinations of ionic solutions.

Voltammetric devices are an extension of potentiometric devices in that they use three electrodes: two electrodes to maintain a controlled potential in the sample solution, and a sensing electrode to measure charge transport. Using this method, benzene in the gas phase has been detected at concentrations of 1 ppm [48]. However, due to the constraints imposed by the oxidation potentials of the sample solution, oftentimes non-CMOS metals such as Pt, Pd, and Au must be used as electrode materials.

Conductometric sensors return to the two electrode configuration. In this case, changes in the electrical properties of an intervening chemically sensitive layer are detected as a result of analyte interaction. The change detected can be a capacitive change (i.e. a change in the dielectric constant of the sensing layer) or a resistive change (i.e. a change in the

resistance of the sensing layer). An example of a conductometric sensor is the ChemFET, in which the transistor gate of a MOSFET device is replaced by a chemically sensitive gate material to detect ionic reactions. Ionic reactions modulate the resistance of the channel region, allowing a correlation between the channel resistance and the concentration of the ionic reactants.

Capacitive sensors consist of a capacitor with a chemically sensitive material acting as the dielectric layer. By detecting dielectric changes in polymers such as (poly)etherurethane (PEUT) and (poly)epichlorohydrin (PECH), CMOS integrated capacitive sensors have been applied to the detection of VOCs in the gas phase [37] [49], with limits of detection of 61 ppm for toluene and 142 ppm for benzene being reported [50]. However, the relatively high dielectric constant of water makes the application of these sensors in humid or aqueous environments challenging.

Resistive sensors utilize a chemically sensitive layer as a resistive element, and measure changes in the sensitive layer's resistance. Resistive sensors using metal-oxide sensitive layers have been produced commercially [51]. These devices usually require microhotplates to achieve temperatures above 200 $^{\circ}C$ to oxidize the target analyte species. Room temperature approaches using conducting polymers and carbon-black-based sensitive layers have been used to detect VOCs, but the detectable concentrations are relatively high, with 1 part per thousand of benzene vapor being reported [52]. Resistive sensors have the ability to be packed into dense arrays [53].

1.4.5 Limits of Detections for Various Volatile Organic Compounds

The chemical sensor types described in the previous sections have differing limits of detection for the key VOCs. These LODs are summarized in Table 3. The lowest limits of detection are achieved by GC/MS systems, and they represent the gold standard of chemical sensing. After GC/MS, spectroscopic methods claim low LODs for some VOC analytes in the gas and liquid phases. Gravimetric methods occupy the middle-range, claiming low-ppb LODs for liquid phase VOCs and low ppm LODs for gas phase VOCs. Voltammetric, capacitive, and calorimetric methods occupy the upper range of LODs for VOCs as of this writing.

Table 3: Limits of Detection for Various VOCs by Sensing Method

Method	Analyte	Material Phase	LOD	Source
GC/MS	benzene	Gas	0.2 pptr	[14]
UV-Visible Spectroscopy	benzene	Gas	3-6 ppb	[27]
UV-Visible Spectroscopy	benzene	Liquid	15-20 ppb	[27]
Surface Acoustic Wave	ethylbenzene	Liquid	25 ppb	[34, 35]
IR Spectroscopy	benzene	Liquid	45 ppb	[26]
Voltammetric	benzene	Gas	1 ppm	[48]
Surface Acoustic Wave	n-octane	Gas	2.1 ppm	[36]
Resonant Silicon Cantilever	n-octane	Gas	2.5 ppm	[45]
Resonant Silicon Cantilever	xylenes	Liquid	6 ppm	[46]
Quartz-crystal Microbalance	toluene	Gas	12 ppm	[31]
Capacitive	toluene	Gas	61 ppm	[50]
Calorimetric	toluene	Gas	100 ppm	[29]

1.5 Arrays and Multisensor Systems

By using multiple sensors in an array, each with a different sensitive layer or inherent sensitivity to a different analyte, the ability to analyze samples containing mixtures of analytes can be achieved. Sensor arrays and systems that act in this capacity are often referred to as electronic noses [54].

The design of multisensor arrays must be tailored to the sensing task. Individual sensor responses should differ significantly for exposure to a given analyte, as correlated responses yield no additional information and negate the advantage of using an array. The difference in sensor responses can be achieved by using a single sensor type with different sensing layers, or by using different sensor types.

A multisensor system should seek to achieve an orthogonality property. That is, if each sensor response lies along a basis vector in a vector space, the vectors should be orthogonal. Orthogonality is desired provided that the sensor responses are not disruptively noisy and are relevant to the presence of the analyte [22]. When a system possessing the orthogonality property is used, mixtures can be analyzed. The resulting data can be analyzed using principal components analysis (PCA) to determine the sample composition down to the concentrations of individual analytes in the mixture. The individual characteristics of each sensor and sensing layer in an array can be tuned to optimize array performance, adding

another layer of complexity to system design. Additional array design considerations include using both broadly and narrowly tuned sensors to achieve better system performance [55]. Arrays of SAW devices individually coated with different polymers have been shown to distinguish 4 component mixtures of VOCs using 4 sensors [56]. Binary mixtures of VOCs have also been analyzed using microcantilever arrays [45].

When implementing array-based systems on the microscale, CMOS fabrication processes can be leveraged to created integrated arrays with a small footprint. Microsensor arrays utilizing gravimetric, calorimetric, and capacitive sensors for VOC sensing have been demonstrated using a CMOS process [28] [57]. This approach allows for low-cost, batch fabricated multisensor systems to be fabricated on a single chip, bringing the commercial applications of microsensor arrays much closer. Non-CMOS integrated approaches using gravimetric and optical sensors [58] as well as a dual gravimetric and resistive sensor combinations [59] have also been applied to VOC detection. Multisensor array approaches have been found to achieve their best results when employing 5 transducers in an array [60].

1.6 Outline of Thesis

In this work, a micromachined silicon-based resonant gravimetric chemical sensor platform is applied toward the gas-phase detection of VOCs. The silicon-based resonant gravimetric sensor technology is then expanded by adding a capacitive sensing capability. The resulting gravimetric-capacitive multisensor is then applied towards the sensing of VOC vapors.

Chapter 2 describes the basic theory of resonant gravimetric chemical sensing, and presents a silicon-micromachined disk resonator. Chapter 2 also describes the basic physical parameters of this resonator along with its fabrication process.

Chapter 3 presents the physical characterization of the silicon disk resonator. The resonator Q-factor is analyzed by examining the various energy loss mechanisms of the resonator, and the deflection of the resonator while resonating in its rotational in-plane resonance mode is also examined.

Chapter 4 presents the performance of the silicon disk resonator in the VOC sensing role. The effect of the polymer sensing layer applied to the disk resonator is quantified in

terms of Q-factor and Allan variance. Measured and theoretical values for the limits of detection and chemical sensitivity of the disk resonator are obtained. Limits of detection for benzene, toluene, and m-xylene vapors are also presented.

Chapter 5 presents a gravimetric-capacitive multisensor platform, exploring the possibilities of multisensor design incorporating resonant gravimetric and capacitive sensing mechanisms. A silicon resonator with a capacitor structure implemented on its surface is modeled and fabricated. The capacitive aspect of the structure is then applied to the sensing of toluene and ethanol vapors.

Chapter 6 presents conclusions and outlooks in the context of gas-phase VOC sensing for both the silicon disk resonator and the gravimetric-capacitive multisensor device presented in this research.

CHAPTER II

RESONANT GRAVIMETRIC SENSING AND DISK RESONATORS

2.1 Introduction

Micromechanical resonators are used in a wide variety of applications. Examples include microfabricated mass sensors [42], chemical and biochemical sensors [45, 61–63], frequency filters, and gyroscopes [64, 65]. Micromechanical resonators have also found large-scale commercial application as accelerometers [66] and pressure sensors [67].

It is through mass-sensing that mechanical resonators can be used as chemical sensors. Chemical analytes can induce an effective mass change of a resonator through physical contact with the resonator structure. A change in the effective mass of a resonant structure produces a change in its resonance frequency, which can be easily tracked with the aid of simple readout circuitry.

This chapter will describe the basic theory of mass-sensing using mechanical resonator structures. The silicon disk resonators used in this research will then be presented, including details about their design, dynamic operation, and fabrication.

2.2 Theory of Resonant Gravimetric Sensing

Mechanical resonance arises from the oscillatory exchange of potential energy (elastic strain) and kinetic energy (momentum) within a mechanical structure. The capacity to store these two types of energy is quantified by the effective stiffness K and effective mass M of the structure. When a time-varying mechanical force $F(t)$ is applied to the structure, the transferred energy will periodically oscillate between potential and kinetic forms within the structure. This is observed as an oscillating displacement, called a vibrational resonance, along a given direction x, called the degree of freedom. This behavior is described by the 2nd-order differential equation of the form [68]

$$M\ddot{x} + D\dot{x} + Kx = F(t) \tag{1}$$

The D term accounts for the energy loss (damping) that occurs during oscillation, which leads to a decrease in the oscillation amplitude with time when the system is unexcited by an external force.

The time-varying mechanical force $F(t)$ can be described as a sum of sinusoids, allowing its transformation into the frequency domain by a Fourier transform. Thus, it becomes useful to analyze (1) in terms of its equivalent transfer function in the frequency domain [68]

$$X = \frac{F}{K + Di\omega - M\omega^2} \tag{2}$$

In this equation, F and X are complex amplitudes and ω is a radial frequency. The form of the transfer function implies that the vibration amplitude X will be maximized at a given excitation frequency ω_o. This frequency is the resonance frequency for the one degree-of-freedom system, and, neglecting damping effects, has the form

$$\omega_o = 2\pi f_o = \sqrt{\frac{K}{M}}. \tag{3}$$

The above equations can be applied to systems with multiple degrees of freedom to obtain a better description of real-world resonant structures. When analyzing a system with multiple degrees of freedom, the values of M, K and D are put into matrix form to represent the effective values of each parameter for each degree of freedom, and the coupling that occurs between the degrees of freedom. With this extension, resonant structures can be seen to have multiple resonance frequencies, each with a corresponding vibrational mode shape. Finite element modeling (FEM) is a useful tool for performing analyses of these vibration modes (modal analyses).

For the application of gravimetric sensing, any addition of mass to the resonant system will result in a reduction of the resonance frequency (by (3)). This change in resonance frequency due to the addition of mass can be quantified with the following equation

$$\frac{\Delta f}{f_o} = -\frac{1}{2}\frac{\Delta M}{M} \tag{4}$$

In (4), Δf and ΔM are the differential changes in resonance frequency and effective

mass, respectively. Thus, the basic framework for applying resonant systems as mass sensors is established. The general field of mass-sensing is referred to as gravimetry, and resonant sensors occupy this field alongside other sensor types.

In the chemical sensing application, sensing of a chemical analyte with a resonant sensor is generally facilitated by a sensing layer that is applied to the sensor surface. The analyte will attach or diffuse into the sensing layer to change the overall density of the sensing layer. The process by which the chemical analyte interacts with this layer in this research is discussed in Chapter 4. A general expression for the chemical sensitivity S of a resonant gravimetric sensor is [45, 69]

$$S = \frac{\delta f}{\delta c} = \frac{\delta f}{\delta \rho_L} \frac{\delta \rho_L}{\delta c} = G \cdot S_A, \tag{5}$$

where c is the concentration of the chemical analyte, ρ_L is the density of the sensing layer, and f is the resonance frequency of the structure. G can be seen as the transducer-dependent component of the chemical sensitivity and S_A is the sensing-layer dependent component of the chemical sensitivity. If the analyte concentration is given in units of ppm, then S has units of Hz/ppm, G has units of Hz/(kg/m^3), and S_A has units of (kg/m^3)/ppm.

To track the changes in resonance frequency of a mechanical resonator, the resonator is placed into an oscillator circuit like that pictured in Figure 1. The resonance frequency of the resonator determines the oscillation frequency of the loop by filtering out the off-resonance signals within the loop. Thus, the loop signal converges in frequency to the resonance frequency of the resonator. When the Barkhausen criterion is satisfied, the oscillator loop signal reaches a steady-state oscillation. Transduction mechanisms must be used to convert the electrical loop signal into the mechanical vibrations within the resonator structure, and vice versa. Examples of such transduction mechanisms include piezoresistive, piezoelectric, and electrostatic transduction mechanisms.

The minimum frequency shift from mass addition that can be measured is determined by the frequency noise Δf_{noise}. A general expression for this frequency noise is given by [70]

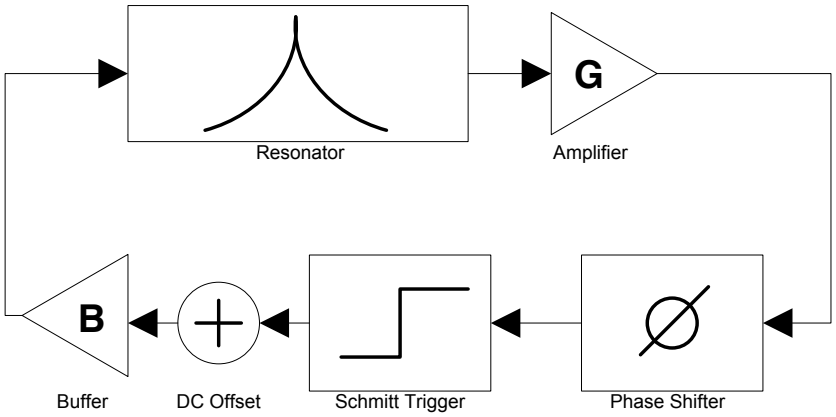

Figure 1: A block diagram for the oscillator circuit used in this research.

$$\Delta f_{noise} \approx \frac{f_o \delta\theta}{2Q}, \tag{6}$$

where $\delta\theta$ is the phase noise introduced to the loop signal by the amplifier, and Q is the Q-factor of the resonator. The Q-factor is given by

$$Q = \frac{\sqrt{MK}}{D} = \frac{f_o}{\Delta f_{-3dB}}, \tag{7}$$

where Δf_{-3dB} is the frequency bandwidth around resonance where the vibration amplitude is at least $\frac{1}{\sqrt{2}}$ times its value at resonance. The Q-factor is inversely proportional to the amount of energy loss occurring in the resonator during an oscillation cycle. Given its role in (6), it is important to maximize the Q of the resonator structure for the purpose of high-resolution gravimetric sensing. A further analysis of the resonator Q-factor is given in Chapter 3.

Given that the system noise and chemical sensitivity has been defined, an expression for the limit of detection of the sensor system can be introduced. When referring to the overall sensor system, the combination of the sensing layer, resonator, and feedback loop is implied. The limit of detection is the minimum amount of analyte which can be reliably sensed with the sensor system, and is defined as

$$LOD = 3\frac{\Delta f_{noise}}{S}. \tag{8}$$

This metric ultimately defines the effectiveness of the chemical sensor system, and is further explored in Chapter 4. The discussion now turns to the particular resonant sensors used in this research: silicon micromachined disk resonators.

2.3 Engineering Considerations for Micromachined Resonant Chemical Sensors

Before the silicon disk resonators are fully introduced, some basic motivating engineering constraints must first be considered. These constraints determine the resonance mode and transduction schemes that are employed in the disk resonator structures used in this research.

Mass-sensing resonators are often employed in viscous media such as gases or liquids, and the energy loss from viscous damping can significantly reduce the resonator Q-factor, in turn reducing the mass resolution of the sensor. The resonance mode of the sensor can be altered to reduce this effect. An example is the use of in-plane resonance modes as opposed to out-of-plane resonance modes to eliminate normal stresses on the resonator surface from the surrounding fluid [33, 71].

The presence of viscous media also dictates the actuation scheme used to sustain oscillation. Electrostatic actuation uses the force generated by electric fields acting on charged electrodes to sustain oscillation. This scheme often requires sub-micron gaps between the driving electrodes, creating the possibility of energy loss due to squeeze-film damping. Electrostatic actuation of silicon cantilever structures with integrated CMOS readout circuity has been demonstrated in chemical sensor applications in the gas phase [43]. However, application of these structures in the liquid phase is challenging due to the squeeze-film damping effect and the high dielectric constant of water.

Electrothermal actuation uses a temperature gradient or the bimorph effect to create a mechanical deflection. This technique is advantageous in that the required heat source can be implemented by an integrated resistor, which is part of the bulk sensor structure.

This transduction mechanism has been demonstrated to actuate resonators with resonance frequencies in the GHz range [72], and is easily implemented in silicon using standard CMOS doping processes. Silicon cantilever resonators with integrated readout circuitry using electrothermal excitation have been demonstrated in the detection of VOCs in the gas phase [45, 46].

Therefore, the disk resonators presented here combine three distinct features: 1) the use of a rotational in-plane resonance mode to reduce viscous damping, 2) the use of electrothermal actuation and piezoresistive sensing elements, and 3) a CMOS-compatible silicon fabrication process.

2.4 Disk Resonator Design

The chemical sensor system studied in this research uses a silicon-based disk resonator vibrating in a rotational in-plane resonance mode. Figure 2 shows an SEM micrograph of a fabricated disk resonator. The relevant geometrical parameters of the fabricated resonator structure are shown Figure 3. The silicon disk structure is suspended by two anchor beams each measuring 250 μm lengthwise. The half-disks have radii that vary between 100 and 200 μm. There is a 20 μm gap between the half-disks and the central anchor beam. Table 4 lists the range of values for each geometric parameter of the disk resonators fabricated in this research.

Viscous damping of this resonator structure has been reduced through the use of a rotational in-plane resonance mode. Cantilever structures typically use out-of-plane resonance modes, and silicon-based cantilevers of this type have Q-factors at most on the order of 1500 in air [73]. The Q-factor limit of cantilevers is a result of energy loss to normal stresses from the surrounding fluid media. These normal stresses from fluid media are prevalent in out-of-plane resonance modes. In-plane resonance modes help to eliminate these normal stresses. The disk resonators used in this research have previously been shown to achieve Q-factors of 5800 in air for a device with a 10 μm silicon thickness [71].

The rotational in-plane resonance mode constitutes a small-angle rotation of the half-disks about the disk center. The resonance frequency of this mode is determined primarily

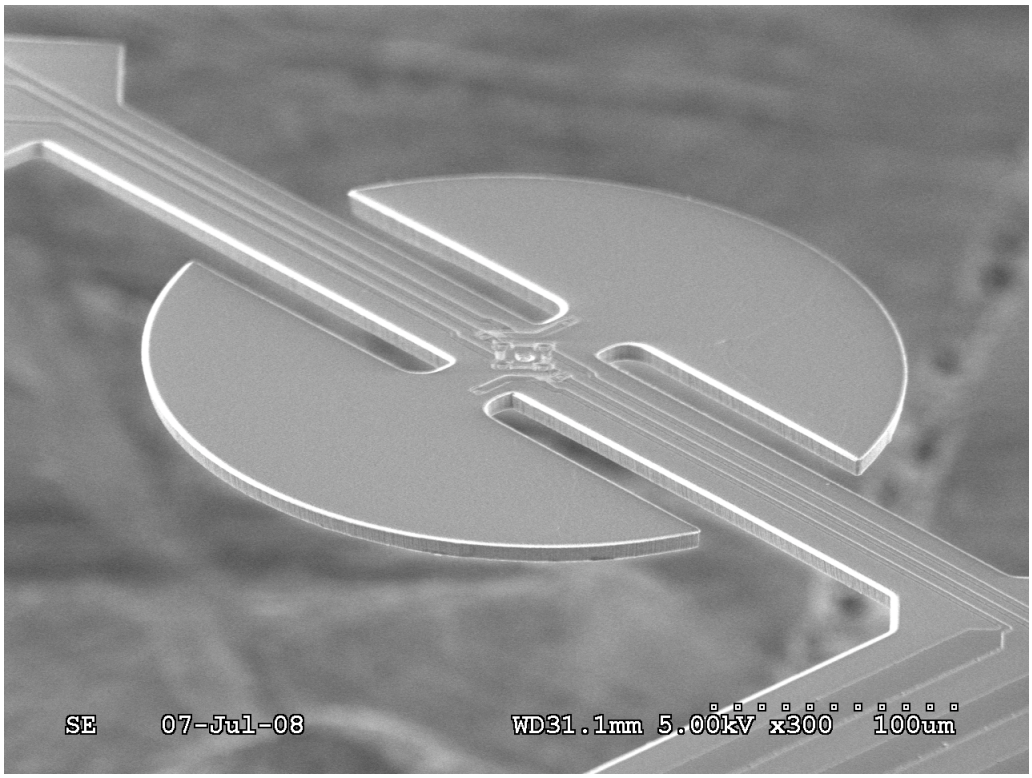

Figure 2: SEM micrograph of a resonator used in this research. The disk radius is 150 μm.

by the radius of the half-disks and the dimensions of the support beams. The resonance frequency of the rotational in-plane mode is shown as a function of disk radius in Figure 4. To a first order, the resonance frequency of the in-plane mode is not dependent on the silicon thickness t_{Si}. In Figure 4, the measured resonance frequency of the rotational in-plane resonance mode is identical for resonators with the same disk radius but different silicon thicknesses. The resonance frequency of the in-plane rotational mode has a $\frac{1}{r_o^2}$ dependence when the support beam dimensions are kept constant, as in Figure 4. When the thickness of the resonator's silicon and the dielectric layers are comparable (see Disk Resonator Fabrication), the overall device thickness will begin to affect the resonance frequency of the rotational in-plane resonance mode. Figure 5 shows a FEM simulation of the rotational in-plane resonance mode.

The gap distance between the half-disks and the central anchor beam was chosen to be 20 μm, which reduces the squeeze-film damping typically occurring in oscillating gaps. The

Table 4: Physical Parameters for the Disk Resonators

Parameter	Description	Value(s)
t_{Si}	Resonator silicon thickness	7 or 18 μm
w	Width of clamped-clamped anchor beam	45 μm
L	Length of clamped-clamped anchor beam	500 μm
g	Width of gap between half-disk and anchor beam	20 μm
b	Width of half-disk bridge beam	32 μm
r_o	Radius of half-disks	100-200 μm
f_{ip}	Resonance frequencies of in-plane mode	270 kHz - 1.3 MHz

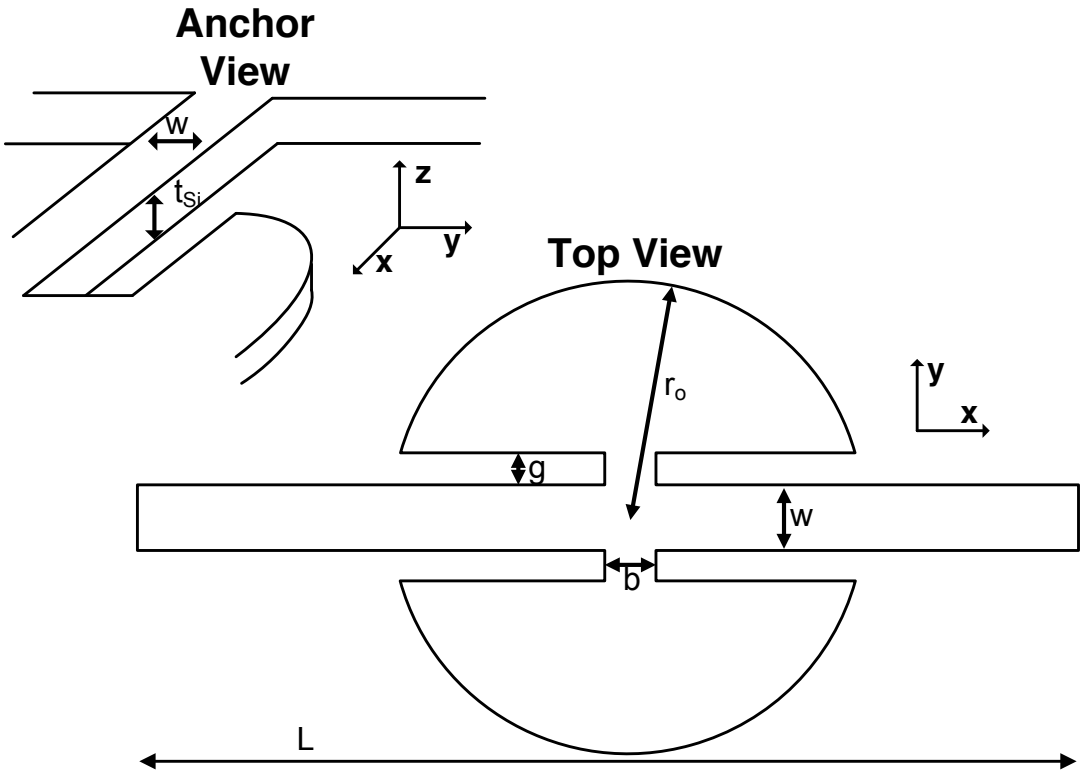

Figure 3: Geometry of the disk resonators used in this research. Relevant geometric parameters are shown.

squeeze-film damping associated with electrostatic excitation is also avoided through the use of an integrated electrothermal excitation scheme. Two integrated heating resistors at the center of the resonator structure are excited with a sinusoidal voltage superimposed on a DC voltage. The resulting sinusoidal heating of the bulk silicon near the resistors causes an in-plane deformation of the half-disks due to the bimorph effect.

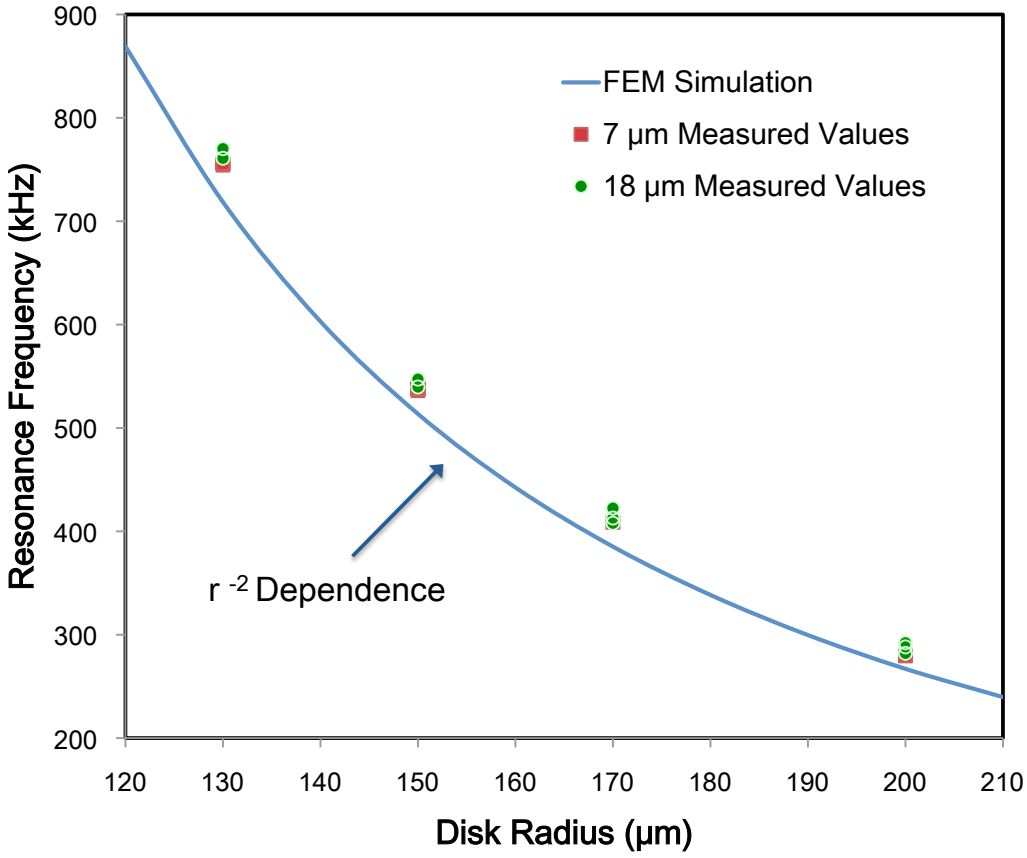

Figure 4: Resonance frequency of the rotational in-plane mode as function of disk radius r_o. The measured values are from disk resonators with $t_{Si} = 7\mu$m and $t_{Si} = 18\mu$m. The simulated values are from disk resonators with $t_{Si} = 7\mu$m. To a first order, the silicon thickness has no effect on the rotational in-plane resonance frequency.

The deformation of the resonator structure is sensed through a Wheatstone bridge configuration of piezoresistors located at the center of the structure [71, 74]. The piezoresistors that constitute the Wheatstone bridge undergo a differential change in resistance proportional to the mechanical strain occurring at the center of the resonator. The Wheatstone bridge output gives a voltage signal proportional to this strain with minimal offset, hence reducing the complexity of signal readout. The piezoresistors are implemented in the same doping step as the excitation resistors.

Figure 6 shows the equivalent circuit diagram of the excitation and Wheatstone bridge resistors along with a SEM image of their implementation in a fabricated disk resonator.

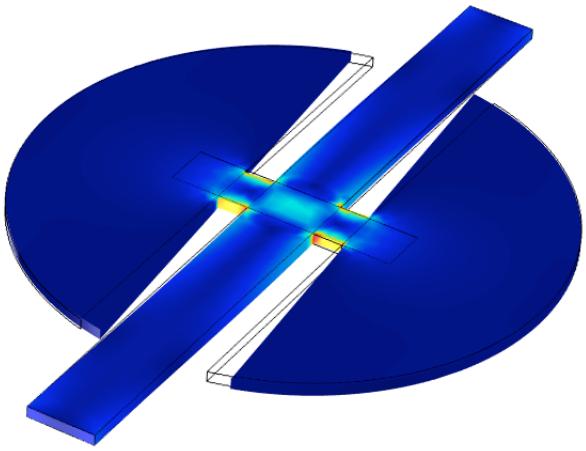

Figure 5: FEM simulation of the deflection from the rotational in-plane resonance mode of the disk resonators used in this research. Coloring is of the Von Mises stress distribution arising from this mode.

A DC bias is applied to the Wheatstone bridge through the V_{cc} and GND ports. The excitation resistors are each given separate AC sinusoidal signals through ports $EX+$ and $EX-$. $EX+$ and $EX-$ have a DC offset from either V_{cc} or GND, respectively [74].

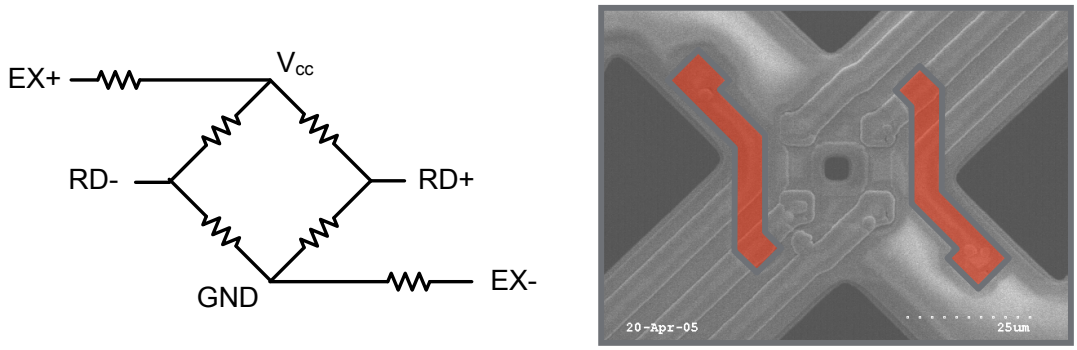

Figure 6: Equivalent circuit of the piezoresistive Wheatstone bridge and excitation resistors (left) and a SEM image of the same on a fabricated disk resonator (right). In the SEM image, the highlighted red areas are the excitation resistors and the Wheatstone bridge is located around the hole at center.

Due to the specific placement of the electrothermal excitation and piezoresistive sensing

resistors, the resonator's piezoresistive transfer characteristic shows a high sensitivity to the rotational in-plane resonance mode relative to the out-of-plane resonance modes. Figure 7 shows the out-of-plane deflection of the tip of a half-disk on a disk resonator, along with the piezoresistive transfer characteristic. The out-of-plane deflection was obtained through laser vibrometry, the details of which are outlined in Chapter 3. The piezoresistive transfer characteristic was obtained through measurement with a network analyzer, using only the excitation and sensing elements on the disk resonator. The disk resonator has a radius of 170 μm and a silicon thickness of 18 μm. With this device, the rotational in-plane mode occurs around 413 kHz. The data shows an out-of-plane deflection at this frequency of only a few nm/V whilst showing a strong piezoresistive response. The existence of the rotational in-plane mode is directly confirmed through a stroboscopic measurement of this same device in Chapter 3.

To sustain oscillation, the input and output ports of the resonator are connected to an amplifying feedback loop like that shown in Figure 1 [74,75]. The Wheatstone bridge output is first amplified and phase-shifted before being rectified and fed back into the excitation elements of the resonator. The initial amplification and phase-shifting are necessary to fulfill the Barkhausen criterion for sustained oscillation. In this research, this system is implemented with discrete circuit elements arranged on a printed-circuit board, shown in Figure 8. The loop oscillation frequency is read by a frequency counter (Agilent-53131A). A gate time of 1 second is used for all frequency measurements of the system.

2.5 Disk Resonator Fabrication

The resonator structures are fabricated using a bulk micromachining technique compatible with standard CMOS fabrication steps, and is adapted from [71,74]. The base substrate for the devices are 500 μm thick, (100) silicon wafers with a diameter of 100 mm. The wafers have an epitaxially-grown phosphorous-doped layer on their surface which is specified to various thicknesses, ranging from 7 μm to 18 μm.

The wafers are thermally oxidized at 1050°C to form a 1 μm thick layer of silicon dioxide on the silicon wafer. Subsequently, reactive ion etching (RIE) is used to form diffusion

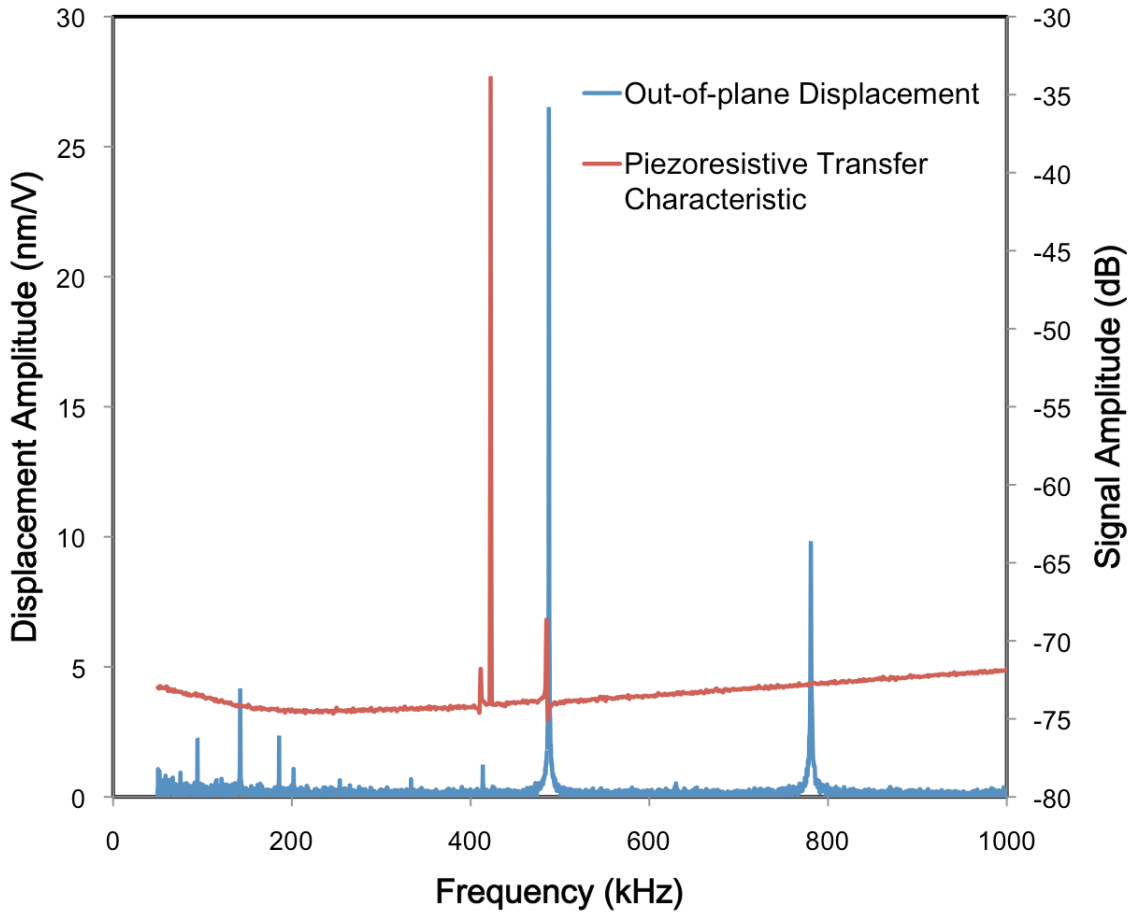

Figure 7: Out-of-plane displacement at the half-disk tip and piezoresistive transfer characteristic of the disk resonator. The peak in the piezoresistive transfer characteristic corresponds to the rotational in-plane resonance mode at 413 kHz. The out-of-plane displacement was measured using laser vibrometry. The device dimensions are $t_{Si} = 18\mu$m and $r_o = 170\mu$m.

windows in the thermally grown oxide. The exposed silicon areas are doped with boron to achieve a p-type carrier density of approximately $1\text{x}10^{19}$ cm^{-3} to form the Wheatstone bridge and excitation resistor areas. A wet oxidation for 1 hour at 1000°C is then carried out to cover the doped areas with silicon dioxide and to simultaneously drive-in the p-type resistors. Contact openings are then etched using RIE. Aluminum traces are then sputtered onto the substrate and patterned to electrically connect the resistor areas. Ohmic contacts between the aluminum traces and doped resistor areas are created through sintering. Plasma-enhanced chemical vapor deposition (PECVD) is then used to deposit 0.4

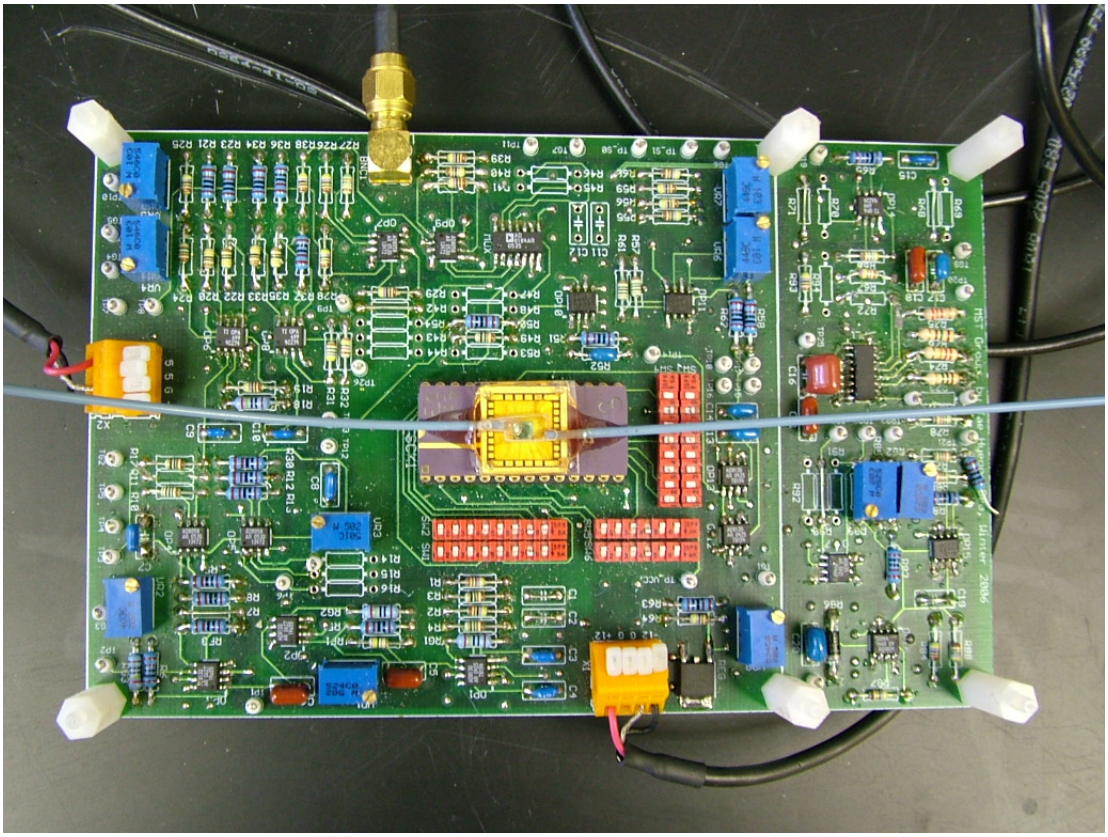

Figure 8: The PCB implementation of the amplifying feedback loop used in this research. Resonator chip is shown at center.

μm of silicon nitride and 0.4 μm of silicon dioxide to protect the aluminum traces from long-term atmospheric oxidation.

The PECVD dielectric layers are then etched with RIE to expose the silicon substrate, defining the shape of the final resonator structures. Etch windows are created on the down-facing side of the wafer to expose the bulk silicon on the back of the wafer. The wafer is then placed in a KOH bath to etch through the bulk silicon from the wafer backside. An electrochemical etch-stop technique is applied to stop the etching at the pn-junction between the n-type epitaxial layer and the p-type substrate. In this way, the epitaxial layer thickness determines the thickness of the final resonator structure. After the KOH etching step, a large (1.5 mm x 2 mm) membrane containing the resonator structures remains suspended by the bulk substrate. A final RIE etching of this membrane releases the freestanding resonator structures and the wafers are cut into dies using a dicing saw.

The fabrication process profile is shown in Figure 9. The fabrication process steps are enumerated in the following list:

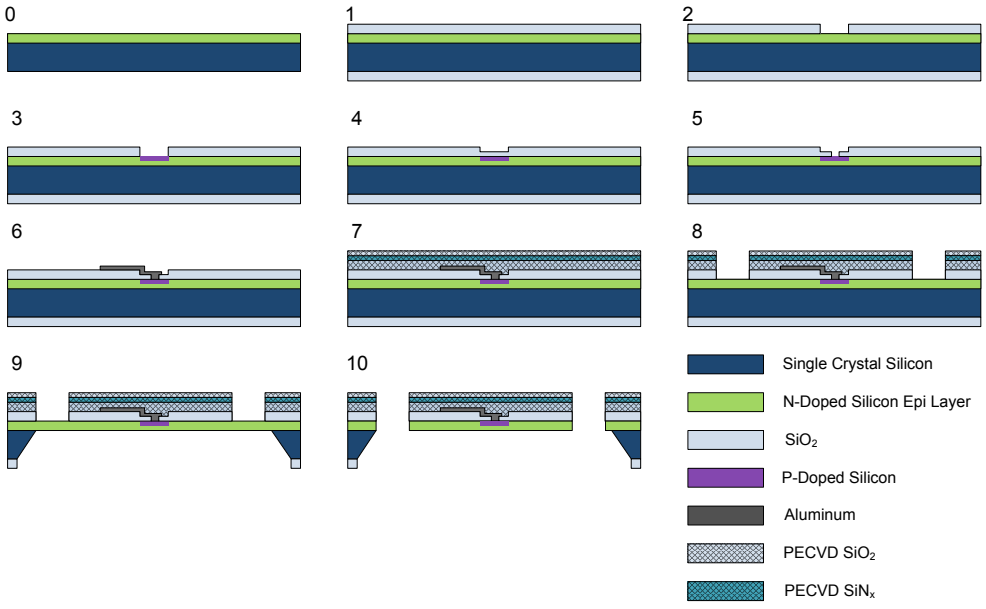

Figure 9: Fabrication process profile.

1. A 1 μm thick layer of wet thermal oxide is grown on a (001) silicon epi-wafer.

2. The thermal oxide layer is etched by an reactive ion etcher (RIE) to expose the bare silicon beneath.

3. P-doping using a solid boron diffusion source is performed using thermal diffusion. This step implements the excitation and Wheatstone bridge resistors. The end surface carrier density is approximately $1\text{x}10^{19} cm^{-3}$.

4. A thin layer of dry and wet thermal oxide is grown to cover the doped areas and simultaneously drive-in the doped resistors.

5. Contact openings are etched using an RIE etch.

6. A 7000 $\mathring{A}$ thick layer of aluminum is sputtered, patterned, and etched to produce the metal lines which connect the doped resistors. Ohmic contacts are created through sintering.

7. PECVD oxide and low-stress nitride layers are deposited for passivation purposes. Each dielectric layer is roughly 4000 $\mathring{A}$ thick. Total dielectric thickness is typically around 1-2 μm, including the thermal oxide.

8. A reactive ion etch (RIE) of the oxide and nitride layers is used to define the resonator structures by etching through the PECVD layers and thermal oxide down to the silicon.

9. Backside etch windows are created by RIE. KOH wet etching is used to selectively etch through the wafer. An electric potential is applied to the KOH solution and the wafer so that the KOH etch terminates at the edge of the epitaxial layer. The thickness of the epitaxial layer therefore determines the resonator thickness.

10. RIE silicon etching is used to release the resonators by etching through the epitaxial layer.

2.6 Chapter Summary

This chapter introduced the basic theory of resonant gravimetric chemical sensing. The important metrics of chemical sensitivity and limit of detection were presented. The design of the silicon disk resonator, its rotational in-plane resonance mode, its transduction mechanisms, and its associated fabrication process were also presented. The characterization of the disk resonator will be discussed in Chapter 3, and its application as a gas-phase chemical sensor will be presented in Chapter 4.

CHAPTER III

PHYSICAL CHARACTERIZATION OF THE DISK RESONATOR

3.1 Introduction

In this chapter, the physical characterization of the disk resonator is presented. The main parameter of interest, Q-factor, and it relation to frequency noise will be described. The functional dependence of the Q-factor on the design parameters of the disk resonator will then be explored. The key loss mechanisms of viscous damping and anchor loss will then be quantified for the disk resonator. To put the viscous damping of the disk resonator in perspective, viscous damping will be examined with respect to cantilever structures also using in-plane resonance modes. Lastly, physical measurements of the deflection of the disk resonator structure while operating in its rotational in-plane resonance mode will be presented.

3.2 The Theory of Q-factor and Frequency Noise

3.2.1 Q-factor and Energy Loss

Resonant structures are pervasive in nature. The nature of resonance lies in the oscillatory exchange of energy from potential to kinetic forms. Mechanical resonators store potential energy through their elasticity, and kinetic energy through their momentum. During steady-state oscillation, the energy provided to excite a resonant structure dissipates through various mechanisms. Under the assumptions of linear vibration, the resonator Q-factor quantifies this energy dissipation as a ratio of energy stored per oscillation cycle to energy dissipated per oscillation cycle [68]

$$Q = 2\pi \frac{E_{Stored}}{E_{Dissipated}} \tag{9}$$

At steady-state oscillation, the power-balance theorem states that the amount of energy put into the resonant system during an oscillation cycle must be the exact amount of energy dissipated during that oscillation cycle [68]. The total Q-factor can be decomposed

by using an inverse sum, which provides a convenient way of expressing the contribution of the various energy dissipation mechanisms of the resonant system. A general form of this sum for micromechanical resonators is

$$\frac{1}{Q} = \frac{1}{Q_{viscous}} + \frac{1}{Q_{anchor}} + \frac{1}{Q_{internal}} \tag{10}$$

In (10), the $\frac{1}{Q_{viscous}}$, $\frac{1}{Q_{anchor}}$, and $\frac{1}{Q_{internal}}$ terms describe the inverse Q-factors associated with viscous damping, anchor loss, and internal damping, respectively. The inverse form of (10) is convenient because the terms are *proportional* to the amount of energy loss from each mechanism. For achieving high Q-factors, it is hence desirable that these terms be small. The largest term will limit the total Q-factor.

The terms of (10) describe the energy loss mechanisms most often considered for micromechanical resonators. Viscous damping is the energy loss attributable to interactions with viscous media. Anchor loss arises from the propagation of elastic waves from the resonator into its support structures. Internal damping includes the effect of thermoelastic damping, and arises from the material-dependent internal friction of the resonator [76].

Frequency noise is shown to have a $\frac{1}{Q}$ dependence [70, 77–79]. In applications where frequency noise must be minimized, the Q-factor of the resonant device becomes critically important. In resonant gravimetric chemical sensing, the resonance frequency noise determines the chemical limit of detection of the resonant sensor. The following section concerns itself with viscous damping, which is generally the dominant damping mechanism for resonators operating in viscous media, and therefore primarily determines the minimum limit of the frequency noise for operation in viscous media.

3.2.2 Viscous Damping

The motion of fluids is described by the Navier-Stokes equations, which describe continuity, energy, and momentum within the fluid. The momentum equation for an incompressible fluid is given by [80]

$$\frac{\partial}{\partial t}(\rho \mathbf{v}) + \nabla \cdot (\rho \mathbf{v}\mathbf{v}) = -\nabla p + \nabla \tau + \rho \mathbf{F_{body}} \tag{11}$$

where $\mathbf{v}$ is the fluid velocity vector, p is the fluid pressure, τ is the fluid viscous stress tensor, $\mathbf{F_{body}}$ is the body force vector acting on the fluid (e.g. due to gravity), and ρ is the fluid density. The components of τ describe the normal and shear stresses exerted upon a differential volume of fluid.

The flow around an oscillating body can be considered to have two regions. The first region is a boundary layer close to the body in which the flow is turbulent and rotational. It is in this region that *viscous* energy dissipation occurs. The characteristic length scale (the penetration depth) describing this boundary layer has the following expression

$$\delta = \sqrt{\frac{2\nu}{\omega}} = \sqrt{\frac{\nu}{\pi f}} \tag{12}$$

In (12), ω is the oscillation radial frequency, f is the oscillation angular frequency, and ν is the kinematic viscosity of the fluid. Away from the boundary layer, the flow exhibits no rotational or turbulent effects, and is called potential flow. This second region of the flow is responsible for an *inertial* force acting on the body, which is called drag.

An easy way to gauge the relative dominance of inertial vs. viscous effects is to consider the Reynolds number Re. The Reynolds number describes the ratio of viscous to inertial forces present in the oscillatory flow. It is defined as

$$Re = \frac{b^2}{2\delta^2} = \frac{\rho\omega b^2}{4\mu} \tag{13}$$

where ρ is the fluid density, μ is the dynamic viscosity of fluid ($\mu = \nu\rho$), and b is the characteristic length of the flow. The Reynolds number is an elegant way of encapsulating both geometrical and frequency effects into a single parameter.

As can be seen from (13), the degree to which either viscous or inertial effects act on the oscillating body is dependent on the oscillation frequency ω. Two limits are considered: that of slow oscillation, and that of fast oscillation. For slow oscillation (i.e. low Re), the terms $\frac{\partial}{\partial t}(\rho\mathbf{v})$ and $\nabla \cdot (\rho\mathbf{v}\mathbf{v})$ disappear in (11), due to the slow time-change of the flow. It is this case that approximates potential flow. In the case of fast oscillation (i.e. large Re), the $\nabla \cdot (\rho\mathbf{v}\mathbf{v})$ term becomes small relative to the $\frac{\partial}{\partial t}(\rho\mathbf{v})$ term in (11), yielding analytical

solutions to (11) which are used in the viscous damping models of this chapter. The full mathematical details of these flow regimes can be accessed in certain classic texts on fluid mechanics [81, 82].

At fast oscillation, a thin boundary layer dominates the energy loss, and the rest of the flow outside the boundary layer is relatively undisturbed. It is in this high-frequency regime that viscous energy loss becomes dominant relative to inertial effects. Close to the oscillating surface at fast oscillation, the fluid velocity can be described as an exponentially-decaying sinusoid. The boundary conditions are dependent on the geometry of the oscillating body, but generally the fluid velocity profile will take the form of a traveling wave that decays exponentially with distance from the surface of the body. The expression for the fluid velocity in a direction parallel to the direction of oscillation takes the general form

$$\mathbf{v}\left(z,t\right)=\mathbf{v_0}e^{i\omega t-\frac{z}{\delta}} \tag{14}$$

where ω is the oscillation angular frequency and z is the direction normal to the oscillating surface, with the body surface defined as being at $z=0$. The body is assumed to be large relative to the length scale of the flow so edge effects are neglected. The overall fluid force acting on an oscillating body is generally stated as [81]

$$\mathbf{F_{fluid}}=(\beta_{viscous}+i\beta_{inertial})\mathbf{v}\left(0,t\right)=\beta_{viscous}\mathbf{v}\left(0,t\right)-\beta_{inertial}\dot{\mathbf{v}}\left(0,t\right)/\omega, \tag{15}$$

where $\beta_{viscous}$ and $\beta_{inertial}$ are factors determined by the geometry of the oscillating body. The factors $\beta_{viscous}$ and $\beta_{inertial}$ describe the contributions of viscous and inertial forces, respectively, to the overall fluid force acting on the oscillating body. In (15), the fluid forces attributable to viscous and inertial components, respectively, are out-of-phase which each other, and the inertial component decreases with oscillation frequency.

The total energy loss due to fluid forces is obtained by integrating $\mathbf{F_{fluid}}\cdot\mathbf{v}$ over the surface of the oscillating body. For a given oscillation amplitude, this viscous energy loss can then be divided by the momentum or elastic energy storage of the oscillating body to obtain the $\frac{1}{Q_{viscous}}$ value for that body. For complex structures with edge effects, this analysis is best performed using FEM or other numerical techniques.

The fluid force expression of (15) can also be coupled with the equations of motion of a resonating structure. By placing the fluid force of (15) into the force term of the Euler-Bernoulli beam equation, a coupling between the equations of motion for elastic structures and fluids can be obtained [83–85]. This allows the $Q_{viscous}^{-1}$ values of cantilever geometries to be obtained in the models presented in the following sections.

The preceding general framework has been refined in several different models to describe the viscous energy loss for microstructures oscillating in a viscous medium. In this section, three shall be discussed: the oscillating sphere model [86], the Sader cantilever model [85], and Stokes' oscillating plate model [71, 81, 87].

3.2.2.1 Oscillatory Motion of Spheres in Viscous Media

Modeling the total fluid force acting on an oscillating sphere acts as a good starting point for exploring the various models for the viscous Q-factors of resonators in viscous media.

The Stokes solution for the total fluid force exerted on an oscillating sphere is expressed as [81, 86]

$$\mathbf{F_{fluid}} = 6\pi\mu R\left(1+\frac{R}{\delta}\right)\mathbf{v} + \frac{2}{3}\pi R^3\rho_{fluid}\left(1+\frac{9}{2}\frac{\delta}{R}\right)i\omega\mathbf{v}, \tag{16}$$

where R is the radius of the sphere, μ is the dynamic viscosity of the fluid, $\mathbf{v}$ is the velocity amplitude vector of the oscillation and ρ_{fluid} is the density of the fluid. The fluid force of (16) has both real and imaginary (out-of-phase) components, corresponding to the viscous dissipation and the drag forces, respectively, described in (15).

Using the general expression for the fluid force acting on a body in (15), a general expression for the viscous Q-factor can be derived. By placing the fluid force of (15) into the force term of the Euler-Bernoulli beam equation, the general viscous Q-factor for an oscillating body can be derived as [88]

$$Q_{viscous}^{-1} = \frac{\frac{\beta_{viscous}}{m_T}}{2\pi\left(1+\frac{\frac{\beta_{inertial}}{2\pi f}}{m_T}\right)f}. \tag{17}$$

In (17), f is the angular oscillation frequency at resonance, and m_T is the total mass of

the oscillating body. Using the viscous and inertial force terms for the sphere in (16), the equation for the viscous Q-factor of an oscillating sphere becomes

$$Q_{viscous}^{-1} = \frac{3\mu R\left(1+\frac{R}{\delta}\right)}{m_T\left(1+\frac{2}{3}\frac{\pi R^3\rho_{fluid}}{m_T}\left(1+\frac{9}{2}\frac{\delta}{R}\right)\right)f}. \tag{18}$$

Two limits of (18) can be taken to find the viscous Q-factor in different flow regimes. The most relevant limit for this research is the viscous regime, where high-frequency oscillation causes the turbulent penetration depth δ to be much smaller than the structure size. It is in this regime that viscous forces dominate the energy loss to the fluid. In this situation, $\delta < R$ for the sphere model of (18), yielding the following approximation

$$Q_{viscous}^{-1} = \frac{9\sqrt{\mu\rho_{fluid}}}{4\sqrt{\pi}R\rho_{sphere}\sqrt{f}} \tag{19}$$

In (19), ρ_{sphere} is the density of the modeled sphere. The useful aspect of this approximation is that the frequency dependency of the viscous penetration depth has been taken into account in the limit, yielding only a single frequency term. From this general model, one expects that the viscous Q-factor at high frequencies should exhibit a $\frac{1}{\sqrt{f}}$ dependence, provided all other factors are held constant.

Taking the opposite limit, i.e. the case of $\delta > R$, yields the following low-frequency expression

$$Q_{viscous}^{-1} = \frac{3\mu}{4\pi\rho_{sphere}R^2 f} \tag{20}$$

In the regime described by (20), the flow around the oscillating body approximates steady-state potential flow. This low-frequency limit is generally not applicable to the oscillating microstructures of this research. However, one should note that the $\frac{1}{f}$ dependence of the viscous Q-factor shown in (20) differs from the $\frac{1}{\sqrt{f}}$ dependence shown in (19). This demonstrates that the frequency dependence of the viscous Q-factor should change with frequency itself.

For resonance frequencies ranging from 100 kHz to 1 MHz, the penetration depth δ ranges from 7 μm to 2.2 μm, respectively, in air at room temperature. Given the general

dimensions of the resonator structures presented in this research, their viscous Q-factor is better modeled by the the high-frequency, viscous regime limit (i.e. the $\frac{1}{\sqrt{f}}$ model) in room temperature air.

3.2.2.2 The Cantilever Model of Sader

The model of Sader [85] describes the viscous damping of a cantilever beam of rectangular cross-section resonating in its fundamental out-of-plane resonance mode. It adapts the solution for an oscillating beam of circular cross-section to that of a rectangular beam through a curve fit based on the Reynolds number. The result for $Q_{viscous}^{-1}$ of the fundamental out-of-plane resonance mode is

$$Q_{viscous}^{-1} = \frac{\Gamma_i(\omega)}{\frac{\pi \rho_{fluid} b^2}{4\mu} + \Gamma_r(\omega)} \tag{21}$$

where Γ_r and Γ_i are the real and imaginary parts, respectively, of the hydrodynamic function for the cantilever geometry and ω is the undamped radial resonance frequency of the fundamental out-of-plane resonance mode. b is the width of the cantilever, and ρ_{fluid} and μ are the density and dynamic viscosity of the fluid, respectively.

Γ is based on a polynomial of the logarithm of the Reynolds number and a term involving Bessel functions. The model is difficult to evaluate, but has been widely applied [88–90]. Through a polynomial approximation of the hydrodynamic function Γ, the $Q_{viscous}^{-1}$ expression of this model can also be shown to have a $\frac{1}{\sqrt{f}}$ dependence to first order [90].

3.2.2.3 The Stokes Oscillating Plate Model

Resonators with in-plane resonance modes can be modeled as plates oscillating in-plane. The plates used in this approximation are assumed to be large compared to the penetration depth δ, which allows edge effects to be neglected. In the plate model, the vorticity, pressure, and body force terms are deemed negligible in the Navier-Stokes equation for momentum of (11).

The plate model can be used to describe the case of an in-plane oscillating disk approximating the disk resonators of this research [71]. In this model, the Navier-Stokes equations

are recast using cylindrical coordinates and a disk of radius R executing small-angle rotations about its central axis is considered. The disk model uses a function Ω for the fluid angular velocity, yielding the following version of the Navier-Stokes equation for momentum with the aforementioned reductions applied [81]

$$\frac{\partial \Omega}{\partial t} = \nu \frac{\partial^2 \Omega}{\partial z^2}, \tag{22}$$

where ν is the kinematic viscosity of the fluid. The solution for Ω has the form

$$\Omega(z,t) = -\omega \theta_i e^{-\frac{z}{\delta}} sin\left(\omega t - \frac{z}{\delta}\right), \tag{23}$$

where θ_i is the amplitude of the disk angular oscillation. The relevant fluid force is the shear stress at the surface ($\sigma_{\phi z}\big|_{z=0}$). Since $\sigma_{\phi z} = \mu \frac{\partial v_\phi}{\partial z}$ and $v_\phi = r\Omega$, the viscous energy loss can be computed using

$$E_{loss} = \frac{1}{\omega} \int_0^{2\pi} \left(\int \sigma_{\phi z}(z=0) v_\phi(z=0)\, dS \right) d(\omega t), \tag{24}$$

The inner integral of (24) integrates the viscous stress multiplied by the fluid velocity over the surface S defining the disk. The outer integral computes the energy loss on the disk surface over the course of an oscillation cycle.

The energy loss expression of (24) can be inserted in the Q-factor equation of (9) to obtain the following approximation for the viscous Q-factor of a disk resonator

$$Q_{viscous}^{-1} \approx \frac{\mu R^2}{f_o \delta M}, \tag{25}$$

where f_o is the resonance frequency of the disk's in-plane mode, δ is the penetration depth, R is the radius of the disk, and M is the mass of the disk resonator [71]. To the first order, the expression simplifies to the following form

$$Q_{viscous}^{-1} \approx \frac{\rho_{fluid}}{\rho_{disk}} \frac{\delta}{t_{disk}}, \tag{26}$$

where t_{disk} and ρ_{disk} are the thickness and density of the disk, respectively, and δ and ρ_{fluid} are the penetration depth and fluid density, respectively. Using the frequency

dependence of δ, (26) becomes

$$Q_{viscous}^{-1} \approx \frac{1}{\sqrt{\pi}} \frac{\sqrt{\mu \rho_{fluid}}}{\rho_{disk} t_{disk}} \frac{1}{\sqrt{f}} \tag{27}$$

In (27), the $\frac{1}{\sqrt{f}}$ dependence is once again present in the expression for $Q_{viscous}^{-1}$.

Using the same starting point of an oscillating plate, the relation of (26) can also be derived for cantilever structures oscillating in an in-plane resonance mode [83]. Under the under assumption of high-frequency oscillation, viscous forces dominate the energy loss, and the following approximation for the viscous Q-factor of a cantilever oscillating in an in-plane mode is obtained [83]

$$Q_{viscous}^{-1} \approx \frac{1}{\sqrt{\pi}} \frac{\sqrt{\mu \rho_{fluid}}}{\rho_{cantilever} t_{cantilever}} \frac{1}{\sqrt{f}} = \frac{\rho_{fluid}}{\rho_{cantilever}} \frac{\delta}{t_{cantilever}} \tag{28}$$

In (28), $t_{cantilever}$ and $\rho_{cantilever}$ are the thickness and density, respectively, of the cantilever structure. In both (26) and (28), there is a common dependence on the ratio of fluid density to resonator density ($\frac{\rho_{fluid}}{\rho_{resonator}}$), and the ratio of penetration depth to resonator thickness ($\frac{\delta}{t_{resonator}}$). Both equations also yield a $\frac{1}{\sqrt{f}}$ frequency dependence for $Q_{viscous}^{-1}$.

(26) and (28) offer general guidance for maximizing the viscous Q-factor of a resonator with an in-plane resonance mode. The resonator thickness should be greater than the penetration depth of the oscillatory flow at resonance. Additionally, the resonator density should be great compared to the density of the surrounding fluid. Given the relatively high density of silicon in comparison to air, the later constraint is satisfied with relative ease in the gas phase. The constraint on resonator thickness, however, produces resonators with increased mass, which is generally detrimental in the mass-sensing application. Additionally, thickness increases eventually cause the plate assumption underlying the models of (26) and (28) to become invalid, in which case the models *underestimate* the viscous loss. This is because the plate model does not account for the fluid force acting on the sidewalls of structures with large thickness dimensions.

3.2.3 Anchor Loss

Anchor loss, also called support loss, is the energy loss due to transmission of elastic waves into the support structure of the resonator [73, 91–95]. For a cantilever structure of length l and thickness t resonating in an out-of-plane resonance mode, the Q^{-1}_{anchor} component of (10) can be estimated by [95]

$$Q^{-1}_{anchor} = 0.46 \left(\frac{t}{l}\right)^3 \tag{29}$$

For the same cantilever structure resonating in a fundamental in-plane resonance mode, the width of the cantilever beam b can be substituted for the thickness t to produce

$$Q^{-1}_{anchor} = 0.46 \left(\frac{b}{l}\right)^3 \tag{30}$$

These estimates can be used to approximate the anchor loss occurring in the disk resonators presented in this research, which have cantilever-like support structures.

3.2.4 Frequency Noise

The connection between resonator Q-factor and frequency noise will now be established. In the chemical sensing application, the silicon disk resonators are used as the frequency-determining element in an amplifying feedback loop. The resonance frequency of the resonator will decrease due to the added mass of the chemical analyte after analyte sorption. The loop oscillation frequency, which is determined by the resonator, is the output signal that is used to measure the concentration of the chemical analyte. The frequency noise of the loop signal thus determines the minimum concentration of analyte that can be sensed. The Q-factor of the resonator influences the amount of frequency noise in the feedback loop. The connection between the resonator Q-factor and the frequency noise will now be quantified.

The fluctuation-dissipation theorem provides the basis for the treatment of noise in equilibrium thermodynamical systems [96]. Mechanical resonators thermally interact with their environment, which introduces perturbations to the overall energy of the resonator, described by the system Hamiltonian H. The resonator system used in this analysis is

assumed to have small dissipation, i.e. a high Q-factor. By the equipartition theorem, the environment will imbue each degree of freedom of the resonator system with an average thermal noise energy equal to k_BT, where k_B is Boltzmann's constant and T is the absolute temperature. This equipartition condition holds when $\hbar\omega < k_BT$, which means the following analysis is valid for resonators operating below the terahertz regime at 300 K, including the resonators presented in this research.

The noise force generated by the thermal noise energy excites the resonator. The displacement response of the resonator for a given degree of freedom, obtained from (2), can be used to find the response of the resonator when excited by this thermal noise force. The displacement response of a single degree-of-freedom system of (2) can be rewritten in squared-magnitude form for ease of use in this analysis as [77]

$$G(\omega) = \frac{\frac{1}{M^2}}{\left(\omega_o^2 - \omega^2\right)^2 + \left(\omega_o\omega/Q\right)^2} \tag{31}$$

In (31), Q is the resonator Q-factor, M is the effective mass for the degree-of-freedom, ω_o is the resonance frequency, and ω is a free variable. The average total resonator energy induced by the noise excitation is equal to k_BT. Thus the following kinetic energy equation can be used to solve for the spectral density of the thermal noise force $S_f(\omega)$ [77, 96]

$$k_BT = M\int_0^\infty \omega^2 S_f(\omega)G(\omega)\ d(\omega) \tag{32}$$

Given that $G(\omega)$ is known, the energy equation (32) can be used to solve for the spectral density of the thermal noise force $S_f(\omega)$, giving the following general form [97]

$$S_f(\omega) = 2k_BT\frac{\omega_o M}{\pi Q} \tag{33}$$

In (33), $S_f(\omega)$ has units of $N^2/(\text{rad/s})$. The above spectral density function has the general form of a white Gaussian noise. That is, the noise density of (33) is constant with radial frequency ω. The spectral density of the thermal noise in (33) describes the thermal force being exerted on the resonator. The resonator amplitude noise caused by this thermal force is described by the product [97]

$$S_x(\omega) = G(\omega)S_f(\omega) \tag{34}$$

$S_x(\omega)$ in (34) is the spectral density of the amplitude noise, describing the noise in the resonator displacement amplitude as a function of frequency, and has units of $m^2/(\text{rad/s})$. To relate this amplitude noise to frequency noise, i.e. the deviation in the resonator's resonance frequency, the spectral density of phase noise $S_\phi(\omega)$ is first introduced. This phase noise density $S_\phi(\omega)$ describes the noise of the resonator phase response as a function of frequency [98]. The general equivalence of phase noise and amplitude noise can be summarized by [97]

$$S_\phi(\omega) \propto \left(\omega_o^2\right) S_x(\omega) \tag{35}$$

The exact details of the above relation rely on an excitation-force-dependent term, and are given in reference [97].

The form of the phase noise $S_\phi(\omega)$ is obtained by assuming $\omega_o/Q << \omega << \omega_o$. This assumption corresponds to phase noise originating from frequencies away from the resonance peak of the system. Under this assumption, and through the relations of (33), (34), and (35), the spectral density of phase noise $S_\phi(\omega)$ has the form [97]

$$S_\phi(\omega) \approx \frac{k_B T \omega_o}{8\pi E_c Q \omega^2} = \frac{k_B T}{8\pi P_c Q^2} \left(\frac{\omega_o}{\omega}\right)^2 \tag{36}$$

In (36), E_c is the maximum kinetic energy of the resonator system at the resonance frequency ω_o, and P_c is the corresponding power defined by $P_c = \omega_o E_c/Q$. It should be noted that the phase noise $S_\phi(\omega)$ of (36) has a dependence on the strength of the resonator excitation through the P_c term [97]. The full derivation of (36) is given in [97].

The relationship between phase noise and frequency noise is established in the following steps. A time-domain measurement of the resonator displacement amplitude has the general form

$$a(t) = a_o sin(\omega_o t + \phi(t) + \theta) \tag{37}$$

In (37), $\phi(t)$ is a noise-induced time-varying phase with spectral density $S_\phi(\omega)$. Noise in the resonator oscillation frequency can be related to phase noise by defining the time-varying oscillation frequency as [97]

$$\omega(t) = \omega_o + \frac{d\phi}{dt} \tag{38}$$

From (38), we define a quantity $\delta\omega$ which quantifies the deviation from the resonance frequency ω_o [97]

$$\delta\omega = \omega(t) - \omega_o = \frac{d\phi}{dt} \tag{39}$$

To analyze $\delta\omega$ in the frequency domain, $\phi(t)$ of (39) can be assumed to be sinusoidal. Additionally, the fractional frequency noise $y = \frac{\delta\omega}{\omega_o}$ is defined, which is more meaningful than $\delta\omega$ by itself. The time-domain relationship of (39) is now used to find the frequency domain relationship between the fractional frequency noise and the phase noise [97–99]

$$S_y(\omega) = \left(\frac{\omega}{\omega_o}\right)^2 S_\phi(\omega) \tag{40}$$

In (40), $S_y(\omega)$ is the spectral density of the fractional frequency noise (frequency noise), describing the deviation in the resonance frequency as a function of radial frequency ω. Using (36) and (40), the spectral density of frequency noise (also called white frequency modulation) can finally be expressed as [97]

$$S_y(\omega) = \frac{k_B T}{8\pi P_c Q^2} \tag{41}$$

In (41), the important relationship between resonator oscillation power P_c and frequency noise density $S_y(\omega)$ is established. With a greater oscillation power, the frequency noise in the oscillator system is reduced. In keeping with the previously stated assumptions of this analysis, the density of (41) describes the frequency noise in the off-resonance region of the frequency spectrum.

This frequency noise $S_y(\omega)$ is measured in the time domain using the Allan variance $\sigma_f(\tau)$, which statistically quantifies the frequency noise when frequency is measured as a

function of time [98–100]

$$\sigma_f^2(\tau) = \langle \frac{1}{2}(\bar{f_{k+1}} - \bar{f}_k)^2 \rangle \tag{42}$$

In (42), τ is the sampling time and $\bar{f}_k$ is an average measurement of the resonator oscillation frequency during the time interval k of length τ occurring from time index k to time index $k+1$. In the resonant gravimetric chemical sensing application, the Allan variance is applied to the baseline oscillator loop signal to determine the frequency noise floor. The Allan variance is dimensionless, allowing comparison of frequency noise between systems with differing resonance frequencies.

The frequency noise density up to this point has been described in the frequency domain. The frequency noise density is transformed into the time domain through the Allan variance. A transformation between the frequency domain description of the frequency noise density and the time-domain Allan variance must therefore be defined. This transformation, stated in terms of the phase noise density, is [99]

$$\sigma_f^2(\tau) = 2\left(\frac{2}{\omega_o \tau}\right)^2 \int_0^\infty S_\phi(\omega) sin^4\left(\frac{\omega\tau}{2}\right) d\omega \tag{43}$$

Through the relation of (40), the transformation of (43) is completely equivalent to a transformation of the frequency noise density $S_y(\omega)$. Through the transformation of (43), the final form of the frequency noise in the time domain is given, yielding a $\frac{1}{Q}$ dependence [70, 77–79]

$$\sigma_f(\tau) = \frac{1}{Q}\sqrt{\frac{k_B T}{8 P_c \tau}} \tag{44}$$

Allan variance thus becomes the immediately useful measure of frequency noise. In (44), the connection between Q-factor and Allan variance is established. This thenceforth allows the analysis of Q-factor with the expected result that improvements in Q-factor yield improvements in frequency noise as measured by the Allan variance.

The particular noise process presented corresponds to white frequency modulation. The Allan variance expression of (44) is valid for τ on the order of seconds, and holds for the

measurements performed in this research. Different frequency noise dependencies arise when the τ value is changed [98], corresponding to the different noise processes studied in the extensive literature relating to frequency control [99].

3.3 Measurement of the Resonator Q-factor

The dynamic energy loss mechanisms present in the disk resonator can be analyzed by taking measurements of the resonator Q-factor. To measure the amount of viscous loss, it is necessary to know the Q-factor of the disk resonator at both atmosphere and high vacuum. The amount of viscous loss can then be obtained using the expression

$$Q_{viscous}^{-1} = Q_{atmosphere}^{-1} - Q_{vacuum}^{-1} \tag{45}$$

In (45) , $Q_{atmosphere}^{-1}$ and Q_{vacuum}^{-1} are the inverses of the Q-factors measured at atmosphere and vacuum, respectively. (45) holds due to the negligible effect of viscous damping at high vacuum.

Several assumptions are made about the loss mechanisms for the resonators studied in this research. The resonators in this research have resonance frequencies less than 1.3 MHz and are fabricated from single crystal silicon. The $Q_{internal}^{-1}$ value for the internal friction mechanisms are several orders of magnitude below those of other mechanisms (e.g. viscous damping) in this frequency regime [91], hence the role of internal friction (e.g. thermo-elastic damping) is not taken to be a dominant effect in the obtained results . It is thus assumed that the dominating loss mechanism at vacuum is anchor loss alone (i.e. $Q_{vacuum}^{-1} \approx Q_{anchor}^{-1}$). The disk resonators used in the measurements are actuated in their rotational in-plane resonance mode, which has a resonance frequency that varies between 270 kHz and 1.3 MHz, depending on the radius of the disk. The disk radii of the disk resonators used in this research vary between 100 μm and 200 μm.

Piezoresistive transfer characteristics of the disk resonators are used to determine the Q-factors at atmosphere and vacuum. The piezoresistive transfer characteristics of the disk resonators are obtained using a network analyzer (Agilent 4394A). For the vacuum measurements, the resonators are placed in a vacuum chamber, which is pumped down to

≈ 2 μbar.

For comparison purposes, the viscous loss of the disk resonators is measured alongside that of silicon micromachined clamped-free cantilever structures (see Figure 10). The fabrication process for the cantilever structures is identical to that of the disk resonators, which is described in Chapter 2.

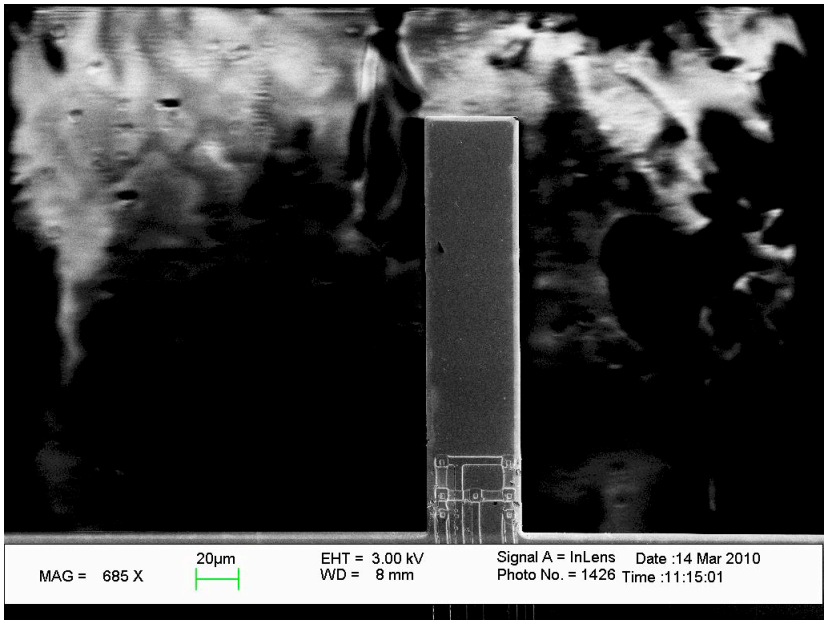

Figure 10: SEM micrograph of a cantilever used in this research. The width is 45 μm and the length is 200 μm.

The clamped-free cantilevers are actuated in both fundamental out-of-plane and fundamental in-plane resonance modes. Resonance frequencies of the fundamental in-plane resonance mode vary between 60 kHz and 1.2 MHz. A FEM simulation of the fundamental in-plane resonance mode of a clamped-free cantilever is pictured in Figure 11. Resonance frequencies of the fundamental out-of-plane resonance mode vary between 18 kHz and 680 kHz. A FEM simulation of the fundamental out-of-plane resonance mode of a clamped-free cantilever is pictured in Figure 12. For both Figure 11 and Figure 12, the simulated structure is composed of single crystal silicon with dimensions of $l = 600\mu$m, $b = 60\mu$m, and $t_{Si} = 20\mu$m. Table 5 lists the geometric parameters of the cantilevers used in this research.

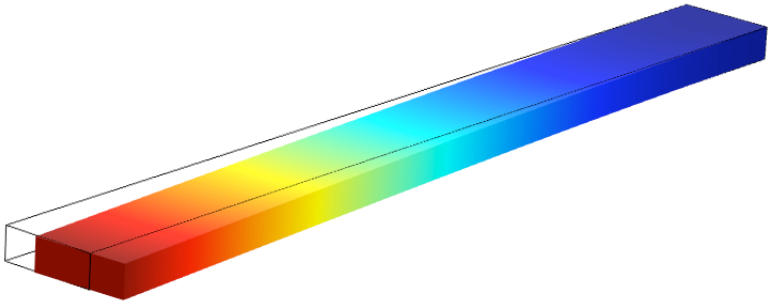

Figure 11: FEM simulation of the deflection of the fundamental in-plane resonance mode of a resonant clamped-free cantilever. The simulated structure is single crystal silicon with $l = 600\mu$m, $b = 60\mu$m, and $t_{Si} = 20\mu$m.

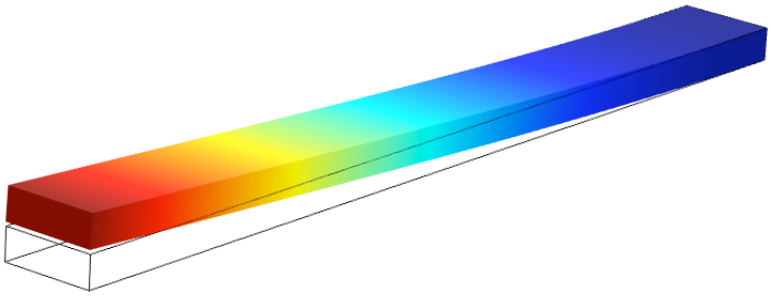

Figure 12: FEM simulation of the deflection of the fundamental out-of-plane resonance mode of a resonant clamped-free cantilever. The simulated structure is single crystal silicon with $l = 600\mu$m, $b = 60\mu$m, and $t_{Si} = 20\mu$m.

Table 5: Physical Parameters for Cantilever Devices.

Parameter	Description	Value(s)
t_{Si}	Cantilever silicon thickness	7 and 20 μm
b	Width of cantilever beam	45,60,90 μm
l	Length of cantilever beam	200-1000 μm
f_{ip}	Resonance frequencies of fundamental in-plane mode	60 kHz - 1.2 MHz
f_{oop}	Resonance frequencies of fundamental out-of-plane mode	18 - 680 kHz

Although the cantilevers are designed specifically for actuation and sensing of the in-plane mode [101], low amplitude out-of-plane modes are visible in the output spectrum, allowing extraction of their Q-factor. The presented Q-factor results (also tabulated in the Appendices) are obtained from disk resonators of various silicon thicknesses and disk radii, and cantilevers of different silicon thicknesses, widths, lengths, and resonance modes.

3.4 Energy Loss and Deflection at Resonance for the Disk Resonator

To analyze the energy loss of the disk resonator due to the mechanisms of viscous damping and anchor loss, transfer characteristics of the disk resonator at atmosphere and vacuum must be obtained (see (45)). Figure 13 shows the piezoresistive transfer characteristic of a single disk resonator around the resonance frequency of its rotational in-plane resonance mode at atmosphere and 2 μbar. The disk resonator has a silicon thickness of 18 μm and a disk radius of 170 μm.

The Q-factor is expected to increase in vacuum, relative to its value at atmospheric pressure, due to the absence of viscous damping from the air. The removal of viscous damping also causes an increase in the resonance frequency of the rotational in-plane resonance mode. Measurements such as the one in Figure 13 are used to draw conclusions about the energy loss dependencies in the disk resonator. A compiled table of all the disk measurement data is presented in Appendix 1. The measurement data associated with the cantilever devices is presented in Appendix 2.

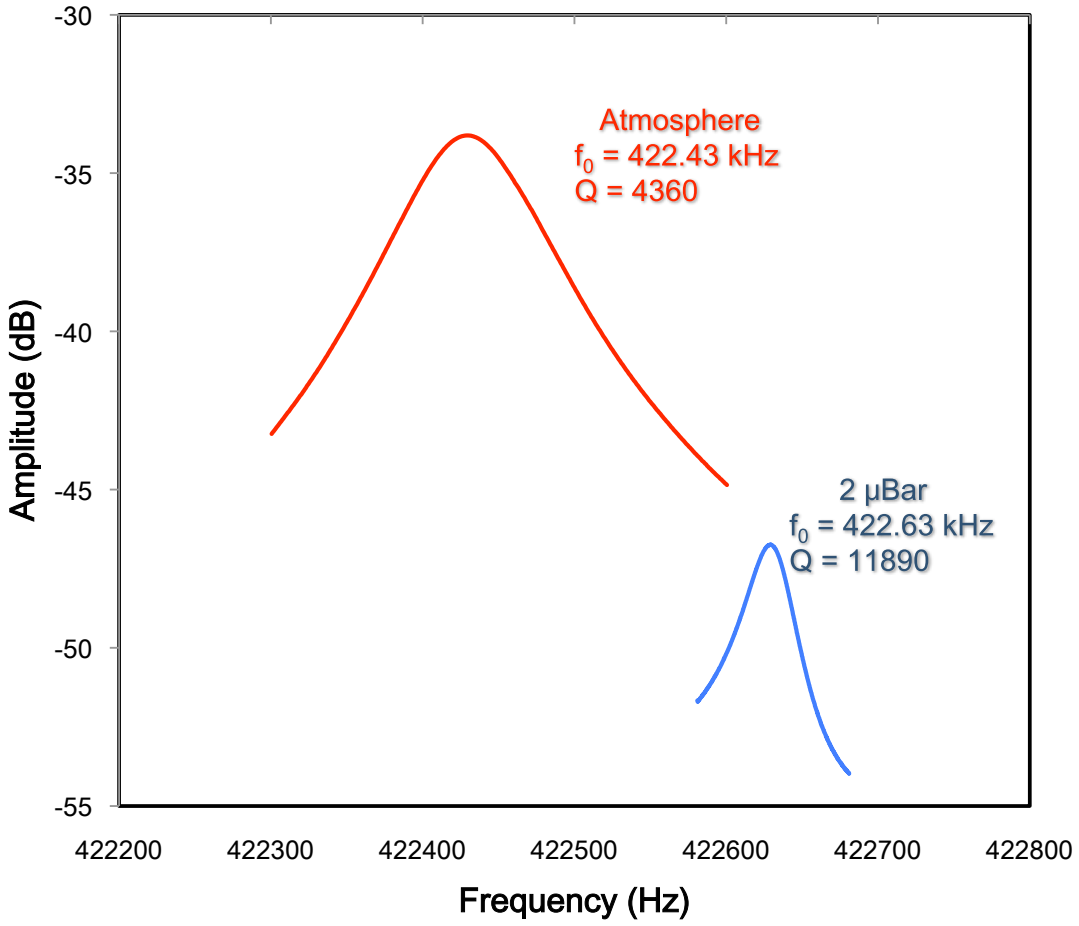

Figure 13: Piezoresistive transfer functions around the resonance frequency of the rotational in-plane resonance mode for a disk resonator with $t_{Si} = 18\mu$m and $r_o = 170\mu$m at atmosphere and 2 μbar.

3.4.1 Q-factor from Viscous Damping

The viscous damping of the disk resonator is first compared with that of micromachined clamped-free cantilever beams. Using these comparisons and the models presented earlier, several conclusions can be made about the frequency and silicon thickness dependencies of viscous damping for the disk resonators.

Figure 14 shows the extracted $Q_{viscous}^{-1}$ values obtained for disk resonators oscillating in their rotational in-plane resonance mode and the extracted $Q_{viscous}^{-1}$ values obtained for microcantilevers oscillating in their fundamental out-of-plane and fundamental in-plane resonance modes as a function of the respective resonance frequencies. The silicon thickness

for the cantilevers is either 7 μm or 20 μm. The silicon thickness for the disk resonators is either 7 μm or 18 μm.

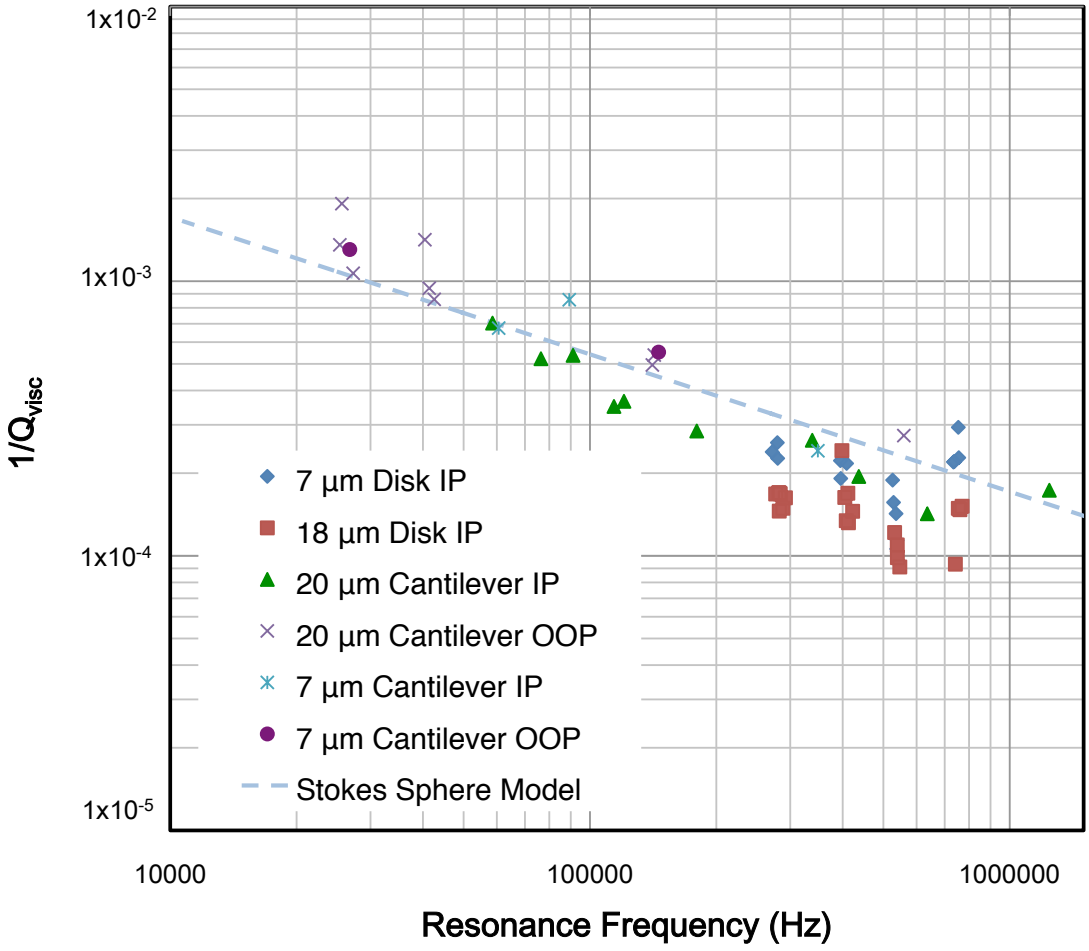

Figure 14: $Q_{viscous}^{-1}$ values for the cantilever and disk resonators as a function of resonance frequency measured at atmosphere. Both in-plane and out-of-plane resonance modes are shown (designated IP and OOP, respectively).

The blue dashed line of Figure 14 shows the $Q_{viscous}^{-1}$ values obtained from the Stokes oscillating sphere theory of (19). The parameters used in the model are listed in Table 6. For the Stokes sphere theory, only the frequency is changed, and a constant notional sphere radius of 15 μm is used across all frequencies. The chosen sphere radius of 15 μm yields a best fit for the data, and represents a length scale on the same order of magnitude as the smallest feature sizes of the disk resonators and microcantilevers (e.g. the silicon thickness t_{Si}). The Stokes sphere model, like all the viscous damping models presented in

Table 6: Parameters used in Modeling of Viscous Damping.

Parameter	Description	Value(s)
E_{Si}	Young's modulus of silicon (isotropic)	130 GPa
ρ_{Si}	Density of silicon	2330 kg/m^3
t_{Si}	Modeled Resonator silicon thickness (plate model)	7 μm, 20 μm
b	Modeled width of cantilever beam (Sader model)	60 μm
R	Notional sphere radius (Stokes sphere model)	15 μm
μ	Dynamic viscosity of air	1.8x10^{-5} $Pa \cdot s$
ρ_{air}	Density of air	1.1839 kg/m^3

this chapter, gives a $\frac{1}{\sqrt{f}}$ dependence for the $Q^{-1}_{viscous}$ values.

In accordance with the $\frac{1}{\sqrt{f}}$ dependence, the higher frequency resonators have consistently less viscous damping. The disk resonators are seen to have a spread in their data. There is an up to 2x variance in the viscous damping for disk resonators of a given silicon thickness and lateral geometry, especially at higher frequencies. This could be attributed to local variations in the resonator silicon thickness. Alternatively, the presence of spurious out-of-plane displacements for the in-plane rotational resonance mode of the disk resonator could cause the variance in the $Q^{-1}_{viscous}$ values. This latter effect would cause increased viscous damping due to added normal stresses from the fluid on the disk resonator surface.

The theory of Sader [85] can alternatively be applied to the cantilevers resonating in their fundamental out-of-plane resonance mode to demonstrate a general $\frac{1}{\sqrt{f}}$ dependence of the viscous damping. The model provides the cantilever Q-factor from viscous damping as a function of the Reynolds number Re, assuming an out-of-plane resonance mode. The characteristic length of Re in Sader's theory is the cantilever width b. Applying the Sader model of (21) to all the data for the cantilevers resonating in out-of-plane resonance modes, it becomes apparent that the Sader model fits the data for out-of-plane resonance modes well (see Figure 15). The only geometrical parameter used in the Sader model is the cantilever width b, which was chosen to be 60 μm for the displayed curve in Figure 15. All of the physical parameters for the model are as in Table 6.

Figure 16 shows $Q^{-1}_{viscous}$ data for both disk resonators and cantilever structures oscillating in an in-plane resonance mode. The viscous Q-factor values are obtained for disk

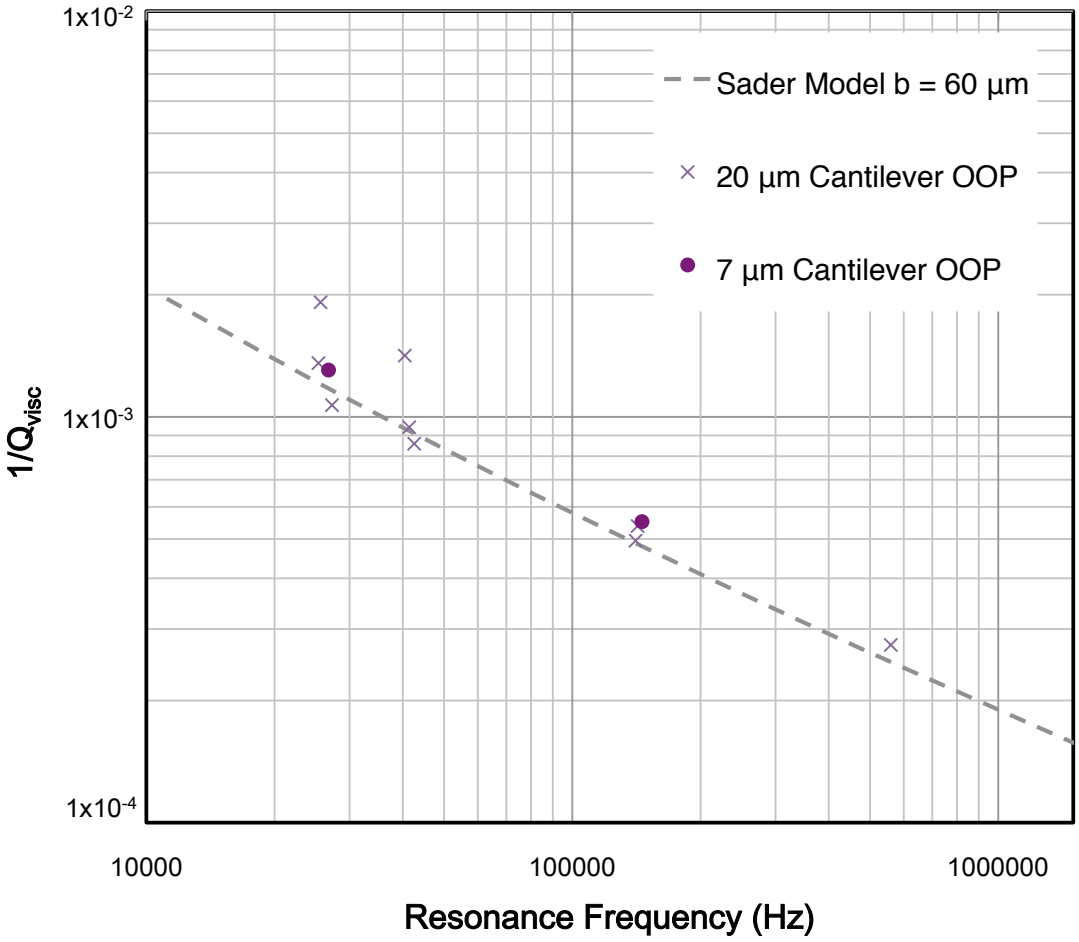

Figure 15: $Q_{viscous}^{-1}$ values for cantilever structures oscillating in an out-of-plane resonance mode as a function of resonance frequency measured at atmosphere. Sader model for a cantilever width of 60 μm is shown as the dashed line.

resonators oscillating in their rotational in-plane resonance mode and cantilevers oscillating in their fundamental in-plane resonance mode. The lines correspond to the plate model of (28), which is equivalent to (26), for silicon thicknesses of 7 μm and 20 μm. As with the other models, the model of (28) has a $\frac{1}{\sqrt{f}}$ dependence.

As can be seen in Figure 16, disk resonators using in-plane resonance modes have a specific advantage in that their thickness can be increased to reduce the viscous damping. An increase in thickness yields an increase in both the effective mass and effective stiffness of the in-plane resonance mode, which keeps the resonance frequencies of in-plane resonance

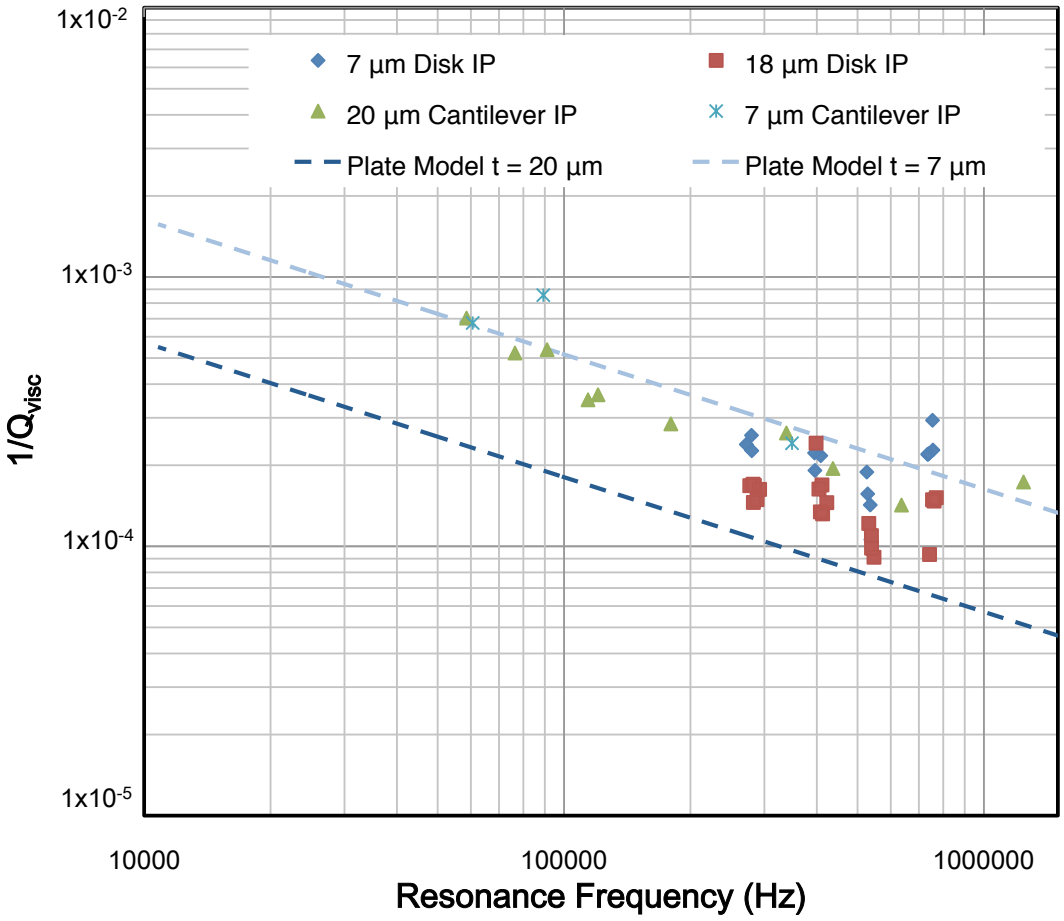

Figure 16: $Q^{-1}_{viscous}$ values for the cantilever and disk resonators as a function of resonance frequency measured at atmosphere. Only resonators with in-plane resonance modes are shown. The model of (28) is shown for different silicon thicknesses.

modes constant to first order with device thickness. The increased thickness leads to an increase in overall Q-factor. For a given silicon thickness, the disk resonators achieve a lower viscous damping than cantilevers of the same silicon thickness oscillating at a comparable resonance frequency in their fundamental in-plane resonance mode. Additionally, the disk resonators appear to more closely follow the plate model of (28) and (26) than the cantilever structures. The lack of agreement for the cantilever structures with a 20 μm silicon thickness can be attributed to the relatively small lateral dimensions of these devices compared to their silicon thickness. This can be quantified by the $\frac{t_{cantilever}}{b}$ ratio of these structures. For these structures, $\frac{t_{cantilever}}{b}$ is relatively large, leading to a disagreement with the model's

underlying assumption of an oscillating plate. It appears that to model the $Q^{-1}_{viscous}$ for the cantilevers appropriately, edge effects and the influence of the sidewalls must be considered, whereas the disk resonators more closely resemble the ideal oscillating plate.

Figure 17 shows the $Q^{-1}_{viscous}$ values for the cantilevers oscillating in their fundamental in-plane resonance mode, with the data for different cantilever widths b being separated by different symbols. The model of (28) is once again shown for silicon thicknesses of 7 μm and 20 μm.

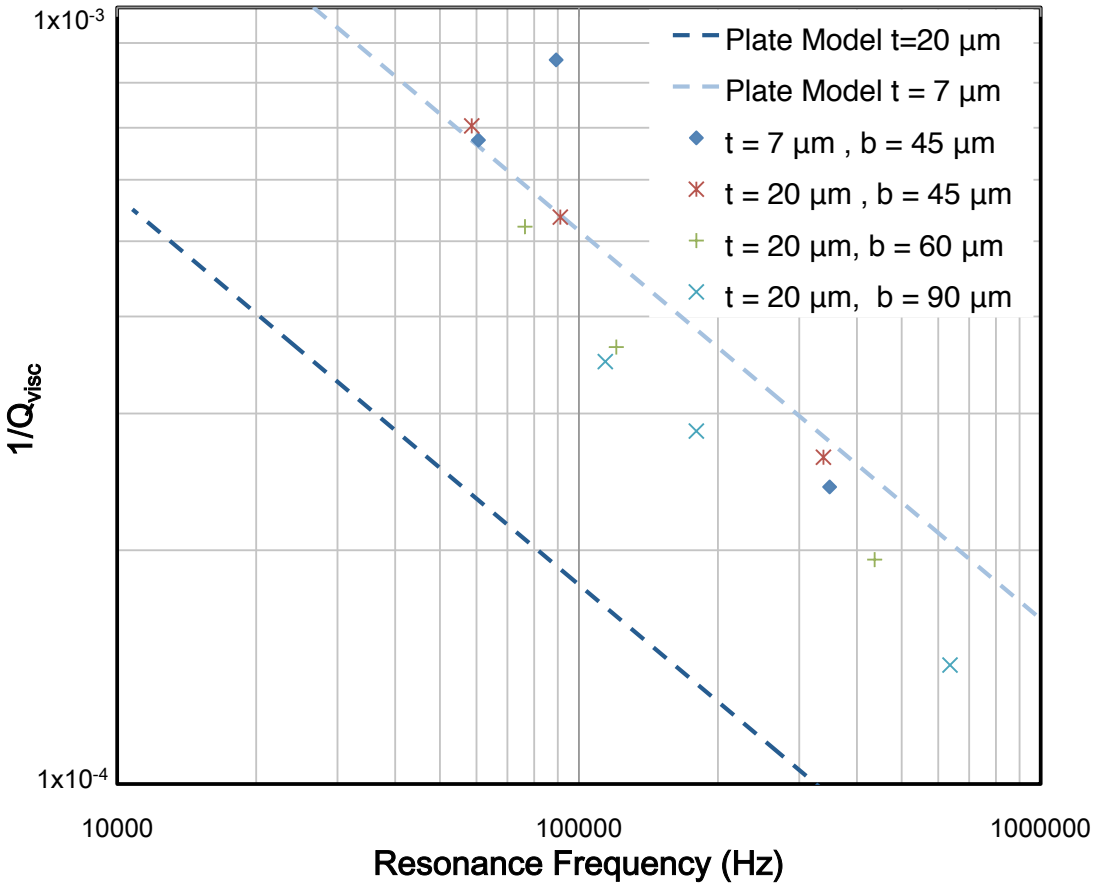

Figure 17: $Q^{-1}_{viscous}$ values for cantilevers of different silicon thicknesses and widths oscillating in their fundamental in-plane resonance mode. The model of (28) is shown for different silicon thicknesses.

A closer agreement with the plate model of (28) can be seen for cantilevers with greater b, and thus lower $\frac{t_{cantilever}}{b}$. The 7 μm silicon thickness cantilevers have a width of 45 μm, giving $\frac{t_{cantilever}}{b} = 0.15$. The 20 μm silicon thickness cantilevers have $\frac{t_{cantilever}}{b} = 0.44$ to

0.22, corresponding to widths ranging from 45 μm to 90 μm, respectively. In the case of the cantilevers with a 20 μm silicon thickness and 45 μm width, the viscous losses are much greater than the model of (28) predicts for a 20 μm silicon thickness. The cantilevers with a 20 μm silicon thickness and greater widths are closer to approximating an oscillating plate, and show a monotonic convergence to the model of (28) for the 20 μm silicon thickness. However, the edge effects and the sidewalls must still be considered to properly model the $Q_{viscous}^{-1}$ of these devices.

In summary, the data of Figure 14 demonstrate that disk devices have lower viscous damping than cantilever devices at a given resonance frequency. The theoretical explanation for this difference is the better approximation of an in-plane oscillating plate achieved by the disk devices. This greater geometrical similarity with the ideal in-plane oscillating plate allows disk devices to achieve the lower viscous damping associated with in-plane resonance modes.

3.4.2 Q-factor Dependence on Geometric Parameters

The rotational in-plane resonance mode of the disk resonator allows for increases of the silicon thickness without affecting the resonance frequency of the rotational in-plane resonance mode, to first order. This is due to the simultaneous increase in both the effective stiffness and effective mass of the resonance mode with increases in the resonator's silicon thickness. Due to these increases in effective mass and effective stiffness, the Q-factor of the disk resonator can also be expected to increase with increasing thickness. Figure 18 shows $\frac{1}{Q}$ for the rotational in-plane resonance mode of the disk resonator at atmosphere as a function of the resonator silicon thickness t_{si}. The measurements are taken from the full range of lateral geometries for each silicon thickness, with disk radii varying from 100 μm to 200 μm, and clearly show the overall trend of increasing Q with increasing t_{si}. Due to these measurements being taken at atmospheric pressure, all energy loss mechanisms are included in these measurements.

Figure 19 shows $\frac{1}{Q}$ of the rotational in-plane resonance mode measured at atmosphere as a function of disk radius for resonators of 7 μm, 18 μm, and 25 μm silicon thicknesses.

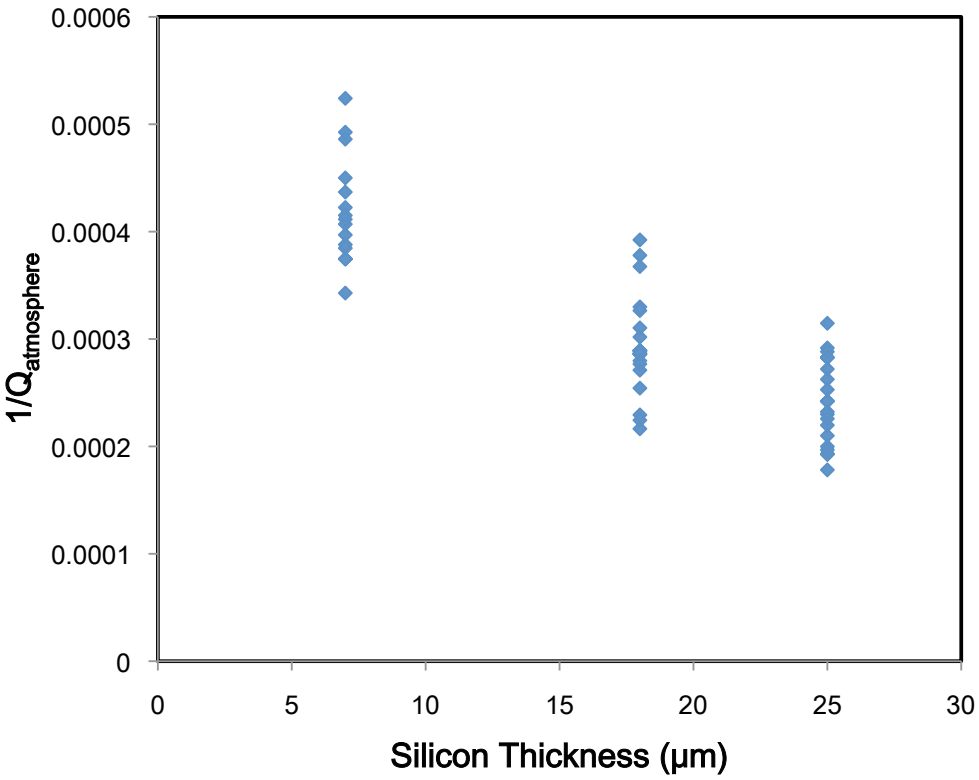

Figure 18: $\frac{1}{Q}$ of the rotational in-plane resonance mode of the disk resonators at atmosphere as a function of resonator silicon thickness. Data points represent all tested lateral geometries.

The disk radii vary between 100 μm and 200 μm. The disk radius that maximizes Q is around 170 μm for the resonators with 7 μm and 18 μm silicon thicknesses. The apparent optimal lateral geometry for maximizing the Q-factor of the rotational in-plane resonance mode is a result of the combined contributions of viscous loss and anchor loss, which are discussed and quantified in the remainder of this section.

Figure 20 shows the contribution of viscous damping to the rotational in-plane mode Q-factor as a function of disk radius. An oscillating disk model [71] for the viscous damping is also shown in the plot to show the predicted viscous damping as a function of disk radius. The model used in Figure 20 is a detailed analytical model specific to the disk resonators [71], and is obtained by evaluating (24) over the resonator's lateral geometry. The oscillating plate models of (26) and (28) are approximations of the model used in Figure 20. The general trend is that of an increasing contribution of viscous damping with disk

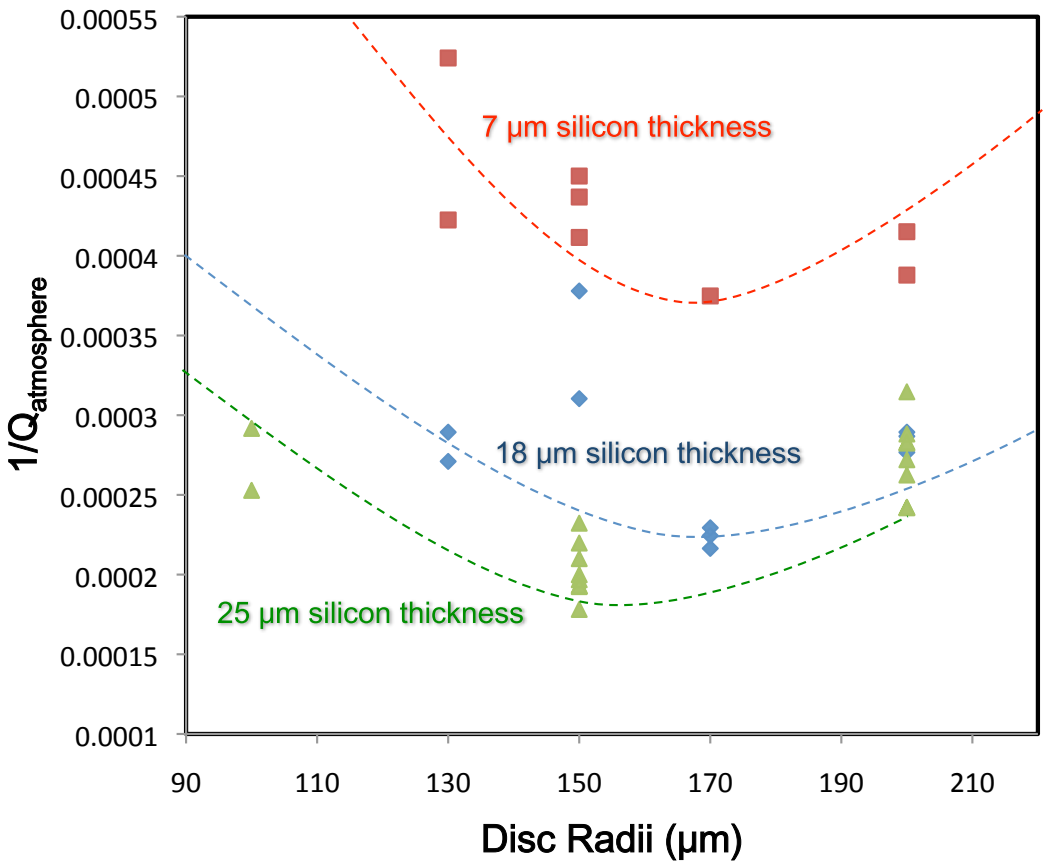

Figure 19: $\frac{1}{Q}$ for the rotational in-plane resonance mode of disk resonators at atmosphere as a function of disk resonator radius for devices with 25 μm, 18 μm and 7 μm thicknesses. Measurements shown are taken at atmospheric pressure. Dashed lines are shown as a guide to the eye.

radius, which is consistent with the frequency dependence of viscous damping in the models of the previous section, as a larger disk radius translates into a lower resonance frequency of the rotational in-plane resonance mode.

From Figure 20, it appears that the viscous loss contribution is minimized for a disk radius of 150 μm. For radii of 130 μm and 200 μm, the contribution of viscous loss is roughly the same. This condition holds for both silicon thicknesses, and indicates that the contribution of viscous damping for smaller radius/higher frequency devices is greater than expected by the model of [71]. This is not consistent with the model, and may be attributed to spurious out-of-plane deflections of the rotational in-plane resonance mode for

these smaller radius/higher frequency devices.

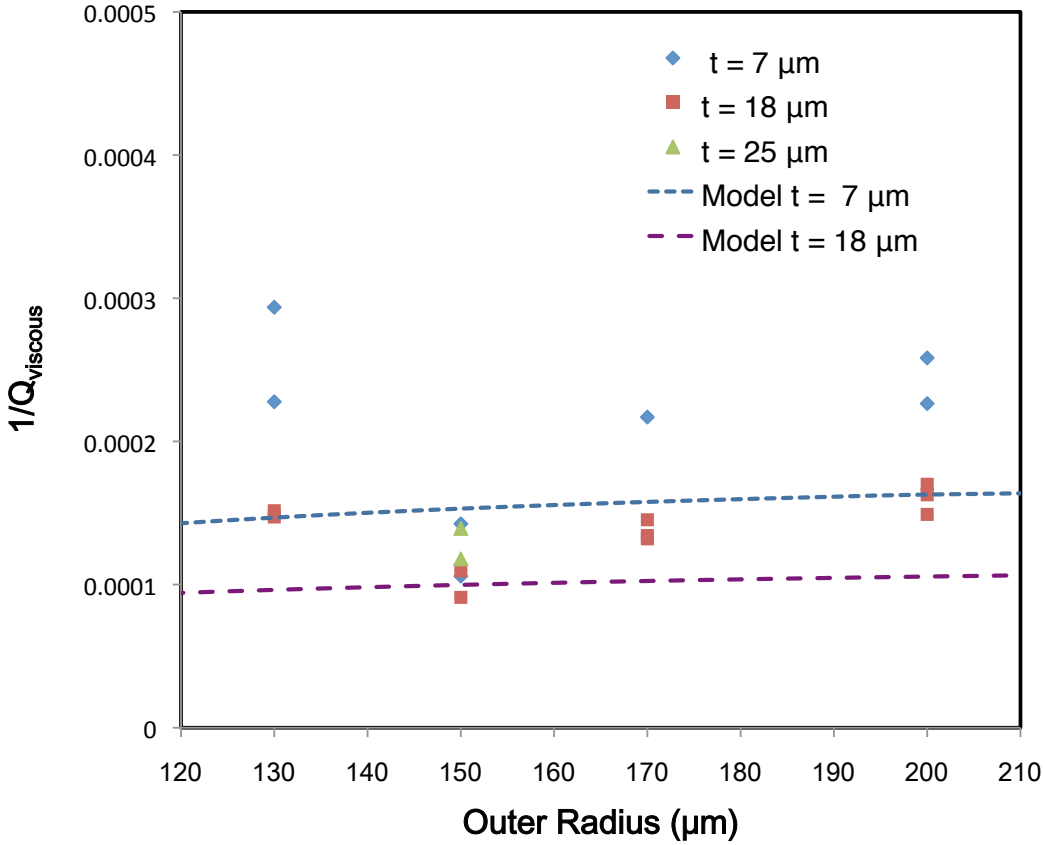

Figure 20: $Q_{viscous}^{-1}$ for the rotational in-plane resonance mode of the disk resonator as a function of disk radius. Data shown are for silicon thicknesses of 7 μm, 18 μm and 25 μm.

Figure 21 shows the viscous damping of the rotational in-plane resonance mode of disk resonators with 7 μm and 18 μm silicon thicknesses as a function of $\frac{t_{Si}}{\delta}$, where δ is the penetration depth of (12). According to (26), $Q_{viscous}^{-1}$ should be inversely proportional to $\frac{t_{Si}}{\delta}$. The model of (26) is shown in Figure 21. In accordance with the model of (26), the viscous loss $Q_{viscous}^{-1}$ generally decreases with increasing $\frac{t_{Si}}{\delta}$. The variance in the data is attributed to edge effects in the fluid flow and possible out-of-plane displacements.

Finally, Figure 22 shows the anchor loss of the rotational in-plane resonance mode of the disk resonator as a function of disk radius. Results for resonators with 7 μm and 18 μm silicon thicknesses are shown. The anchor loss is shown to not be dependent on the silicon thickness of the resonator, with anchor loss values for both silicon thicknesses roughly

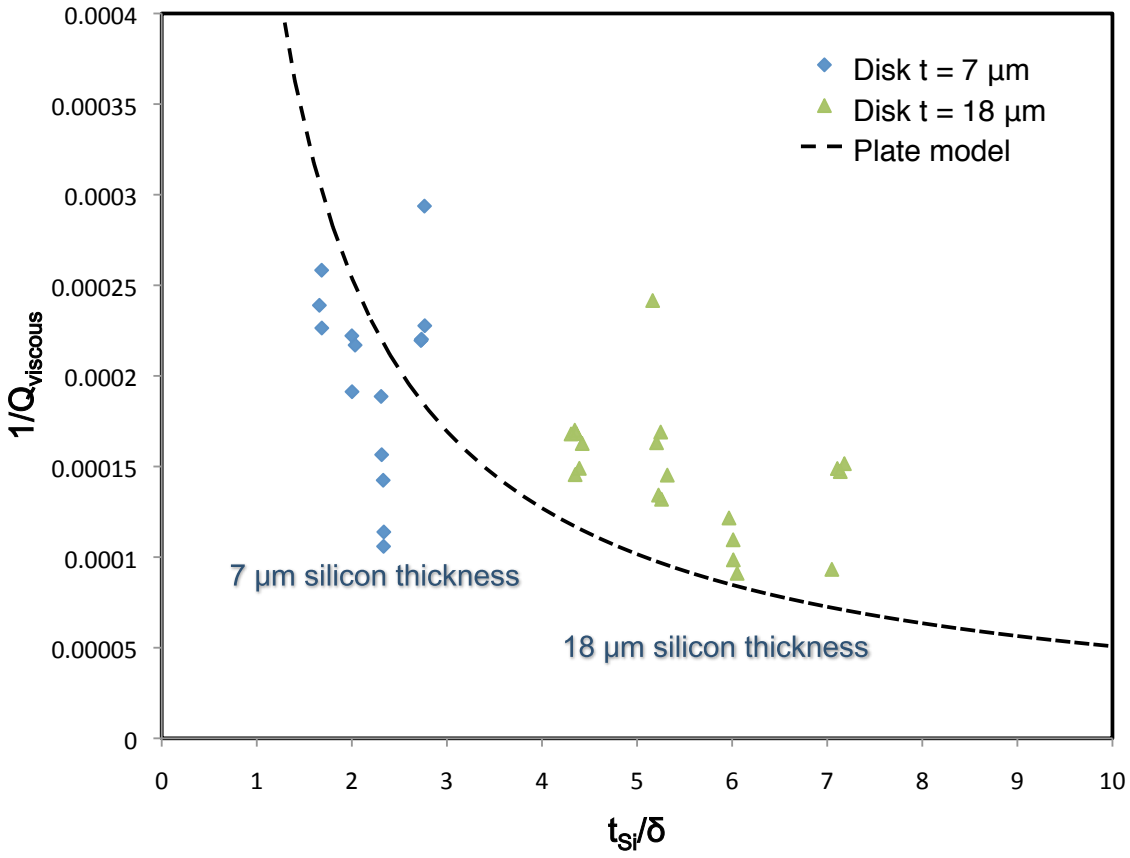

Figure 21: $Q_{viscous}^{-1}$ as a function of $\frac{t_{Si}}{\delta}$ for the rotational in-plane resonance mode of disk resonators with 7 μm and 18 μm silicon thicknesses. The line is the oscillating plate model of (26).

overlapping. This is consistent with the theory of (30). The variance in the anchor loss values can be 50% for a given disk radius. Lateral geometrical defects resulting from the resonator fabrication process may be the source of this variance.

The dashed line in the plot comes from the in-plane anchor loss model of (30). The effective width w for the model is the 45 μm width of the disk resonator clamped-clamped support beam, and the effective length l is chosen to be the length of the disk resonator clamped-clamped support beam (i.e. 500 μm). For the given width w, the measured anchor loss values are small enough as to only be accounted for by an effective anchor length on the order of hundreds of microns. The only features of that size on the resonator structure are

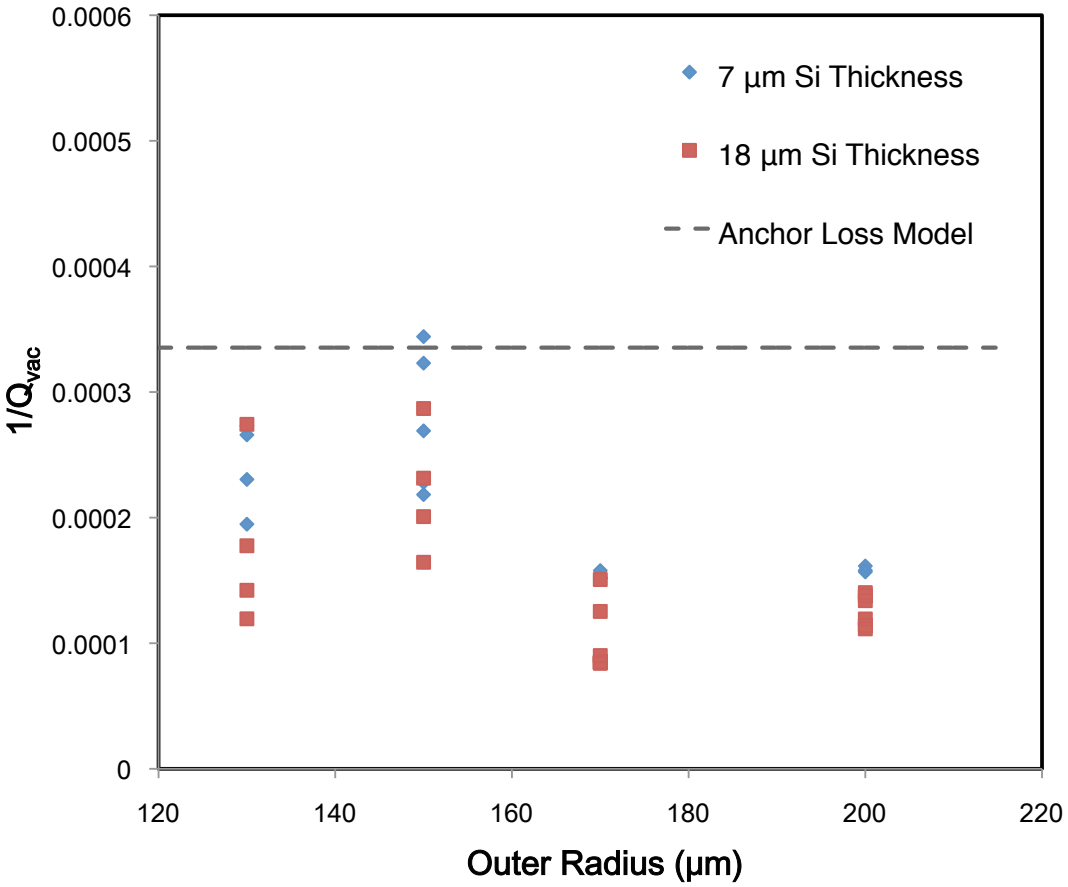

Figure 22: Q_{anchor}^{-1} of the rotational in-plane resonance mode of the disk resonators as a function of disk radius. The dashed line is the anchor loss model of (30). The measured values of anchor loss correspond to an effective length l on the order of the length of the clamped-clamped support beam.

the disk radii and clamped-clamped support beam. It is thus concluded that the clamped-clamped supprt beam, being larger than the disk radius, is the main determinant of the total anchor loss.

Given the anchor loss values in Figure 22, the Q-factor limit due to anchor loss of the rotational in-plane resonance mode can be estimated. Given that the minimum values of Q_{anchor}^{-1} are in the 1×10^{-4} range, the maximum Q-factor limit due to anchor loss is estimated to be on the order of 10000. Since the anchor loss is invariant with the resonator silicon thickness, this gives an upper limit to the Q-factor that can be achieved by increasing the resonator silicon thickness to minimize viscous damping.

3.4.3 Deflection at Rotational In-plane Resonance

The deflection of the disk resonator at the resonance frequency of its rotational in-plane mode has both in-plane and out-of-plane components. Out-of-plane components can be analyzed using a laser vibrometer, which can measure the out-of-plane deflection at a specific point on the surface of the device using the Doppler shift of a reflected laser beam. The in-plane deflection of the rotational in-plane resonance mode can be measured by capturing a series of images of the resonator when a strobe light illuminates the device at a frequency close to the resonance frequency of the rotational in-plane resonance mode. Subsequent image processing of the captured images can allow the in-plane deflection of the device to be obtained. The following sections present analyses of both the out-of-plane and in-plane deflections of the disk resonator at its rotational in-plane resonance mode. The measurements were made using a Polytec MSA-500 system, which has both laser vibrometry and stroboscopic capabilities.

For the vibrometric and stroboscopic measurements, no readout circuitry was connected to the output ports of the resonator's Wheatstone bridge. The Wheatstone bridge was shorted by connecting ground to both power inputs, and the same excitation signal was connected to both excitation resistors. This modified excitation scheme is compared with the closed-loop excitation scheme in Figure 23.

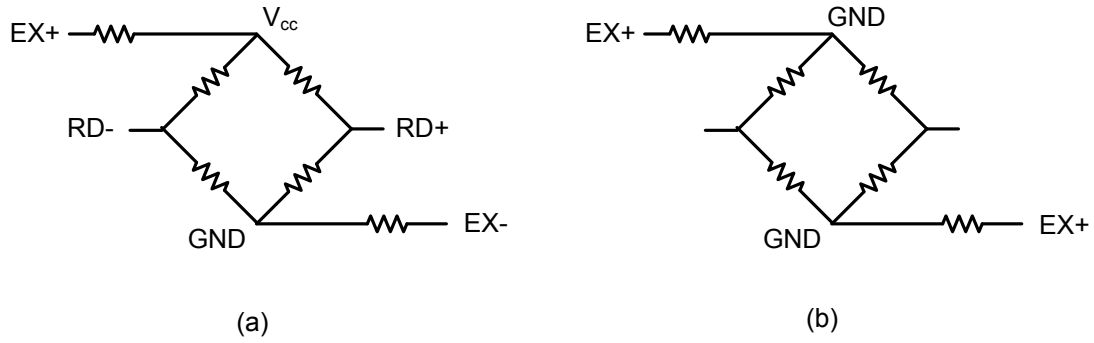

Figure 23: Excitation scheme for normal closed-loop operation (a) compared with that used for stroboscopic and vibrometric measurements (b). In (b), the Wheatstone bridge is shorted by applying ground to both of the power inputs and the same excitation signal is applied to both excitation resistors.

3.4.3.1 In-plane Deflection of the Disk Resonator

Stroboscopic measurements using the MSA-500 system were used to determine the in-plane deflection of the disk resonator when resonating in its rotational in-plane resonance mode. Measurements of the deflection of the in-plane resonance mode were taken at the tip of the half-disks as shown in Figure 24.

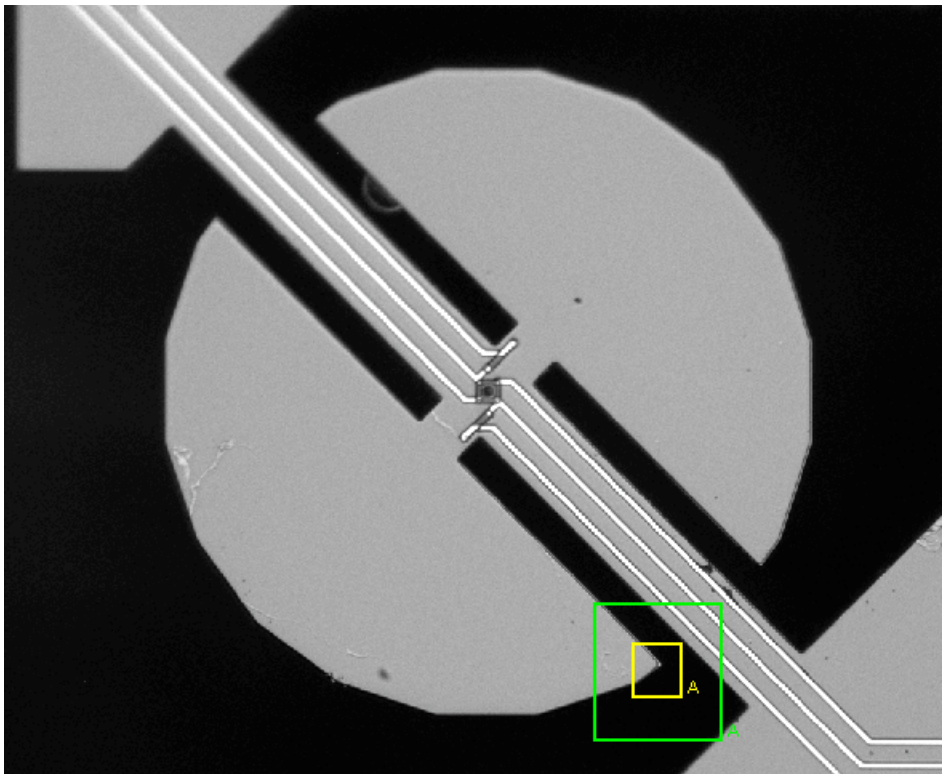

Figure 24: Measurement area on the disk resonator for assessing the deflection of the rotational in-plane resonance mode.

Figure 25 shows a transfer characteristic obtained from a stroboscopic measurement of the in-plane deflection of the disk resonator around its rotational in-plane resonance frequency. The displacement shown is the total in-plane displacement of the half-disk tip (i.e. $\sqrt{x^2+y^2}$). The tested disk resonator has a silicon thickness of 18 μm and a disk radius of 170 μm. To actuate the rotational in-plane resonance mode, a sinusoidal signal with a DC offset was applied to the two excitation resistors on the resonator. For the device shown in the following measurements, the resistance of each excitation resistor was approximately 550 Ω. The applied voltage had the form $V = V_{ac}sin(\omega t) + V_{dc}$. The total power dissipation

for a single resistor is

$$P_{total} = P_{static} + P_{dynamic} = \frac{1}{R}\left(V_{dc}^2 + \frac{1}{2}V_{ac}^2\right) + \frac{1}{R}\left(2V_{dc}V_{ac}sin(\omega t) + \frac{1}{2}V_{ac}^2 sin(2\omega t)\right) \quad (46)$$

In (46), P_{static} is the power dissipation due to DC currents, and $P_{dynamic}$ is the power dissipation due to AC currents. Only the first term of the dynamic power dissipation, i.e. $2V_{dc}V_{ac}sin(\omega t)$, is used in the calculation of dynamic power, as the thermal wave generated by the second term has a negligible effect on the disk excitation due to its small thermal penetration depth [102].

For the transfer characteristic shown in Figure 25, $V_{ac} = 2V$ and $V_{dc} = 2V$, giving a total of 21.8 mW static heating power and 20.5 mW rms dynamic heating power from the two excitation resistors.

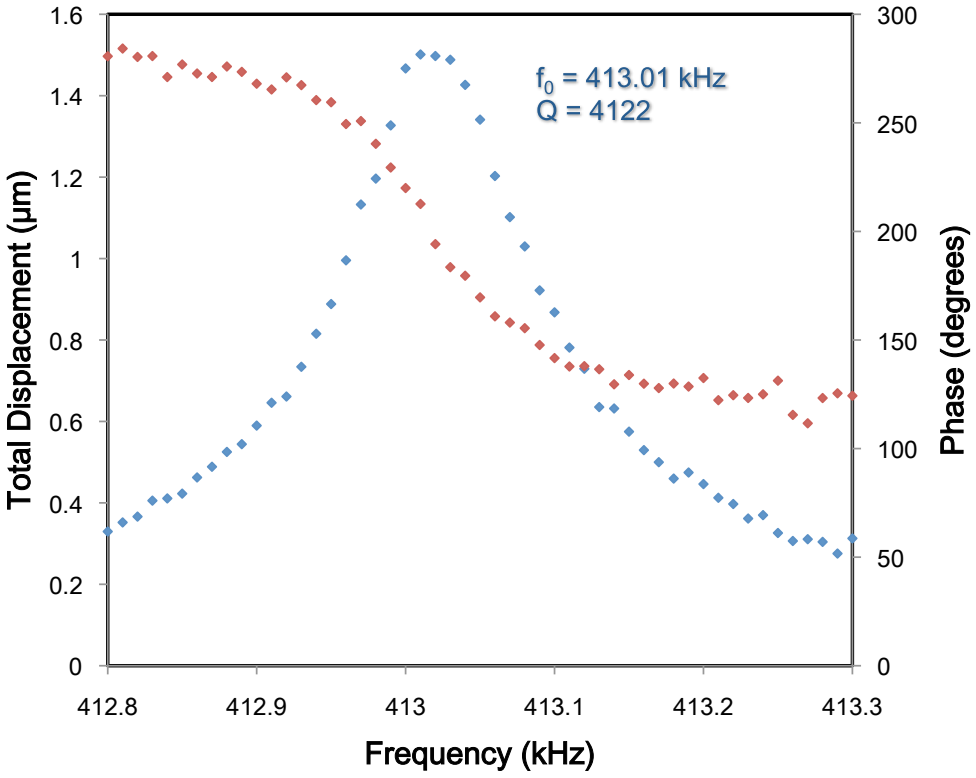

Figure 25: Stroboscopic measurement of the in-plane deflection of the rotational in-plane resonance mode at the tip of a half-disk on a disk resonator with a disk radius of 170 μm and silicon thickness of 18 μm. The applied dynamic power is 20.5 mW rms.

Figure 26 shows the total displacement of the tip of the same disk resonator with various excitation powers applied to it. At the rotational in-plane resonance frequency ($f_o \approx 413$ kHz), the in-plane deflection is on the order of microns for the excitation powers applied. The applied excitation powers and maximum in-plane tip deflection at each power are summarized in Table 7. The power-deflection relationship is almost linear. Comparing the results of this section with those of the following section, the actuation efficiency for the rotational in-plane resonance mode can be calculated. At a given input power, the in-plane deflection can be expected to be 100 times greater than the out-of-plane deflection for the rotational in-plane resonance mode. This comparison between the in-plane deflection and out-of-plane deflection is performed at the half-disk tip.

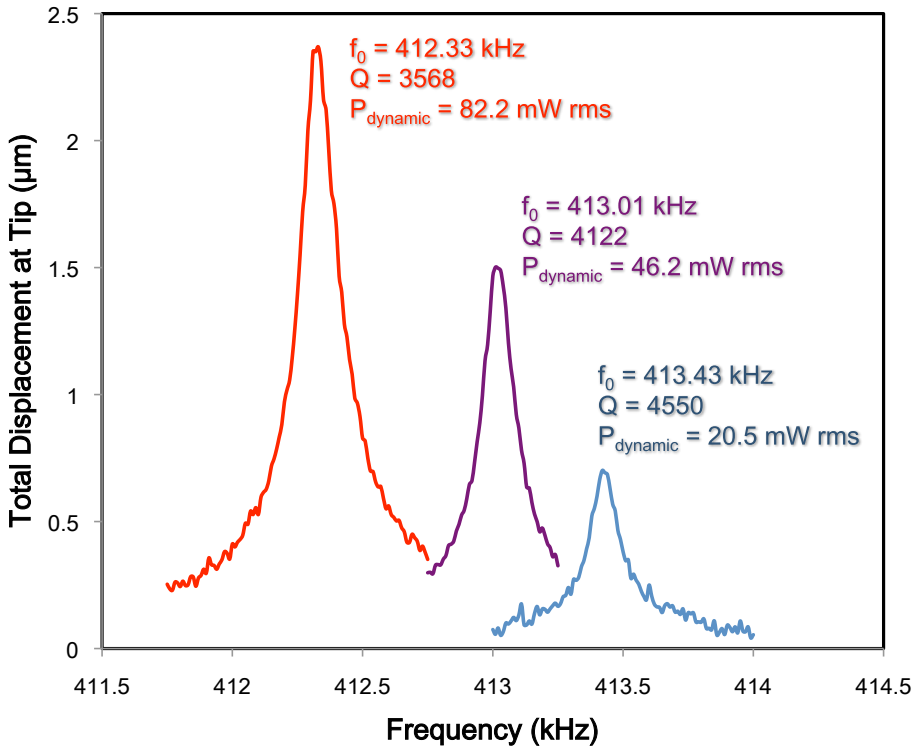

Figure 26: In-plane displacement responses of the rotational in-plane resonance mode at the tip of a half-disk of a disk resonator with $r_o = 170\mu$m and $t_{Si} = 18\mu$m. The Q-factor and resonance frequency decreases while the displacement amplitude increases with increasing thermal excitation power. Displacement amplitude is the total displacement distance (i.e. $\sqrt{x^2 + y^2}$).

With increasing excitation power, the Q-factor suffers a decrease not solely attributable

Table 7: Characteristics of the Rotational In-plane Resonance Mode as a Function of Applied Excitation Power (radius 170 μm, silicon thickness 18 μm, Resistance 550 Ω)

V_{ac}	V_{dc}	Static Power (mW)	Dynamic Power (mW rms)	Resonance Frequency (kHz)	Q-factor	Tip Deflection (μm)
2	2	21.8	20.5	413.43	4550	0.7
3	3	49	46.2	413.01	4122	1.5
4	4	87.2	82.2	412.33	3568	2.3

to a decrease in the stiffness of the structure due to heating. In the case of a simple stiffness change, the effective mass of the structure and the damping would remain approximately constant. Assuming a simple change in stiffness with static heating power, the following equation should hold

$$\frac{f_{heated} - f_{nominal}}{f_{nominal}} = \frac{\sqrt{\frac{K_{heated}}{M}} - \sqrt{\frac{K_{nominal}}{M}}}{\sqrt{\frac{K_{nominal}}{M}}} \tag{47}$$

It follows then that

$$\frac{f_{heated}}{f_{nominal}} = \sqrt{\frac{K_{heated}}{K_{nominal}}} \tag{48}$$

Since $Q = \frac{\sqrt{MK}}{D}$ (see Chapter 2), and only a change in stiffness is assumed, the following must be true under the assumption of constant mass and damping

$$\frac{Q_{heated}}{Q_{nominal}} = \frac{f_{heated}}{f_{nominal}} \tag{49}$$

Comparing the data for 21.8 and 87.2 mW of static heating power, it can be seen that $\frac{Q_{87.2mW}}{Q_{21.8mW}} = 0.78 < \frac{f_{87.2mW}}{f_{21.8mW}} = 0.99$.

Since a large mass change is not plausible, an increase in damping must be present when the 87.2 mW of static power is applied. This damping mechanism is possibly squeeze-film damping at large deflections from compression of the air in the small gap spaces between the main support beam and the half-disks. Alternatively, a non-linear stiffness effect such as stress stiffening or stress softening might be present due to the large amplitude deflections at higher excitation powers. Given the data, the half-disk deflection should be kept in the sub-micron regime to maintain high Q-factors.

3.4.3.2 Out-of-plane Deflection of the Disk Resonator

The design of the disk resonator is intended to minimize viscous losses by resonating in a rotational in-plane resonance mode that primarily has in-plane deflections. It is therefore important that out-of-plane deflections of the rotational in-plane resonance mode be quantified and minimized.

The out-of-plane deflection of the disk resonator is non-zero at the resonance frequency of the rotational in-plane resonance mode. This is shown through both simulation and measurement. Figure 27 shows the out-of-plane components of the rotational in-plane resonance mode as predicted by FEM simulation. In the simulation, the rotational in-plane resonance mode has been simulated using a modal analysis. The simulated structure is composed entirely of silicon with no dielectrics, and only the u_z (out-of-plane) component is displayed (i.e. the u_x and u_y displacements are not displayed). The absolute magnitude of this out-of-plane deflection cannot be obtained by the modal analysis, since modal analyses only give the deflection of the various nodes on a structure relative to each other [68]. The simulated disk radius is 170 μm and the disk thickness is 18 μm. Isotropic silicon properties are used in the simulation, and the resulting resonance frequency of the rotational in-plane resonance mode is simulated to be 398 kHz.

The simulation serves to confirm that for the rotational in-plane resonance mode of the silicon disk resonator without dielectrics, a finite out-of-plane displacement can be mathematically predicted. In both measurement and simulation, the shape of the out-of-plane displacement of the rotational in-plane resonance mode is similar to that of out-of-plane resonance modes that are near in frequency to the rotational in-plane resonance mode. This indicates that nearby out-of-plane resonance modes may contribute low-amplitude vibrations when the rotational in-plane resonance mode is excited to full resonance.

The FEM simulation of Figure 27 shows both half-disks performing torsional rotations about their respective anchor beams. The rotations are out-of-phase which each other. Using the same FEM model, the out-of-plane resonance mode at 397 kHz is displayed in Figure 28. The resonance mode of Figure 28 directly neighbors in frequency the rotational in-plane resonance mode simulated in Figure 27. In Figure 28, all the deflection components

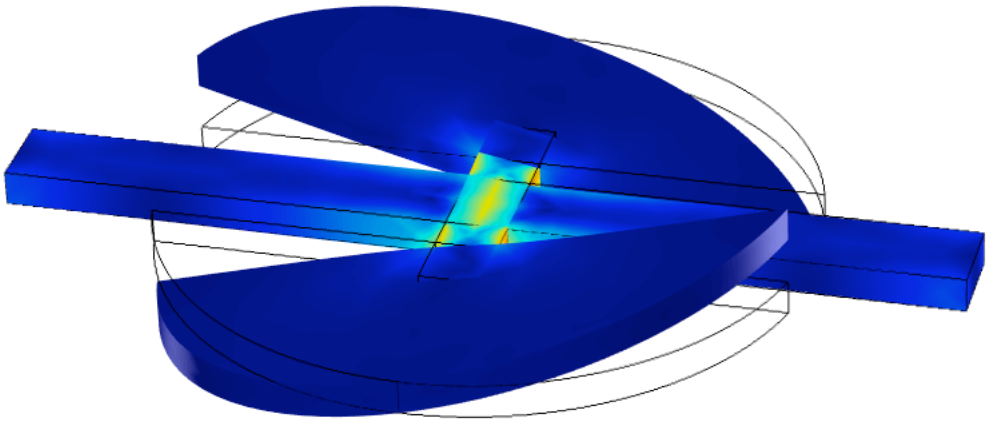

Figure 27: FEM simulation of the out-of-plane component of the rotational in-plane resonance mode for a disk resonator with $r_o = 170\mu$m and $t_{Si} = 18\mu$m. The displayed deflection is such that the in-plane components are not visible. Coloring represents the von Mises stress. The wireframe is the undeformed shape of the resonator.

are displayed, and the u_z deflection of the resonance mode is naturally prominent. The u_z deflection need not be emphasized by negating in-plane displacements, as is done with the rotational in-plane resonance mode displayed in Figure 27.

The similarity in the shape of the u_z components of both resonance modes supports the hypothesis that nearby out-of-plane resonance modes may undergo low-amplitude vibrations when the rotational in-plane resonance mode is fully excited. This is supported by the laser vibrometry measurement of Figure 29, which shows out-of-plane displacements when the rotational in-plane resonance mode of the resonator is excited. The measured device is the same device on which the in-plane stroboscopic measurements were performed in the previous section. The match in resonance frequencies between the stroboscopic and laser vibrometry measurements confirm that the rotational in-plane resonance mode is being

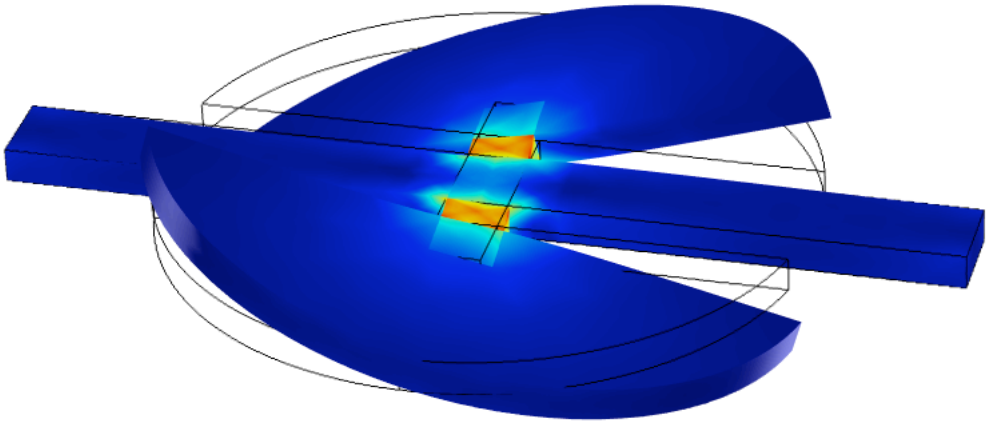

Figure 28: FEM simulation of an out-of-plane resonance mode for a disk resonator with $r_o = 170\mu$m and $t_{Si} = 18\mu$m. The displayed mode is 1 kHz lower in frequency than the rotational in-plane resonance mode under the simulation conditions. All directions of deflection are displayed. Coloring represents the von Mises stress. The wireframe is the undeformed shape of the resonator.

excited in this measurement.

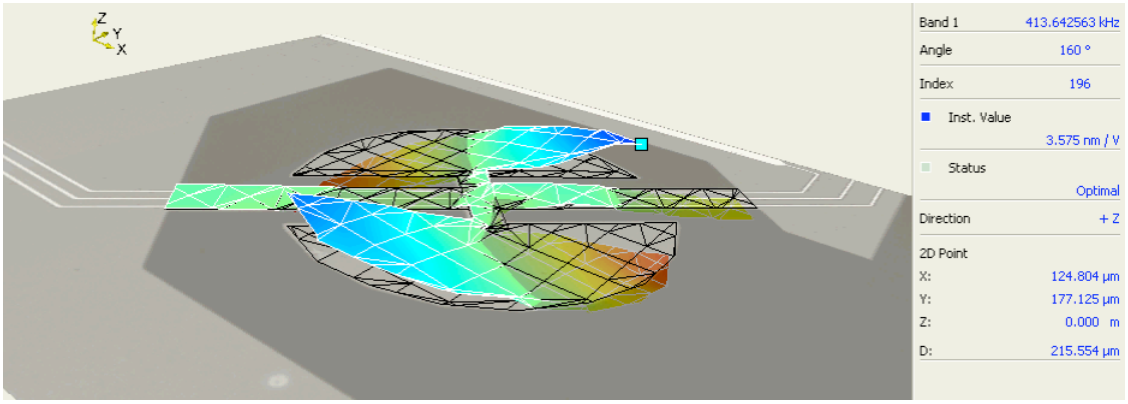

Figure 29: Laser vibrometry measurement of the out-of-plane deflection of a disk resonator operated at its rotational in-plane resonance mode. The resonance frequency is 413.6 kHz. The disk dimensions are $r_o = 170\mu$m and $t_{Si} = 18\mu$m.

The deflection of the entire surface of the disk resonator is obtained by an iterated point-by-point measurement over the device surface. The out-of-plane deflection may be exaggerated by the resonator plane being uneven relative to the laser reflection, which would tend to register in-plane deflections as out-of-plane deflections.

The deflection displayed in Figure 29 is quantified by taking vibrometry measurements at specific points on the disk resonator surface. The deflection of the disk resonator at three distinct points on the surface when resonating in its rotational in-plane resonance mode is shown in Figure 30. The deflection is given in units of μm/V. 1 V of input signal in this case corresponds to 5.1 mW rms of equivalent dynamic input power. The measurements of Figure 30 are again from the same device as Figure 29.

The out-of-plane deflection at the tip of the half-disk is shown to be an order of magnitude greater than that of the substrate-clamped portion of the support beam or that of the disk center. The half-disk tip is the highlighted area shown in Figure 24. The deflection at the half-disk tip is 3 nm, as opposed to 0.4 nm for the disk center and 0.2 nm for the subtrate-clamped anchor. Comparing the in-plane and out-of-plane deflections at the half-disk tip, this corresponds to a $\approx$ 100:1 actuation efficiency for the rotational in-plane resonance mode. This efficiency calculation scales the measured out-of-plane deflections by 4x to equate the dynamic input excitation powers to those used for the measurement of the in-plane deflections, which are tabulated in the previous section in Table 7.

The out-of-plane deflection data presented in this section has possible implications for the viscous damping of the disk resonators. The spread in $Q^{-1}_{viscous}$ data for nominally identical disk resonators in Figure 16 may be explained by the finite out-of-plane deflection of the disk resonators when resonating in their rotational in-plane resonance mode. Such deflections could vary from device to device as a result of geometric defects, thus producing a spread in the $Q^{-1}_{viscous}$ data.

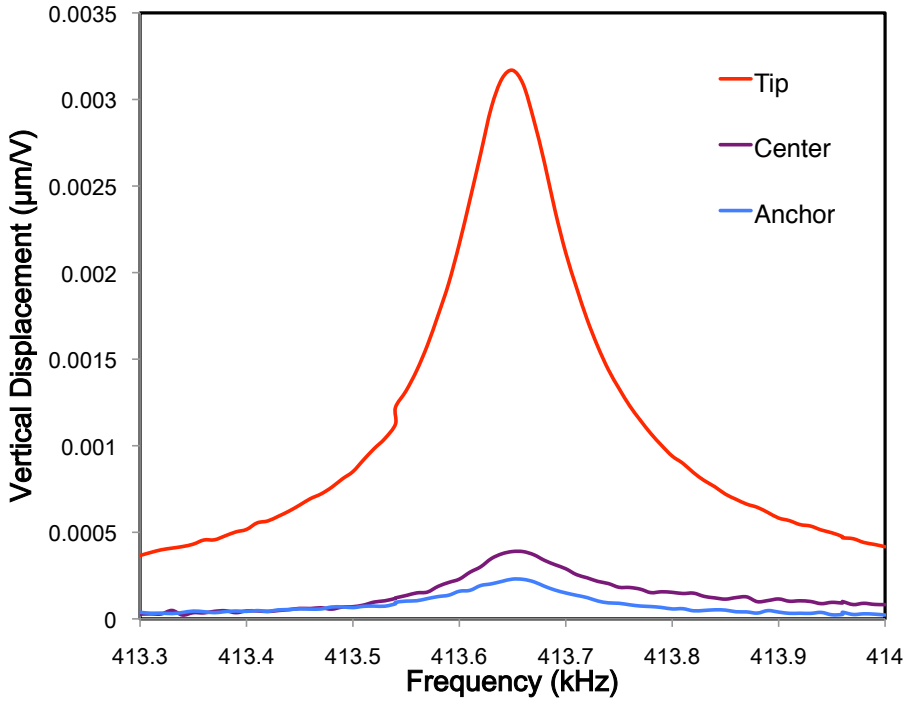

Figure 30: Out-of-plane displacement responses at the half-disk tip, disk center, and clamped portion the anchor beam of a half-disk of a disk resonator with $r_o = 170\mu$m and $t_{Si} = 18\mu$m. The resonator is excited around the resonance frequency of its rotational in-plane resonance mode.

3.5 Chapter Summary

This chapter presented theoretical and physical characterization results for the disk resonator with respect to the Q-factor and dynamic deflection of the rotational in-plane resonance mode. The theories of viscous damping, anchor loss, and frequency noise were presented. Experimental results showing the viscous damping of the rotational in-plane resonance mode as a function of resonance frequency and geometrical parameters of the disk resonator were presented. The dependency of the total Q-factor and anchor loss of the rotational in-plane resonance mode on the disk resonator geometrical parameters was also presented. Lastly, measurements of the deflection experienced by the resonator when oscillating in its rotational in-plane resonance mode were shown. The main points to be derived from this chapter follow:

- The viscous damping for disk resonators and cantilever beams can be seen as a function

of resonance frequency and resonance mode shape. Generally, a $\frac{1}{\sqrt{f}}$ dependence of the viscous damping is observed for both in-plane and out-of-plane resonance modes.

- The Q-factor of the rotational in-plane resonance mode of the disk resonator can be improved by increasing the resonator silicon thickness. However, in order to minimize the relative viscous damping resulting from fluid forces on the disk sidewalls, the silicon thickness should not approach the order of the lateral dimensions of the device. As a lower limit, the thickness dimension should be greater than the fluid boundary layer thickness. Stated succinctly: $\delta < t_{Si} << l_{lateral}$.

- For the disk resonator, the disk radius that optimizes the Q-factor of the rotational in-plane resonance mode is 170 μm for the range of devices tested in this work.

- The anchor loss for the rotational in-plane resonance mode of the disk resonator does not vary with the resonator silicon thickness, and is mainly due to the central clamped-clamped anchor beam. The anchor loss-limited Q-factor of the rotational in-plane resonance mode of the disk resonators is on the order of 10000. This can be modified through optimization of the lateral geometry of the disk resonator.

- For typical operating input powers, the in-plane deflection of the disk resonator in its rotational in-plane resonance mode is 100's of nanometers. This is compared to an out-of-plane deflection of single nanometers for the rotational in-plane resonance mode. Thus the actuation efficiency for the rotational in-plane resonance mode is $\approx$ 100:1.

The characterization results of this chapter give a better understanding of what device parameters should be used for optimal application of the disk resonators as gas-phase chemical sensors. Chapter 4 explores this application.

CHAPTER IV

CHEMICAL SENSING BEHAVIOR OF THE DISK RESONATOR

4.1 Introduction

In this chapter, the performance of the silicon disk resonator as a gas-phase chemical sensor is presented. The detection principle of physisorption through the use of polymer films is first described. A mathematical model is then developed for both the chemical sensitivity and limit of detection (LOD) of the disk resonator. Finally, experimental results are presented showing the chemical sensitivity, limit of detection, and transient response of the polymer-coated disk resonator to the gaseous VOC toluene. Limits of detection and calibration curves are also presented for benzene, toluene, and m-xylene.

4.2 Analyte Sorption

Gravimetric chemical sensors detect the mass of a target analyte, requiring a mechanical contact between the sensor structure and the analyte. In this research, the mechanical contact is facilitated by the thermodynamic tendency of gaseous VOCs to diffuse into solid media such as polymers. Thus, polymer films can be used to absorb the target analyte onto the sensor surface. Sensors with polymer films applied to their surface for the purpose of analyte sorption are said to be *functionalized*. It therefore becomes desirable to choose polymers that have strong sorption characteristics for the analyte under consideration.

The strength of the thermodynamic force driving the diffusion of the analyte into a given polymer film is characterized by the partition coefficient K. The partition coefficient is an equilibrium constant describing the ratio of the concentration of the analyte in the polymer matrix to its concentration in the surrounding fluid solution, i.e.

$$K = \frac{c_{poly}}{c_{fluid}} \tag{50}$$

where c_{poly} is the concentration of the analyte in the polymer matrix and c_{fluid} is the

concentration of the analyte in the fluid solution. To achieve a high sensitivity to a particular analyte, one should generally choose a polymer film that has a high partition coefficient for that analyte .

Partition coefficients follow a general trend relating to the relative polarities of the polymer film and the analyte. Polar analytes tend to sorb into polar polymer films, and non-polar analytes tend to sorb into non-polar polymer films. A large literature exists with measurements and estimates of partition coefficients for different analyte-polymer pairs, both in the liquid and gas phases. Table 8 summarizes liquid and gas-phase partition coefficients for some common polymers and VOCs. The polymers listed in Table 8 are (poly)isobutylene (PIB), (poly)dimethylsiloxane (PDMS), (poly)epichlorohydrin (PECH), and (poly)etherurethane (PEUT).

In Table 8, $K_{g\rightarrow p}$ is the gas-phase partition coefficient and $K_{l\rightarrow p}$ is the liquid-phase partition coefficient for the respective analyte-polymer pair. Table 8 assumes standard atmospheric pressure and a temperature of 300 K for the gas-phase partition coefficients. There are sometimes significant deviations in the experimental values reported, as partition coefficients can be affected by many factors. These factors include the sensing method employed, the thickness of the polymer film, and the material properties of the particular polymer formulation used, such as its molecular weight. However, for practical experiments focusing on the physical transducer, the values found in [103, 105, 107] are used in this research.

The thermodynamic driving force causing the analyte to be absorbed into the polymer is quantified by the Gibb's sorption energy $\Delta G_{sorption}$, which has a slight temperature dependence. The Gibbs sorption energy is related to the partition coefficient K through the following equation [109],

$$lnK = -\frac{\Delta G_{sorption}}{RT} \tag{51}$$

In (51), R is the ideal gas constant and T is absolute temperature. The temperature dependence of K makes heating of the sorbent polymer layer undesirable, as this would reduce the partition coefficient. Thus, to maintain high chemical sensitivity, sensors using

Table 8: Partition coefficients for key sorbent polymers and VOCs

	PIB		PDMS		PECH		PEUT	
	$K_{g\to p}$	$K_{l\to p}$	$K_{g\to p}$	$K_{l\to p}$	$K_{g\to p}$	$K_{l\to p}$	$K_{g\to p}$	$K_{l\to p}$
benzene	360 [103], 799 [104]		400 [105], 296 [106]				710 [103]	
xylenes	2137 [107], 3400 [103], 7260 [104]	458 [107]	2785 [107], 3200 [105], 2190 [106]	743 [107]	3284 [107]	700 [107]	5200 [103]	
toluene	583 [107], 1030 [103], 1000 [108], 2460 [104]	140 [107]	1164 [107], 1200 [105], 1870 [108], 815 [106]	279 [107]	1040 [107], 1670 [108]	249 [107]	1750 [103]	
ethylbenzene	1672 [107]	464 [107]	3153 [107], 2020 [106]	772 [107]	2425 [107]	673 [107]		
nitrobenzene	256 [107]	0.75 [107]	526 [107]	1.5 [107]	3482 [107]	10 [107]		
n-octane	1720 [103]		2200 [105]				950 [103]	
ethanol			180 [109]				700 [110]	

polymeric sorbent films should avoid any heating of the film.

4.3 Mass-Sensitive Behavior

The chemical sensitivity of the disk resonator is quantified as a change in resonance frequency per unit of analyte concentration. The rotational in-plane resonance frequency of the disk resonator is determined by the effective rotational stiffness, K_r, and the effective rotational inertia, J, of the resonator structure. Rotational inertia is used in place of mass because it better describes the rotational in-plane resonance mode of the disk resonator. The following equations are generally valid for resonators in a rotational in-plane resonance

mode using polymer layers to absorb gas-phase analytes.

The rotational in-plane resonance frequency is stated in terms of K_r and J as follows

$$f_o = \frac{1}{2\pi}\sqrt{\frac{K_r}{J}} \tag{52}$$

Upon analyte sorption, the change in the rotational inertia is the primary contributor to the change in resonance frequency of the rotational in-plane resonance mode. Changes in the elastic modulus, and hence K_r, of the resonator also occur with sorption, especially in the case of thick sorption films, but this is considered a non-dominating effect in this analysis. Therefore it is the change in rotational inertia that is of primary consideration in deriving the resonator's chemical sensitivity. The nominal rotational inertia of the layered microstructure can be described by the following equation

$$J_o = (\rho_{Si} t_{Si} + \rho_{poly} t_{poly}) \int_A r^2 \, dA, \tag{53}$$

where ρ_{Si} and t_{Si} are the silicon density and silicon thickness, respectively, of the resonator, and ρ_{poly} and t_{poly} are the density and thickness, respectively, of the polymer layer. For simplicity, the dielectric layers of the resonator structure are neglected in this analysis. The integral of (53) is taken over the lateral geometry of the resonator. The sorption of the analyte by the polymer primarily creates a change in the polymer density through the dissolution of the analyte molecules into the polymer matrix. The change in polymer density is denoted by $\Delta\rho_{poly}$. The following equation describes the proportional change in mass per unit area on the resonator surface due to mass absorption

$$\Delta = \frac{\Delta\rho_{poly} t_{poly}}{\rho_{Si} t_{Si} + \rho_{poly} t_{poly}} \tag{54}$$

It follows that the rotational inertia after analyte sorption can be reduced to the following form

$$J = J_o(1 + \Delta) \tag{55}$$

From (55) it then follows that the new resonance frequency after mass absorption has the following form

$$f = \frac{1}{2\pi}\sqrt{\frac{K_r}{J}} = \frac{1}{2\pi}\sqrt{\frac{K_r}{J_o(1+\Delta)}} = \frac{1}{2\pi}\sqrt{\frac{K_r}{J}}\sqrt{\frac{1}{1+\Delta}} \approx f_o(1-\frac{1}{2}\Delta) \tag{56}$$

where the last step is an approximation afforded by a Taylor series expansion. Thus, the relative frequency change due to the change in polymer density is

$$\frac{\Delta f}{f_o} = -\frac{1}{2}\frac{\Delta\rho_{poly}t_{poly}}{\rho_{Si}t_{Si}+\rho_{poly}t_{poly}} \tag{57}$$

Since the above equation is completely independent of the lateral geometric parameters of the resonator or polymer layer, it follows that relative resonance frequency changes due to mass absorption are independent of the resonator-polymer lateral geometry (assuming the layers of the structure are uniform). Rearranging the above equation to obtain a frequency change per unit of analyte concentration, the chemical sensitivity S can be expressed as

$$S = \frac{\Delta f}{\Delta C} = -\frac{1}{2}\frac{f_o}{\Delta C}\frac{\Delta\rho_{poly}t_{poly}}{\rho_{Si}t_{Si}+\rho_{poly}t_{poly}} = -\frac{1}{2}f_o\frac{\Delta\rho_{poly}}{\Delta C}\frac{t_{poly}}{\rho_{Si}t_{Si}+\rho_{poly}t_{poly}}, \tag{58}$$

where ΔC is the change of the analyte concentration. $\frac{\Delta\rho_{poly}}{\Delta C}$ depends solely on the sorption characteristics of the polymer with respect to the analyte of interest, and describes the density change of the polymer subject to a given change in analyte concentration. To a first order, S increases linearly with the polymer thickness t_{poly}. The polymer thickness term in the denominator will lead to a decrease in the incremental sensitivity for thick polymer layers, causing a non-linearity in the equation. Assuming a thin polymer film (compared to the silicon thickness), the chemical sensitivity becomes a linear function of the ratio of polymer thickness to silicon thickness.

Furthermore, the ratio $\frac{\Delta\rho_{poly}}{\Delta C}$ from (58) can be written as a function of the partition coefficient K using the ideal gas law, yielding the following simplified equation for S

$$S = -\frac{1}{2}\frac{f_o}{\rho_{Si}}\frac{KM_aP}{RT}\left(\frac{t_{poly}}{t_{Si}}\right), \left[Hz/\frac{g}{L}\right] \tag{59}$$

where K is the analyte-polymer-specific partition coefficient, M_a is the molar mass of the analyte, P is the ambient pressure, R is the ideal gas constant, and T is the absolute temperature. (59) has units of $Hz/\frac{g}{L}$. By introducing a factor of 10^6 in the denominator, the chemical sensitivity in units of Hz/ppm can be obtained.

From (58), it can be shown that resonators with higher resonance frequencies should have higher chemical sensitivities due to the linear dependence of S on resonance frequency. A possible way to achieve these apparent higher chemical sensitivities would be to change the lateral geometry of the resonator to achieve higher resonance frequencies. However, the apparent chemical sensitivity gain from this approach is misleading.

From (58), one can derive a normalized sensitivity, $\frac{S}{f_o}$, which is completely invariant with respect to the resonator's lateral geometry. The dependence on lateral geometry through f_o is cancelled in this new quantity, which can thus be used to show that lateral geometric variation will yield no improvement in relative chemical sensitivity [111]. That is, $\frac{\Delta f}{f_o}$ is constant across all lateral geometries for a given $\frac{t_{poly}}{t_{Si}}$ and ΔC. Thus, optimization of chemical sensitivity can only be achieved by manipulating $\frac{t_{poly}}{t_{Si}}$ for resonators with rotational in-plane resonance modes, or by optimizing the analyte-polymer interaction described by $\frac{\Delta \rho_{poly}}{\Delta C}$.

4.4 Experimental Apparatus for Analyte Exposure

4.4.1 Polymer Coating

To functionalize the disk resonators with an analyte-absorbing polymer layer, the resonator dies are packaged in a 28-pin dual in-line (DIL) package and placed in a spray-coating setup. The spray-coating setup consists of a commercially available airbrush vertically mounted on a stand. The vertical mounting allows for the polymer solution to be sprayed directly onto the resonator surface without the polymer subsequently creeping into the small gaps of the resonator geometry. The polymer used is (poly)isobutylene (PIB) (Sigma-Aldrich) dissolved in a 0.01% w/v solution with toluene. The toluene evaporates from the solution after spray-coating, leaving a pure polymer layer behind. For each polymer coating of the disk resonator, a reference sample is also coated in order to measure the polymer thickness

with a profilometer.

4.4.2 Analyte Testing

The coated disk resonators are exposed to controlled analyte vapor concentrations using a custom-made gas manifold system. The gas manifold system consists of a supply of nitrogen (Airgas, ultra high purity), which is fed to a system of mass-flow controlled gas lines which connect to a measurement chamber. The nitrogen acts as a carrier gas for analyte dilution. This is accomplished by feeding mass-flow-controlled carrier gas to an analyte-containing bubbler, in which a quartz sand matrix is soaked with the desired analyte. The analyte vapor mixes with the carrier gas when the carrier gas passes through the sand matrix. In the bubbler, the analyte vapor reaches a temperature-dependent equilibrium concentration in the carrier gas. The bubbler temperature is controlled by a room-temperature water bath kept at 22°C. The corresponding equilibrium concentration for a particular analyte is calculated by using the Antoine coefficients specific to that analyte [112]. This equilibrium analyte concentration is further reduced through the controlled addition of carrier gas after the bubbler, resulting in a controlled analyte concentration which is periodically pulsed into the measurement chamber using a 4-way valve. When analyte injection into the measurement chamber is not occurring, a secondary line supplies pure carrier gas to the measurement chamber. The measurement chamber contains the resonator operating in a closed amplifying feedback loop [75]. A schematic of the gas-manifold system is shown in Figure 31.

Analytes used during the experiments included benzene (Sigma-Aldrich, CAS 270709), toluene (VWR, CAS 108883), and m-xylene (Sigma-Aldrich, CAS 108383).

4.5 Analyte Sensing Results

4.5.1 Chemical Sensitivity

Given the results of the physical characterization and geometrical optimization from the previous chapter, disk resonators with a radius of 170 μm are chosen for the chemical sensing experiments. The disk resonators were coated with several layers of PIB and exposed to linearly-increasing concentrations of toluene vapor in the gas phase. The concentrations

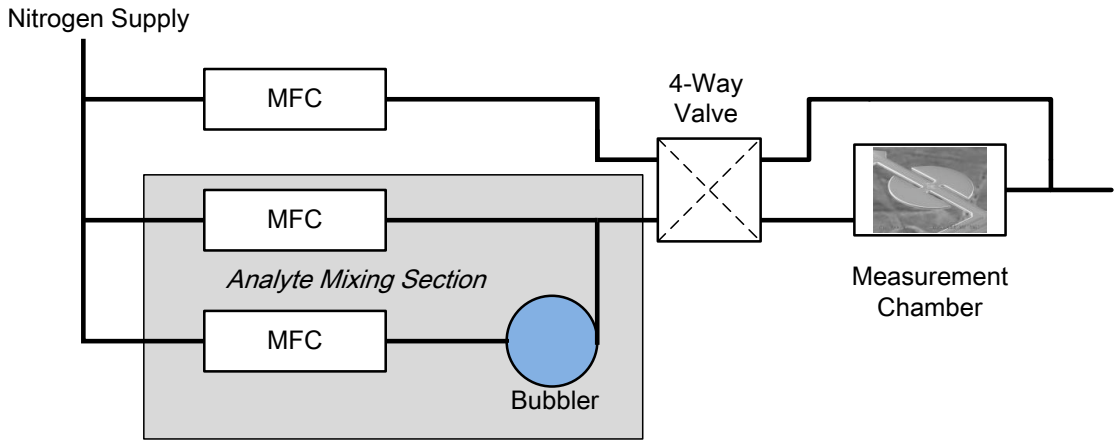

Figure 31: Schematic of the gas manifold system used in this research.

range from 2000 ppm to 16000 ppm of toluene. For each new additional layer of PIB applied, a new test is undertaken. Figure 32 shows a transient response from a typical test, with toluene being exposed to a resonator with $r = 170\mu$m, $t_{Si} = 7\mu$m, and a coated PIB thickness of 3.4 μm. The uncoated resonance frequency of the rotational in-plane resonance mode of a resonator with this geometry is between 408-422 kHz. Resonators with two silicon thicknesses, 7 μm and 18 μm, are used to characterize the chemical sensing behavior of the disk resonators for the data presented in this chapter. With each subsequent layer of PIB, the resonance frequency of the resonator decreases, in accordance with (56) (see Figure 33).

With each subsequent polymer coating, the chemical sensitivity increases, but the obtained sensitivities are below the trend expected from (58) . Figure 34 shows the experimentally measured sensitivity for a PIB-coated resonator with 7 μm silicon thickness exposed to toluene. The ideal room-temperature toluene sensitivity, shown as a dashed line, is based on (58) using a room temperature value of the PIB-toluene partition coefficient K. This room-temperature toluene sensitivity is strictly higher than the experimentally measured values.

The cause of this relative decrease in toluene sensitivity is the heating of the polymer layer by the excitation and sensing resistors used in the resonator structure. Finite element (FEM) simulation results show that a temperature elevation occurs on the surface of the

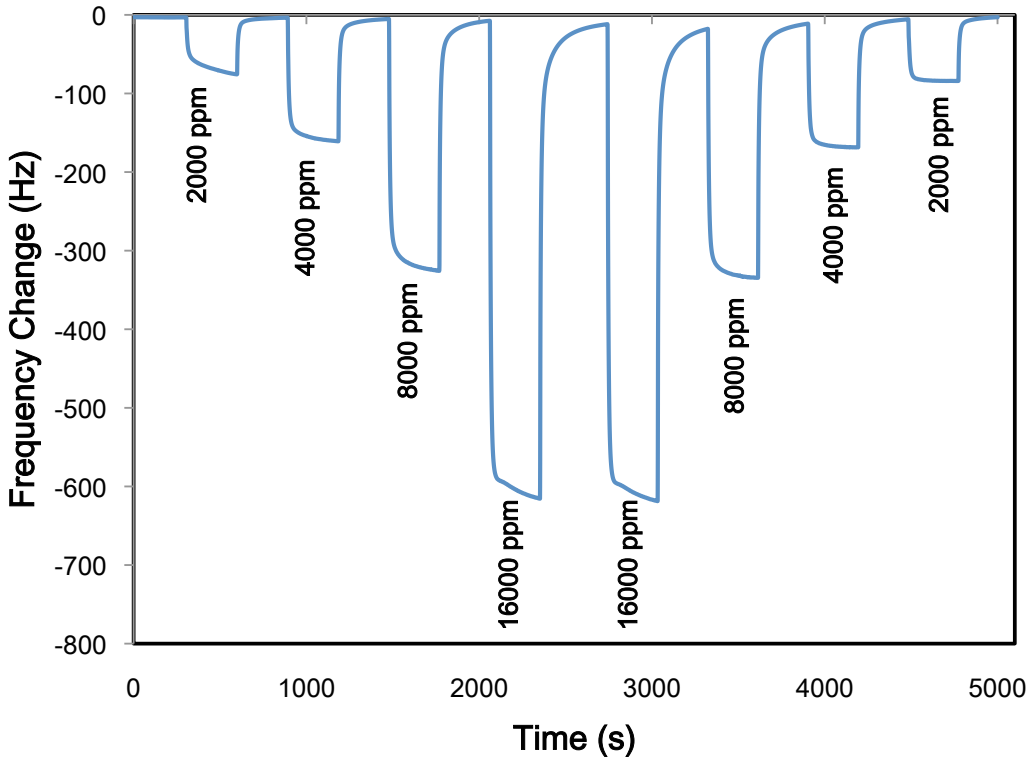

Figure 32: Transient resonance frequency changes due to exposure of various concentrations of toluene vapor to a disk resonator coated with PIB. The disk resonator has $r = 170\mu$m, $t_{Si} = 7\mu$m, and a coated PIB thickness of 3.4 μm.

resonator due to the heat dissipation of the excitation resistors and the Wheatstone bridge. A FEM thermal simulation of the disk resonator using COMSOL is shown in Figure 35. The structure shown is simulated using a 7 μm silicon thickness with a 1 μm thick layer of silicon dioxide on top. No heat dissipation from convection due to the surrounding air is simulated, thus the simulation produces a worst-case temperature elevation. As expected, the results of this simulation show that the temperature elevation on the resonator surface is inversely proportional to the silicon thickness of the resonator. This relationship is due to the increased thermal conductance of thicker conducting structures. Resonators with a 7 μm silicon thickness experience a temperature elevation of approximately 3°C/mW, whereas resonators with an 18 μm silicon thickness experience a temperature elevation of approximately 1.4°C/mW.

Each excitation resistor and Wheatstone bridge resistor of the tested devices has a resistance of 500-600 Ω. During operation, the Wheatstone bridge produces roughly 8 mW

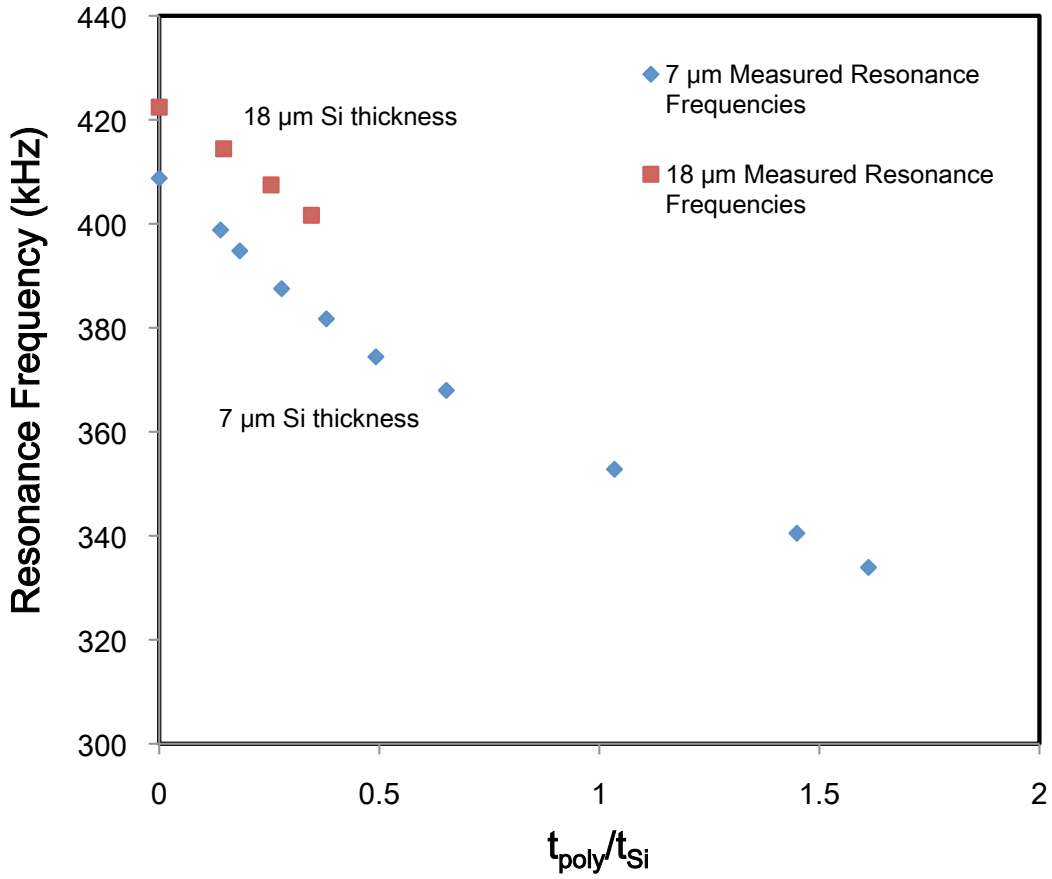

Figure 33: Resonance frequencies of the rotational in-plane resonance mode for two disk resonators of varying silicon thickness (18 μm: red squares, 7 μm: blue diamonds) and 170 μm radius as a function of normalized polymer thickness.

of static heating power and the combined static heating power of the excitation resistors is 3.8 mW. This corresponds to a temperature elevation of roughly 35°C on the surface of the 7 μm resonators and 17°C on the surface of the 18 μm resonators, respectively. This temperature elevation reduces the absorptive effects of the polymer applied to the resonator surface for the purpose of mass-sensing, in accordance with (51).

Using the temperature elevation values from simulation, the effective toluene-PIB partition coefficient should be lowered from published values of 1030 [103] down to 300 for the 7 μm resonator and 666 for the 18 μm resonator, respectively. This heating-corrected partition coefficient is obtained by curve-fitting to previously published partition coefficient data [109]. The temperature dependence of K for the PIB polymer used in this research can

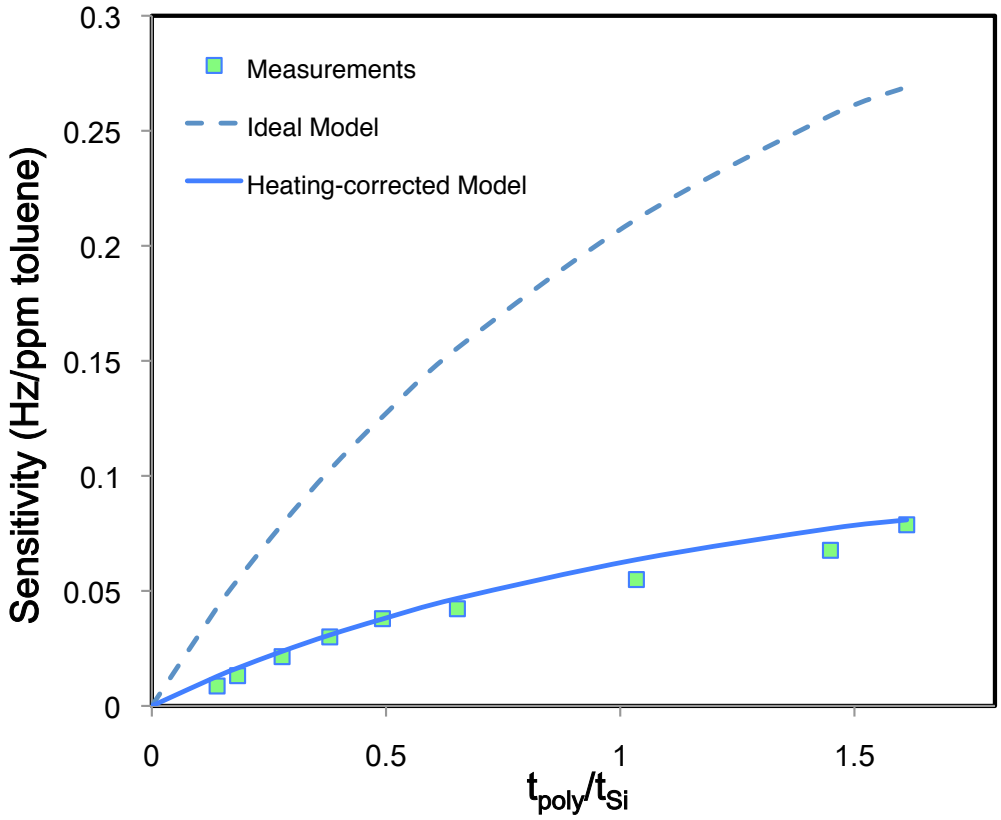

Figure 34: Chemical sensitivity to toluene as a function of normalized polymer thickness, where the dashed line is the non-heating corrected sensitivity predicted from (58), the solid line is the sensitivity predicted by (58) with the heat-adjusted partition coefficient, and the squares are the experimentally measured sensitivities for a disk resonator with 7 μm silicon thickness and a 3.4 μm PIB coating.

be used to extrapolate a new heating-corrected partition coefficient based on the published slopes of $ln(K)$ vs. $\frac{1}{T}$ curves [109]. The heating-corrected partition coefficient yields a heating-corrected sensitivity in closer agreement with the experimentally measured values. The corresponding heat-corrected theoretical chemical sensitivity curve is shown as a solid line in Figure 34 for the resonator with a 7 μm silicon thickness.

Figure 36 shows the experimentally measured toluene sensitivities for PIB-coated resonators as a function of normalized polymer thickness for resonators with 7 μm and 18 μm silicon thicknesses. The heat-adjusted sensitivity models are also included (solid lines), and show close agreement with the experimentally measured sensitivities. In Figure 36,

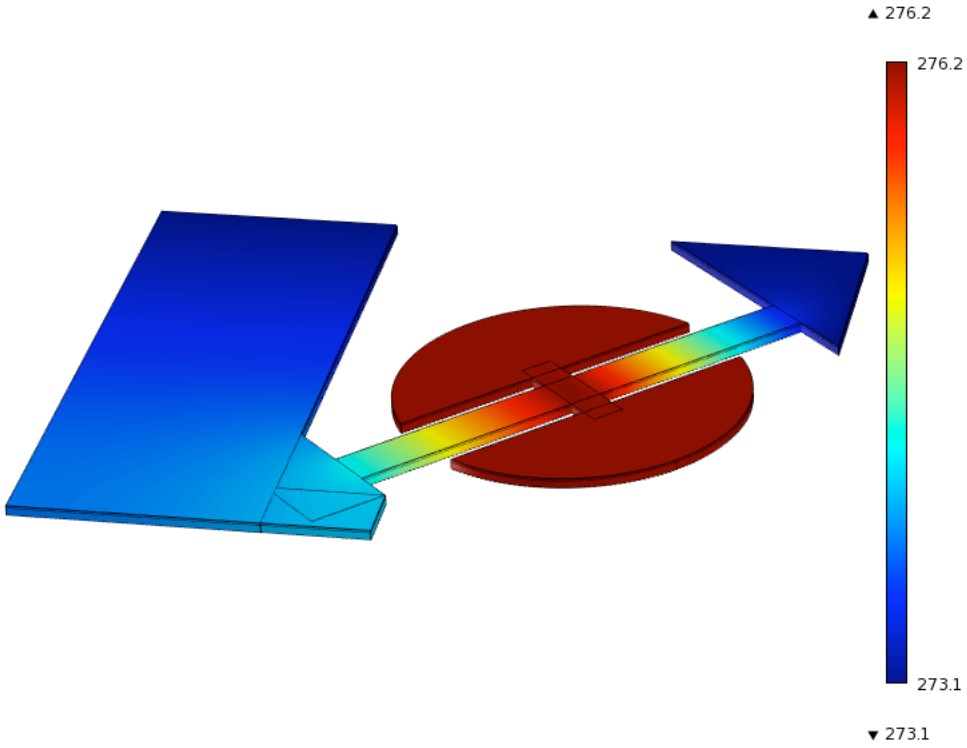

Figure 35: FEM simulation of the temperature elevation of a heated disk resonator with 7 μm silicon thickness and support structures. 1 mW of static heating power is dissipated at the location of the resistors. The maximum temperature elevation is 3° C on the half-disks.

the 18 μm thick disk resonator shows a higher toluene sensitivity than the 7 μm thick disk resonator. This is due to the reduced temperature elevation of the 18 μm thick resonator, which improves the partition coefficient K and results in greater analyte sorption. Neglecting the effects of the temperature elevation on the surface of the disk resonators, the chemical sensitivity of the disk resonators as a function of $\frac{t_{poly}}{t_{Si}}$ should be the same for the two silicon thicknesses presented in the data (see (58) and (59)). However, since the thicker resonator exhibits a reduced temperature elevation, it exhibits higher K and thus higher S.

4.5.2 Limit of Detection

The limit of detection (LOD) for a particular analyte is defined as 3 times the ratio of the chemical sensor system's baseline noise to its analyte-specific sensitivity. For the resonant gravimetric sensors presented in this research, LOD is defined as

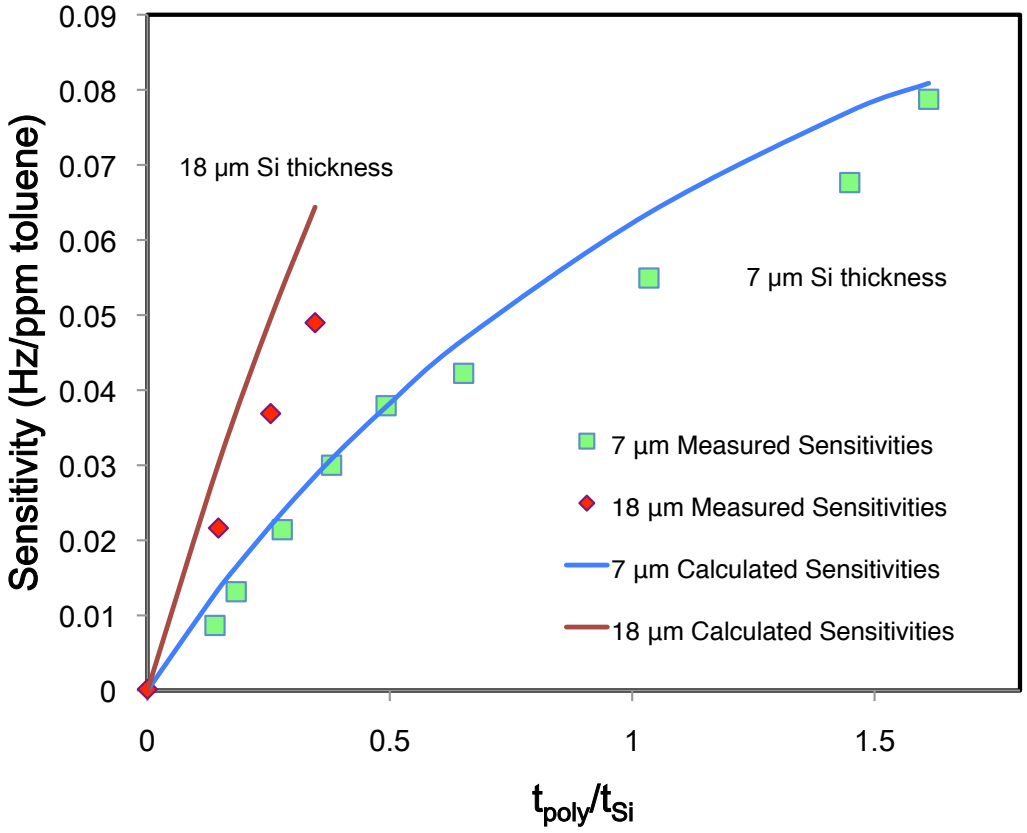

Figure 36: Chemical sensitivity to toluene as a function of normalized polymer thickness for resonators with a silicon thickness of 18 μm (red line: model, purple triangles: experimental) and 7 μm (blue line: model, green squares: experimental).

$$LOD = 3\frac{Var(f_n)}{S} = 3\frac{f_o Var_{Allan}(f_n)}{S}, \tag{60}$$

In (60), $Var(f_n)$ is the absolute frequency variance of the system oscillation frequency, $Var_{Allan}(f_n)$ is the Allan variance, and a pre-factor of 3 is used in order to distinguish frequency changes due to analyte sorption from the noise level. The LOD metric is the ultimate measure of performance for a chemical sensor system.

The LOD of a polymer-coated disk resonator is highly dependent on the thickness of the polymer layer on the resonator surface. The viscoelastic properties of the polymer layer result in the dissipation of mechanical energy from the bulk silicon of the resonator. This effect can be modeled by a $\frac{1}{Q_{polymer}}$ term in (10). The dissipation of the polymer layer results in a reduction of the resonator Q-factor with increasing polymer thickness. The Q-factor

in turn affects the Allan variance, and this is shown in the log-log plot of Figure 37 by a regression of Allan variance on total Q-fcator for a resonator of 7 μm silicon thickness coated with different PIB thicknesses. A $\frac{1}{Q}$ dependence is found for the Allan variance, which is predicted from theory (see Chapter 3) [77, 97]. Figure 38 shows the same relationship for resonators of 7 μm and 18 μm silicon thicknesses coated with different PIB thicknesses.

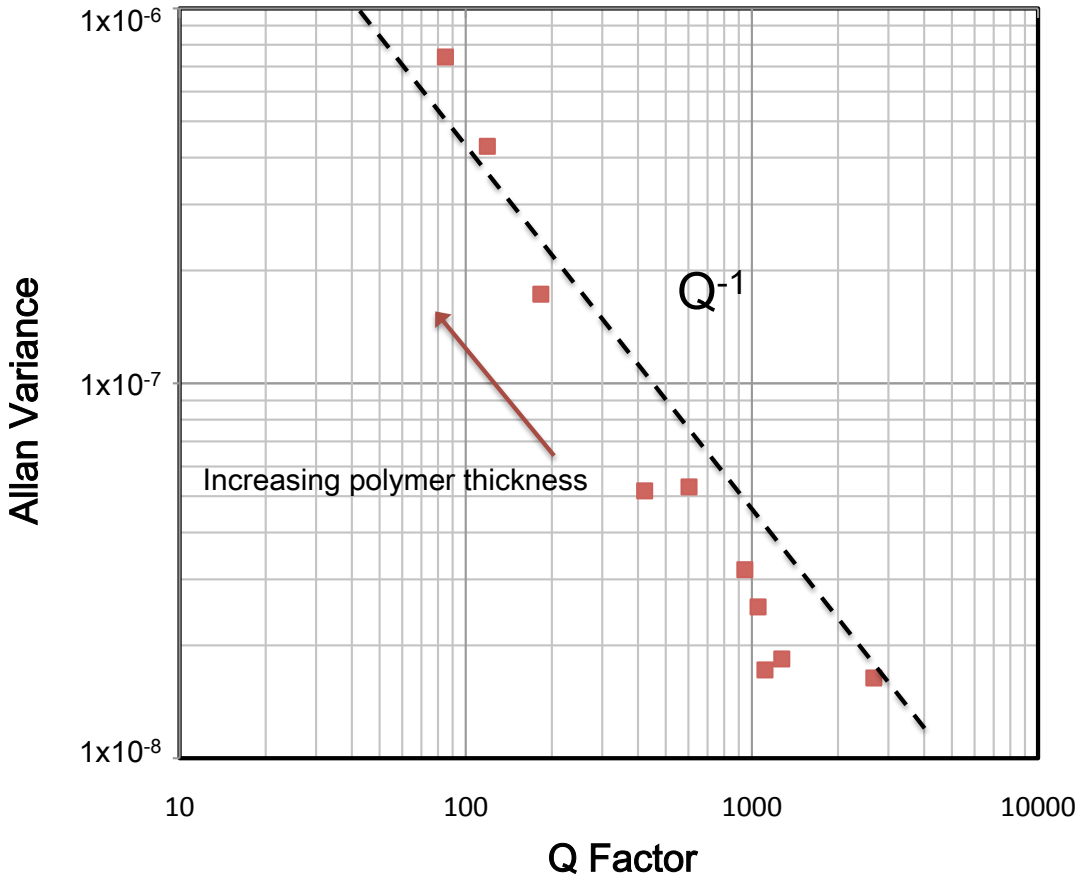

Figure 37: Allan variance as a function of Q-factor for a 7μm resonator with different PIB film thicknesses. The dashed line shows a $\frac{1}{Q}$ trend.

Although the relationship between Q-factor and Allan variance can be expected from theory, the relationship between Allan variance and polymer thickness is of more interest for determining the LOD of the disk resonators as a function of polymer thickness. The relationship between Allan variance and normalized polymer (PIB) thickness for the disk resonators with 7 μm and 18 μm silicon thickness is plotted in the log-linear plot of Figure 39.

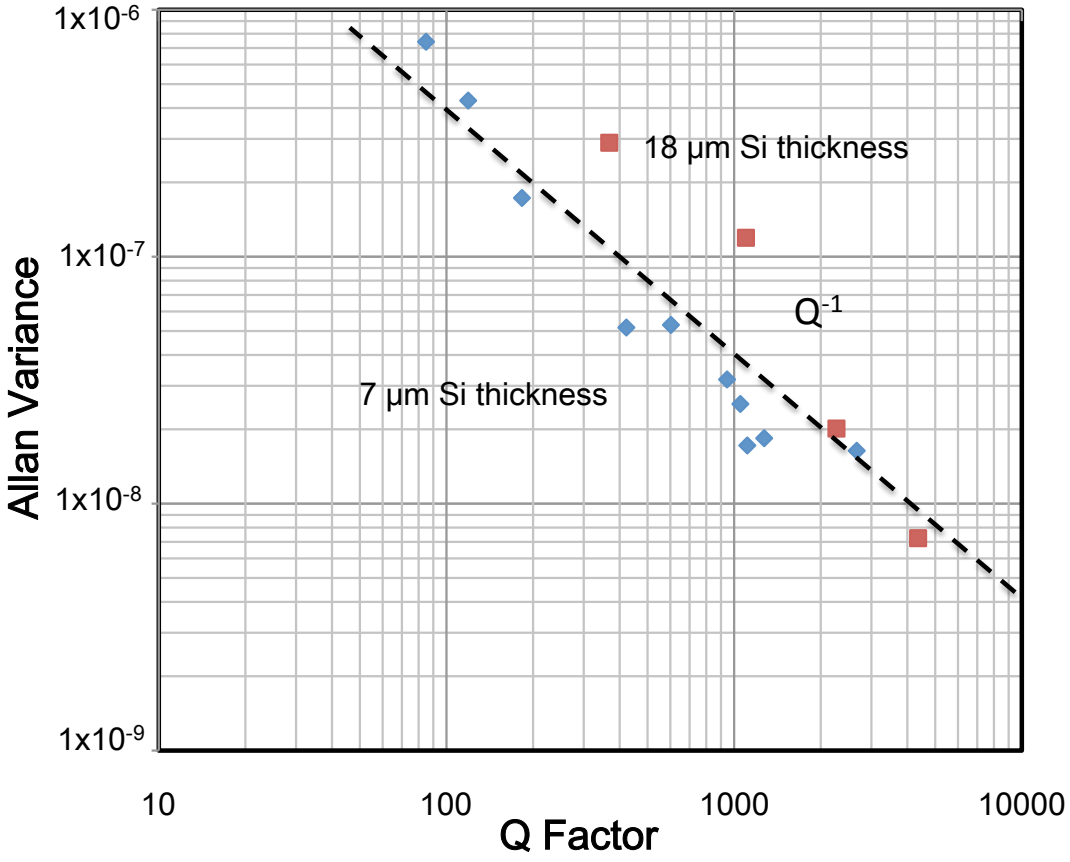

Figure 38: Allan variance as a function of Q-factor for resonators with different polymer (PIB) film thicknesses. Data from resonators with $t_{Si} = 7\mu m$ (blue diamonds) and $t_{Si} = 18\mu m$ (red squares) are shown. The dashed line shows a $\frac{1}{Q}$ trend.

The relationship of Allan variance to normalized polymer thickness is shown to be exponential in nature. The Allan variance of the resonator can now be described by the following equation

$$Var_{Allan}\left(\frac{t_{poly}}{t_{Si}}\right) = Var_o e^{\alpha\left(\frac{t_{poly}}{t_{Si}}\right)}, \tag{61}$$

where Var_o is the initial Allan variance of the uncoated resonator and α is a unitless fitting factor derived from empirical observations with values ranging from 2-11 for resonators with 7 μm to 18 μm silicon thicknesses, respectively. The fitting factor α is found to increase with the resonator silicon thickness t_{Si}.

Given that α is proportional to t_{Si}, the Allan variance expression of (61) can be modified such that it only becomes a function of t_{poly}

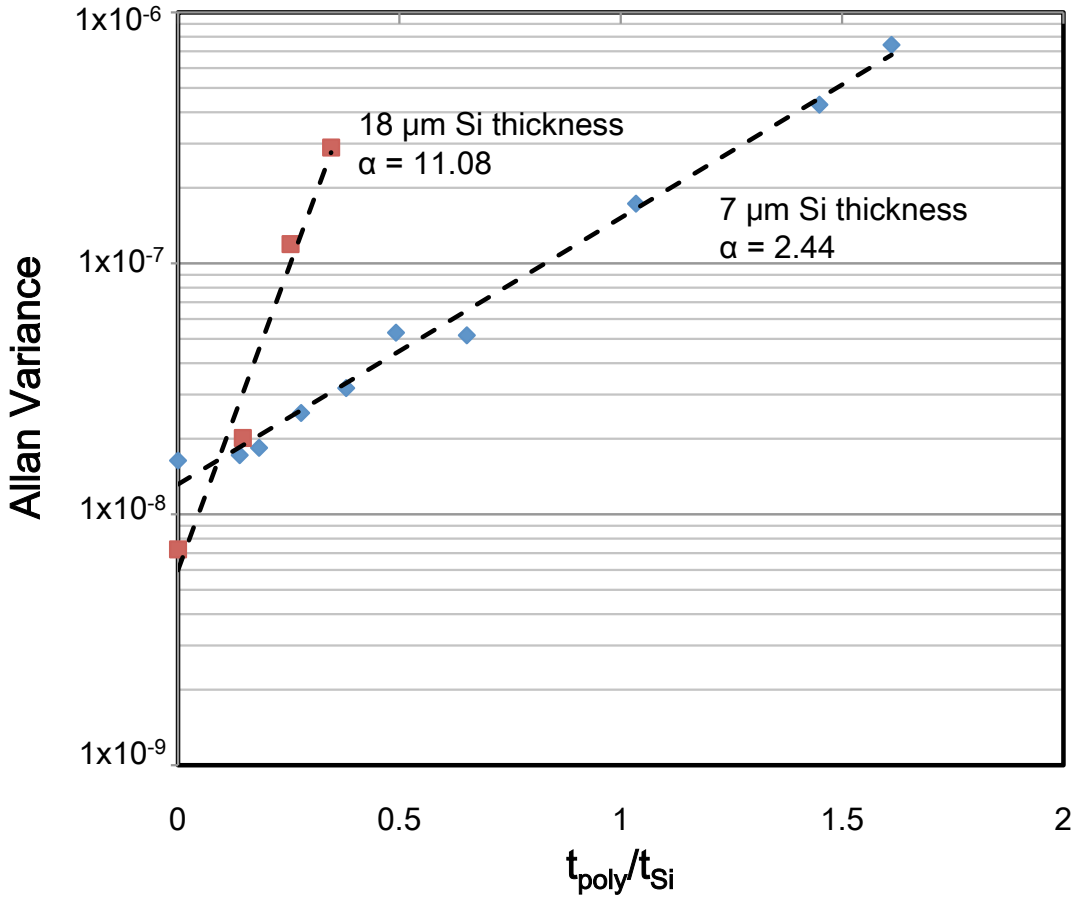

Figure 39: Allan variance as a function of normalized polymer (PIB) film thickness. Data from resonators with $t_{Si} = 7\mu m$ (blue diamonds) and $t_{Si} = 18\mu m$ (red squares) are shown.

$$Var_{Allan}\left(t_{poly}\right) = Var_o e^{\beta\left(t_{poly}\right)}, \tag{62}$$

In (62), the Allan variance is now fitted to polymer thickness t_{poly} instead of the normalized polymer thickness $\frac{t_{poly}}{t_{Si}}$. Applying this new equation to the data, the fitting parameter β adopts values of $3.5 \times 10^{-1}/\mu$m and $6.1 \times 10^{-1}/\mu$m for the 7 μm and 18 μm cases, respectively. This much tighter variance of fitting parameter values between the two resonator silicon thicknesses suggests that t_{poly} should be the sole variable considered for modeling the Allan variance, as in (62), and that the Allan variance dependence is better expressed in terms of polymer thickness alone. The regression of Allan variance against polymer thickness alone is shown in Figure 40.

From the exponential dependence of Allan variance on normalized polymer thickness

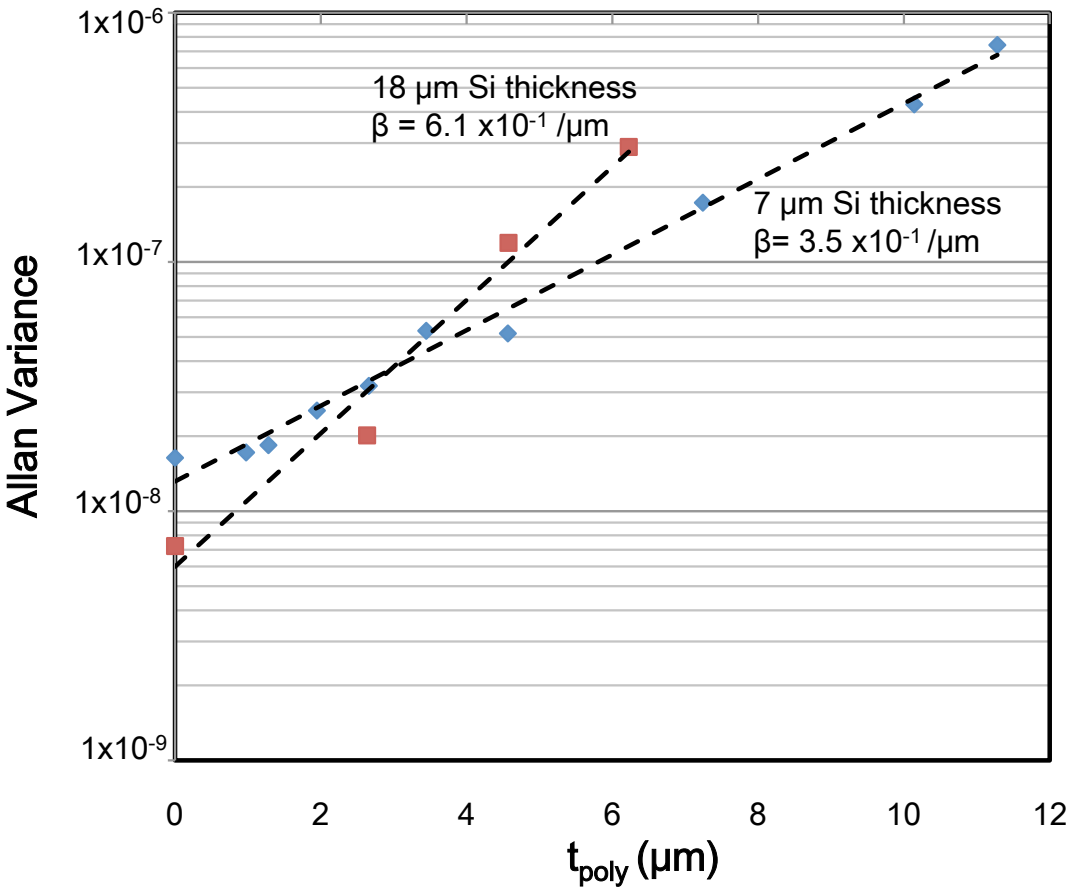

Figure 40: Allan variance as a function of polymer (PIB) film thickness. Data from resonators with $t_{Si} = 7\mu m$ (blue diamonds) and $t_{Si} = 18\mu m$ (red squares) are shown.

shown in Figure 39, the definition of LOD shown in (60) becomes a ratio of an exponential function of normalized polymer thickness to a linear function of normalized polymer thickness. Therefore the polymer will have an optimal thickness to minimize LOD. Combining equations (58),(60), and (61) produces an analytical model which closely matches the experimentally measured LODs for toluene. Figure 41 compares the model with the experimental toluene LODs for resonators of 7 μm and 18 μm silicon thicknesses. The model for LOD in Figure 41 has been adjusted to account for polymer heating as in Figure 34 and Figure 36 by using the heating-corrected partition coefficient K.

For toluene, the minimum limit of detection was 1.2 ppm for resonators of either silicon thickness. Approximately 2.6 μm of coated PIB achieved this limit on a 7 μm thick

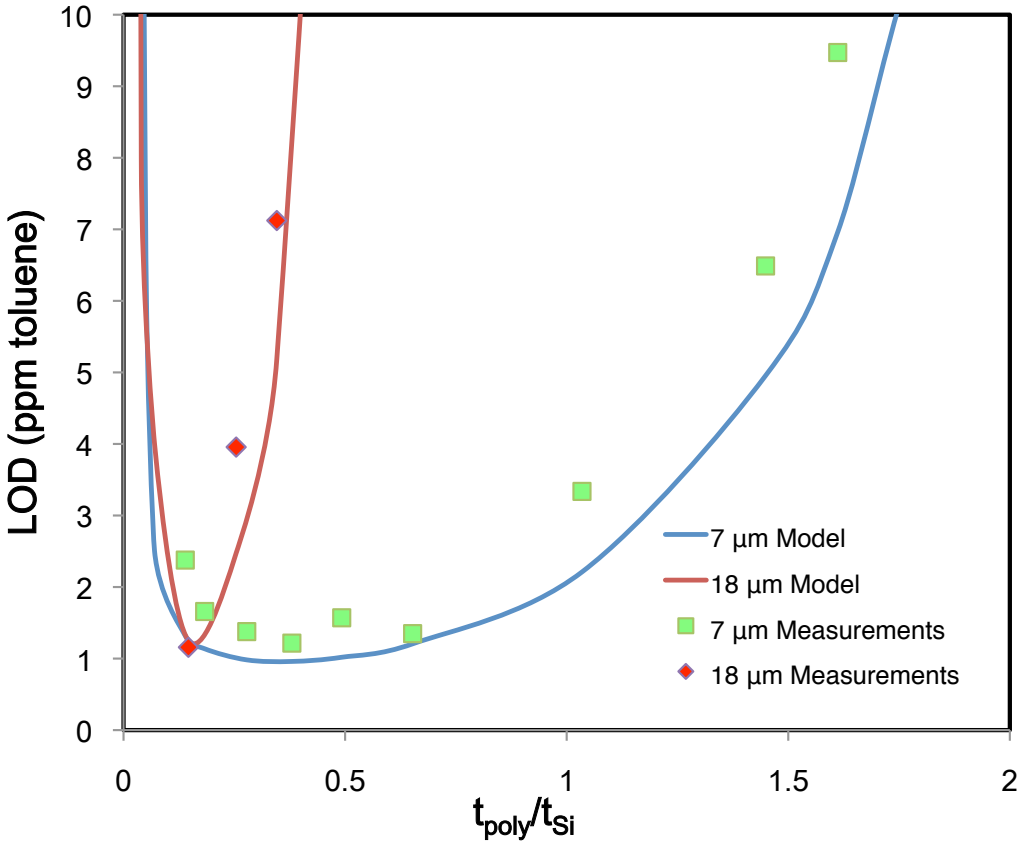

Figure 41: Model of LOD for toluene ($t_{Si} = 7\mu$m blue line, $t_{Si} = 18\mu$m red line) and LODs for toluene extrapolated from measured data ($t_{Si} = 7\mu$m squares, $t_{Si} = 18\mu$m diamonds) as functions of normalized polymer thickness. The minimum limit of detection was 1.2 ppm for both resonators.

resonator, corresponding to a normalized polymer thickness of 0.37. For the 18 μm thick resonator, the normalized polymer thickness that optimized LOD was 0.14, corresponding to the same PIB thickness of 2.6 μm. This invariance of the optimal polymer thickness across different resonator silicon thicknesses suggests that a polymer-thickness-limited process controls the minimal LOD of the sensor system.

4.5.3 Calibration Curves

A series of gas-phase calibration curves were measured for the VOCs benzene, toluene, and m-xylene. These calibration curves were measured on the 7 μm silicon thickness disk resonator with a PIB thickness of 4.5 μm, corresponding to a normalized polymer thickness

of 0.625. From the data shown in Figure 41, this polymer thickness is still within the region of minimum LOD for toluene. Due to the strong exponential relationship of Allan variance on polymer thickness, this same optimal region for limit of detection can be expected when applied to other analytes. The LOD expression of (60) can be modified to correct for the use of different analytes, as only the chemical sensitivity will change due to the different analyte-specific partition coefficients. Figure 42 shows the calibration curves for benzene, toluene and m-xylene vapors.

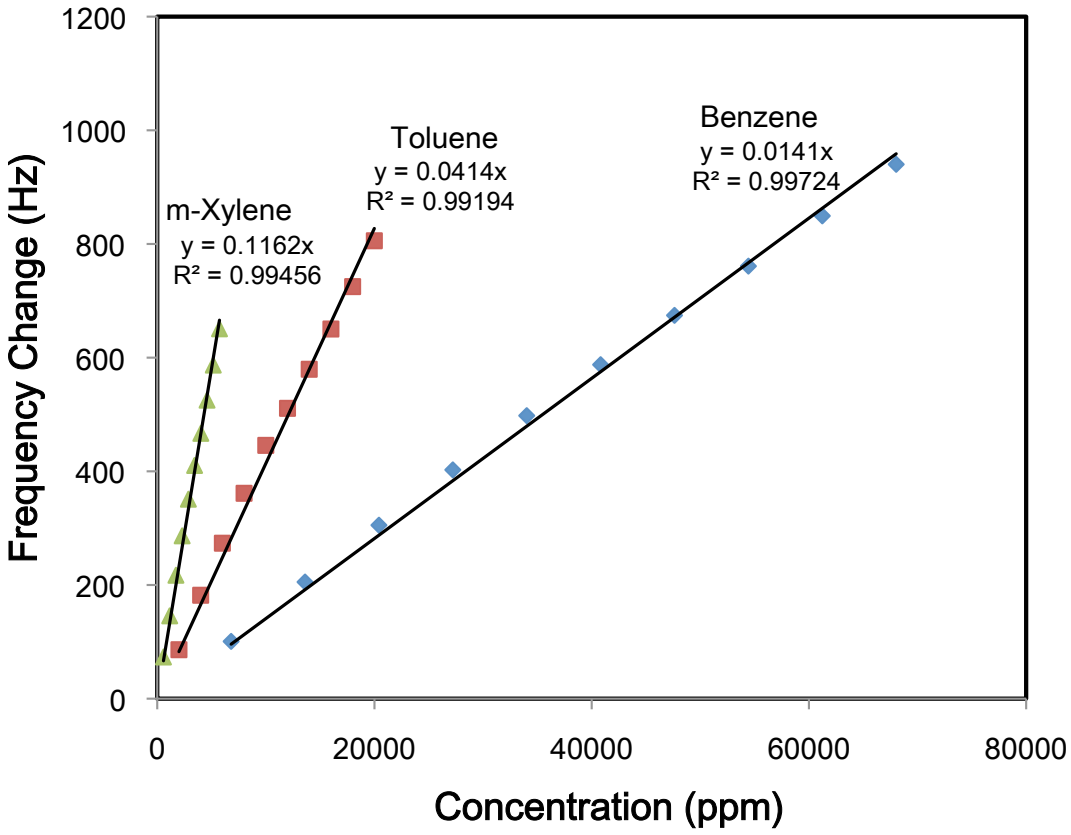

Figure 42: Gas-phase calibration curves for benzene (diamonds), toluene (squares), and m-xylene (triangles). The disk resonator used had a 7 μm silicon thickness and a 4.5 μm PIB thickness.

If one accounts for the polymer heating, the calibration curves agree well with published data for the PIB partition coefficients for benzene, toluene, and m-xylene. In particular, the ratios of the chemical sensitivities for m-xylene, toluene, and benzene of 0.116, 0.0414, and 0.0141 Hz/ppm, respectively, agree with ratios of published partition coefficients for PIB of

m-xylene, toluene, and benzene, respectively. Assuming a PIB-toluene gas phase partition coefficient of 1030 [103], this analysis yields a PIB-m-xylene partition coefficient of 2560, and a PIB-benzene partition coefficient 334. These values agree well with the published data (see Table 9).

Additionally, the model of (60) predicts values in agreement with the measured LODs of the three analytes. This data, along with published and heat-adjusted partition coefficients for each analyte, are summarized in Table 9.

Table 9: LODs and partition coefficients for benzene, toluene, and m-xylene for a PIB-coated ($t_{poly} = 4.5\mu$m) disk resonator ($t_{Si} = 7\mu$m)

Analyte	Measured LOD	Predicted LOD	Published K	Heat-Adjusted K
Benzene	5.3 ppm	4.0 ppm	360 [103]	108
Toluene	1.2 ppm	1.0 ppm	1030 [103]	300
m-Xylene	0.6 ppm	0.5 ppm	2137 [107]	642

From the data presented in Table 9, it becomes clear that the heat dissipation caused by the integrated resistive elements causes a significant decrease in the sensitivity of the coated resonator structure, thus affecting the LOD. The results of Figure 34 indicate that the LOD could be reduced by 3-4 times by reducing the heating power. However, the results shown in Table 10 indicate that reductions in heating power can have an adverse effect on the Allan variance of the oscillator system. Different bias voltages were applied to the excitation resistors to yield changes in sensitivity (and hence LOD) by changing the amount of static heat dissipation on the disk resonator with 7 μm silicon thickness. Table 10 shows results for three different excitation biases used for detection of m-xylene at a PIB thickness of 4.5 μm. The Wheatstone bridge bias voltage V_{cc} was maintained at 2 V and the AC excitation amplitude V_{ac} was held at 0.5 V.

Increases in the excitation bias result in an increase in the amplitude of the resonator's oscillation, which consequently reduces the frequency noise of the system. This accounts for the improvement in Allan variance with increased excitation bias. This improved Allan variance would improve LOD if taken in isolation. However, the increase in excitation bias also precipitates an increase in static heating power dissipation on the resonator surface,

Table 10: Different LODs for m-xylene corresponding to different excitation biases (PIB thickness 4.5 μm)

Excitation Bias (V)	Static Heating Power (mW)	Allan Variance	m-Xylene LOD
0.5	9.2	$1.51\text{x}10^{-7}$	0.94 ppm
1.0	11.6	$6.83\text{x}10^{-8}$	0.59 ppm
1.5	15.6	$5.07\text{x}10^{-8}$	0.73 ppm

thus leading to a decrease in sensitivity, and thus serving to worsen LOD for the higher excitation biases. Due to the inverse dependence between excitation bias and Allan variance, a static heating power of 11.6 mW was found to minimize the LOD for the 7 μm thick disk resonator, as shown in Table 10. The conditions corresponding to this optimal case were used for all the measurement results presented in the previous sections of this chapter. The tradeoff between low heat dissipation and low frequency noise could be made less severe through improved thermal design of the resonator structures.

4.5.4 Transient Behavior

The diffusion process that drives the analyte into the polymer sensing layer can be expected to produce equilibration characteristics typical of Fickian diffusion. The amount of time needed to reach the maximal analyte-induced sensor response can be characterized by a time constant τ. τ represents the amount of time needed for the sensor to reach 66% of its maximal response for a given concentration. For thicker polymer layers this time constant can be expected to increase.

Figure 43 shows a collection of transient responses for the PIB-coated disk resonator with 7 μm silicon thickness upon exposure to 4000 ppm of toluene for different polymer thicknesses ranging from 0.97 μm to 11.3 μm.. The chemical sensitivity increases with increasing polymer thickness, as modeled by (59). The associated time constant for each analyte-induced sensor response is also seen to increase. Figure 44 shows that this increase is roughly linear with polymer thickness and ranges from 1 to 20 s. In the polymer thickness range corresponding to minimal toluene LOD, the time constant is under 10 s.

The results show that the sensor system should be able to resolve transient changes in

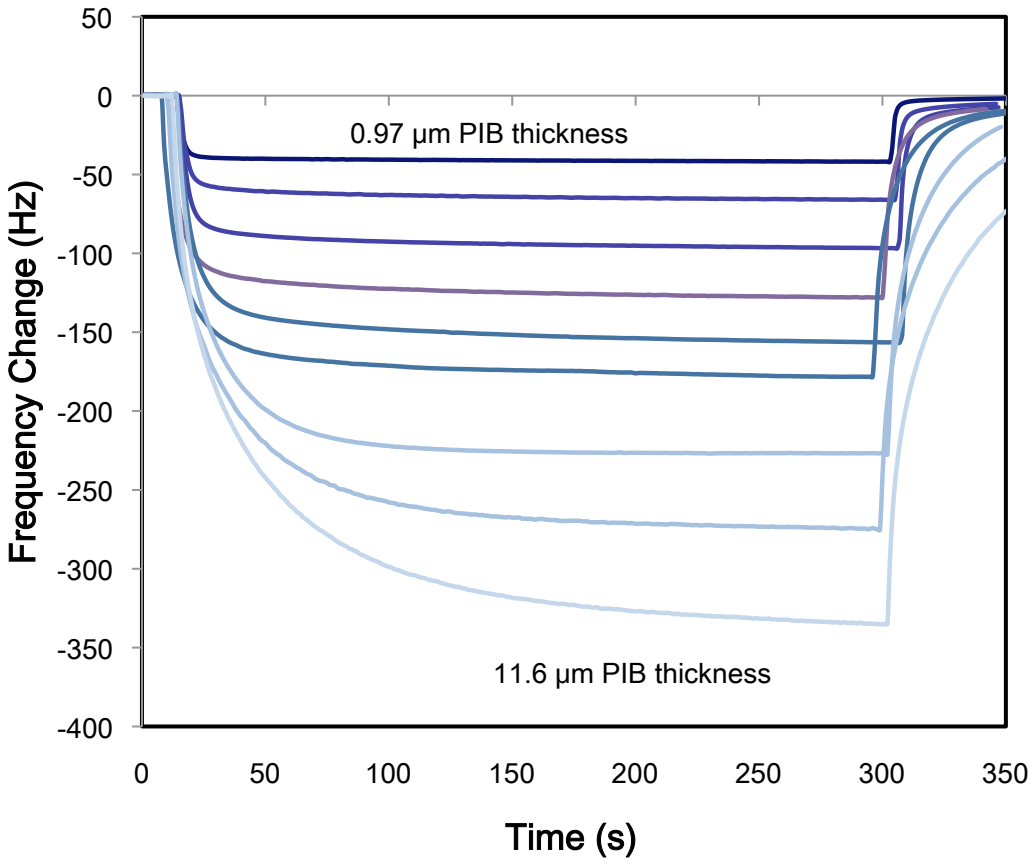

Figure 43: Transient responses of the PIB-coated disk resonator with 7 μm silicon thickness upon exposure to 4000 ppm of toluene for different polymer thicknesses.

analyte concentration on the order of seconds. Since the initial slope of the sensor response is steep, these sensors should be suitable for pre-concentrator-based sensor systems in which analyte concentrations are boosted and exposed to the sensors very quickly.

The transient response can be analyzed further through the theory of Fickian diffusion. Given a polymer of thickness t_{poly}, the ratio of mass sorption at time t to equilibrium mass sorption can be approximated by the following equation [113]

$$\frac{M_t}{M_\infty} = \frac{4}{t_{poly}} \left(\frac{D}{\pi}\right)^{\frac{1}{2}} \sqrt{t}, \tag{63}$$

where M_t is the mass uptake at time t, M_∞ is the equilibrium mass uptake, and D is the diffusion coefficient. The above relationship is valid during the initial phase of analyte sorption into the polymer. It follows that a linear relationship should exist between $\sqrt{t}$ and

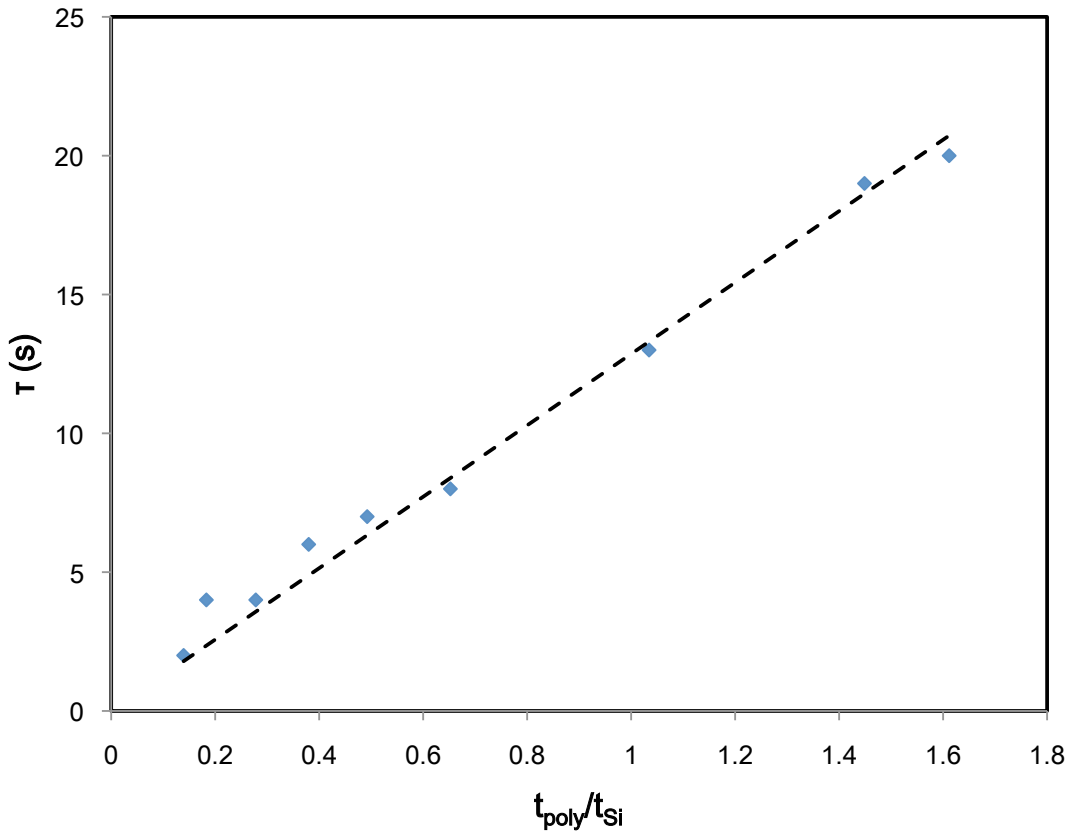

Figure 44: Time constant τ to reach 66% of the maximal sensor response from a 4000 ppm toluene exposure as a function of normalized polymer (PIB) thickness for a disk resonator with 7 μm silicon thickness.

$\frac{M_t}{M_\infty}$. This relationship should hold for small t.

Using the ratio of frequency change over maximum frequency change $\frac{\Delta f}{\Delta f_{max}}$ as a proxy for $\frac{M_t}{M_\infty}$, Figure 45 plots $\frac{\Delta f}{\Delta f_{max}}$ vs $\sqrt{t}$ for 4000 ppm injections of toluene for PIB thicknesses of 0.97 μm and 11.6 μm on the disk resonator with 7 μm silicon thickness.

The initial linearity of the relationship for small t is evident in the curve corresponding to the 0.97 μm thickness. For the curve corresponding to the 11.6 μm thickness, the linear region has a shallower slope, in keeping with the $\frac{1}{t_{poly}}$ relationship in (63). However, for a given time t, $\frac{\Delta f}{\Delta f_{max}}$ for the 11.6 μm polymer thickness is not 11 times smaller, as expected from (63). This suggests that a diffusion-limiting phenomena might be occurring.

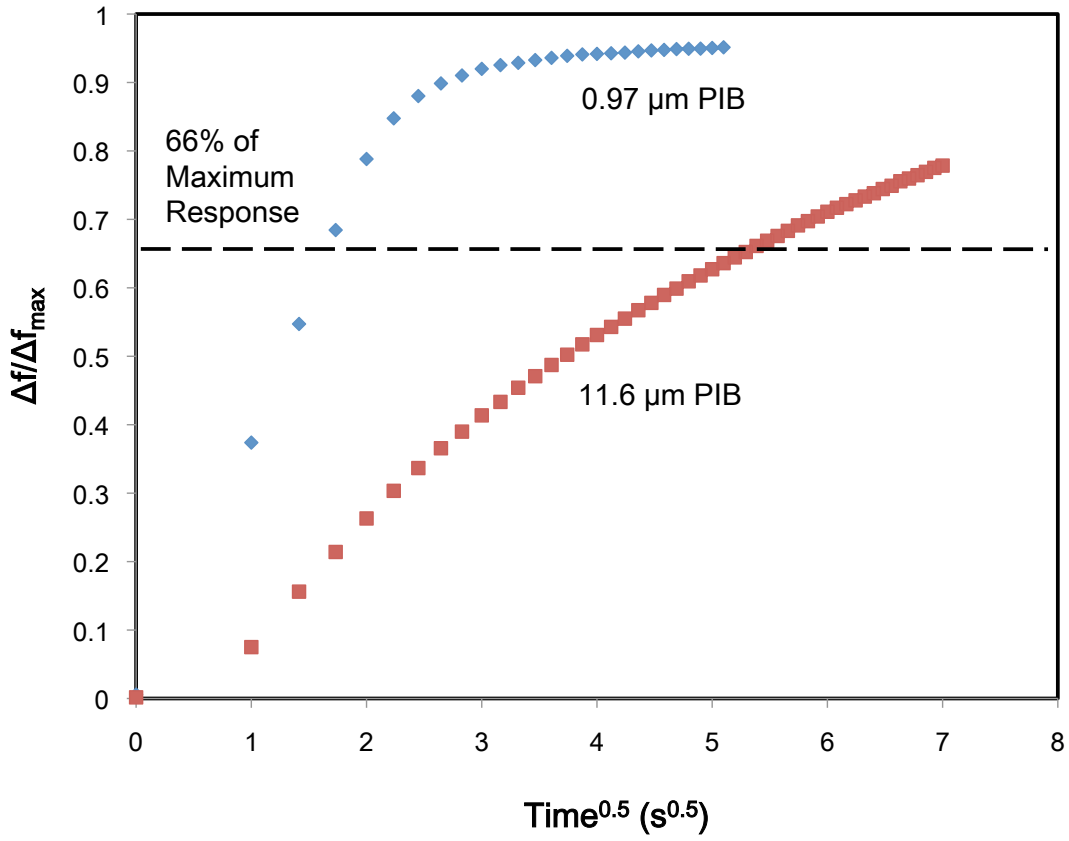

Figure 45: $\frac{\Delta f}{\Delta f_{max}}$ vs $\sqrt{t}$ for a 4000 ppm injection of toluene on a PIB-coated disk resonator with 7 μm silicon thickness for PIB thicknesses of 0.97 μm (blue diamonds) and 11.6 μm (red squares).

4.5.5 Polymer Uniformity

For the chemical sensing experiments, the thickness of the deposited polymer on the disk resonators was measured using conventional mechanical profilometry. Reference samples were spray-coated with the polymer solution for the same amount of time as the actual experimental devices. This was done to obtain polymer thicknesses on the reference samples that were equivalent to those on the experimental devices. The reference samples were then measured using a mechanical profilometer. Optical profilometry, which does not use mechanical contact with the sample, can be used to investigate the properties of the polymer films that were applied to the disk resonators without disturbing them.

Figure 46 shows an optical profilometry measurement of a disk resonator coated with

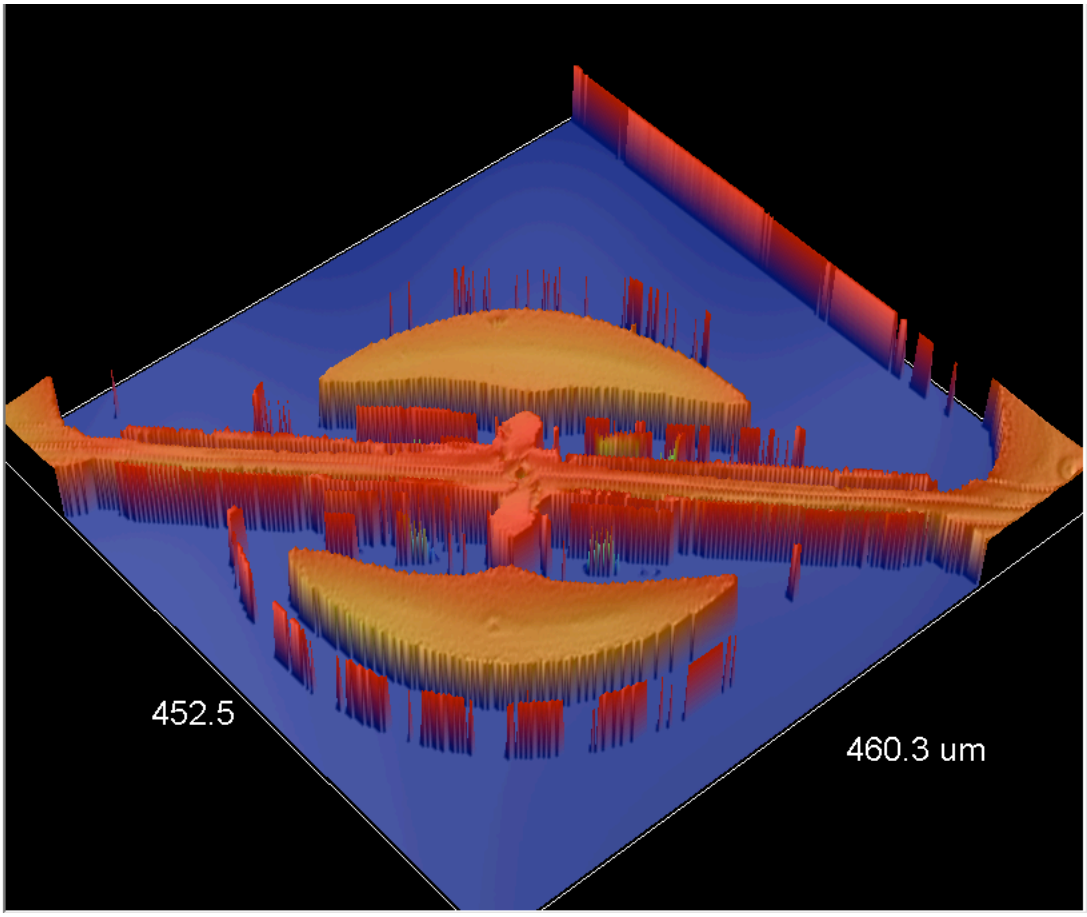

Figure 46: Optical profilometry measurement of a disk resonator with 9.7 μm of deposited PIB. Disk dimensions are $r_o = 170\mu$m and $t_{Si} = 18\mu$m. Areas beyond the measurement range appear as blue and the coated device structure appears as red.

PIB. The disk dimensions are $r_o = 170\mu$m and $t_{Si} = 18\mu$m. The optical profilometer measures an average polymer thickness of 9.7 μm, whereas the reference sample method using mechanical profilometry measures 8 μm. The optical profilometry and mechanical profilometry measurements of the polymer thickness are with 20% of each other. Each method uses an average measurement to account for the lack of uniformity in the polymer layer. In Figure 46, the polymer is shown to concentrate towards the center of the half-disks and central anchor beam. This lack of uniformity can cause deviations in the experimental results from the models derived earlier in this chapter, which assume uniform polymer layers.

4.6 Chapter Summary

This chapter presented chemical sensing results for gas-phase volatile organic compounds (VOCs) using a PIB-coated disk resonator. The general derivation for the chemical sensitivity of a resonant gravimetric sensor with a rotational in-plane resonance mode was presented. This was followed by experimental results in which disk resonators of 7 and 18 μm silicon thicknesses were spray-coated with (poly)isobutylene (PIB) polymer and exposed to controlled concentrations of VOC vapors in a gas manifold system. The limit of detection (LOD), chemical sensitivity, Q-factor, and Allan variance as functions of polymer thickness were presented for both device silicon thicknesses. Calibration curves for benzene, toluene, and m-xylene were presented, along with transient responses from toluene vapor exposures. The results yield the following insights:

- The chemical sensitivity normalized by the resonance frequency is completely independent of lateral geometric parameters for microstructures with a uniform material layer stack vibrating in a rotational in-plane resonance mode. Since the frequency change per unit mass added to the resonator surface increases with resonance frequency, normalizing the chemical sensitivity by the resonance frequency yields an expression that is independent of terms describing the lateral geometry of the resonator.

- With increasing polymer thickness, the coated disk resonators experienced an exponential increase in frequency noise due to the additional damping introduced by the viscoelastic properties of the polymer. This exponential dependence was empirically described with a fitting factor.

- Given the models for chemical sensitivity and frequency noise, a model for LOD was found that predicts an optimal polymer thickness for minimizing LOD. This model was in agreement with experimental results.

- A PIB-coated disk resonator with a 7 μm silicon thickness and disk radius of 170 μm exhibits LODs of 1.2 ppm for toluene, 5.3 ppm for benzene, and 0.6 ppm for m-xylene. The coated PIB thickness corresponding to these LODs was 4.5 μm.

Table 11: Chemical Microsensor Technology Comparison with Disk Microresonators in the VOC Vapor Sensing Role

Method	Analyte	Material Phase	LOD	Source
UV-Visible Spectroscopy	benzene	Gas	3-6 ppb	[27]
Resonant Silicon Disk	**m-xylene**	**Gas**	**600 ppb**	[69]
Voltammetric	benzene	Gas	1 ppm	[48]
Surface Acoustic Wave	n-octane	Gas	2.1 ppm	[36]
Resonant Silicon Cantilever	n-octane	Gas	2.5 ppm	[45]
Quartz-crystal Microbalance	toluene	Gas	12 ppm	[31]
Capacitive	toluene	Gas	61 ppm	[50]
Calorimetric	toluene	Gas	100 ppm	[29]

- The chemical sensitivity is limited by heating of the polymer layer by the integrated resistive elements within the disk resonator. If this heating were mitigated, a 3-5x increase in sensitivity could be achieved, allowing a 3-4x decrease in the aforementioned LODs (accounting for the polymer thickness region corresponding to optimal LODs).

- The transient delay time required to reach the 66% of the sensor response for a given concentration of exposed analyte is a linear function of polymer thickness. The delay time is on the order of seconds for a disk resonator with a 7 μm silicon thickness and coated-PIB thicknesses between 0 and 5 μm.

When compared with the other chemical sensing technologies presented in the introductory chapter, the disk resonators presented in this research exhibit a favorable performance when compared to other chemical microsensor technologies. A comparison with other microscale chemical sensing technologies is presented in Table 11. In Table 11, the comparison is with respect to limits of detection for VOC vapor sensing.

As of this writing, the disk resonators achieve the best performance amongst all resonant gravimetric sensors to the author's knowledge for VOC vapor sensing. With further optimization of the frequency noise and chemical sensitivity, e.g. through the reduction of static heating power, the disk resonators could achieve even lower LODs. The advantages of batch fabrication and easy CMOS-integrability would further make the silicon disk resonators competitive with optical sensors, since optical devices often rely on external

light sources. Thus, with further improvement, disk resonator devices can be competitive with the full range of microscale chemical sensor technologies in the VOC vapor sensing application.

CHAPTER V

THE GRAVIMETRIC-CAPACITIVE MULTISENSOR

5.1 Introduction

In this chapter, a gas-sensing transducer based on both capacitive and resonant gravimetric sensing principles is presented. The basic motivation and principles of the transducer are discussed, followed by a presentation of the fabrication process and physical modeling of the transducer. VOC sensing results will then be presented, followed by recommendations for future work on the transducer.

5.2 Motivation for Multisensors

The combination of two chemical sensing principles onto a single transducer structure can yield multiple advantages. Firstly, the possibility exists for obtaining orthogonal sensor responses. That is, a set of analytes that produces a weak response using one sensing principle might produce a strong response with another, thus allowing an expanded analyte sensing ability if a single transducer uses both sensing principles [22]. Secondly, the combination of two sensing principles on one sensing structure allows a minimization of the system footprint. That is, a sensor system that utilizes two sensing principles in separate transducers can be implemented in a smaller area by using a single hybrid transducer. Multisensor approaches utilizing several transducers on a single chip have been demonstrated in the detection of VOCs [28, 60]. In this research, a multisensor utilizing capacitive and resonant gravimetric sensing principles on a single released structure is presented.

A capacitive sensor detects changes in the dielectric constant of a medium. Due to the large dielectric permittivity of water, micromachined capacitive sensors were at first applied towards the measurement of humidity. Due to their relative ease of fabrication, capacitive sensors were amongst some of the first microfabricated sensors [114–116].

Through the use of a polymer sensing layer, capacitive sensing principles can be applied towards gas-vapor sensing. The analyte in this case is absorbed into the polymer layer

through the same physisorption mechanism described in the previous chapter. In the case of a capacitive sensor, the change in the dielectric permittivity of the polymer layer is detected. This dielectric change can be either positive or negative, depending on the difference between the dielectric permittivities of the polymer layer and the analyte. This is in contrast to the disk resonators of the previous chapter, which sense changes in the density of the polymer layer.

The advantage of a gravimetric-capacitive multisensor becomes apparent by considering the respective advantages of each sensing principle. A transducer using only a gravimetric sensing principle would have difficulty distinguishing between two analytes with similar mass and physisorption properties (i.e. similar partition coefficients). However, if the two analytes have differing dielectric constants, a capacitive transducer could differentiate them.

On the other hand, if the dielectric constants of the analytes are close to that of the polymer sensing layer, no change in dielectric permittivity is detected. The gravimetric transducer, however, would detect the mass-change of the sensing layer in any case. Thus, the advantage of combining the two sensing mechanisms becomes apparent. Additionally, the high humidity sensitivity of capacitive sensors can also be used to compensate for humidity effects. An example would be the use of a humidty-based capacitive signal which is subtracted from the gravimetric sensor signal to remove the humidity effects present in the latter.

In this research, the combination of gravimetric and capacitive sensing principles is explored. For the case of the presented multisensor system, the sensing layer is again polymeric. The following section describes the underlying theory behind capacitive chemical sensors utilizing polymer sensing layers.

5.2.1 Theory of Capacitive Sensing of Chemical Analytes

Capacitive sensors detect changes in the dielectric properties of the material between the capacitor electrodes. The dielectric material in the VOC sensing application is a polymer layer. The VOC analyte undergoes physisorption into the polymer layer, thereby changing its dielectric properties.

The most basic capacitor geometry is that of the parallel-plate capacitor. The analytical expression for the capacitance of this capacitor geometry can be used to estimate the capacitance of more complex capacitor geometries. The expression is

$$C_{parallel} = \frac{\epsilon A}{d}, \tag{64}$$

where ϵ is the dielectric constant of the medium between the capacitive plates, A is the electrode area and d is the distance between the electrodes. The expression neglects the effect of fringing electric fields, as it only considers electric field lines directly in-between the two capacitor electrodes. This basic analytical expression can be adapted to more complex capacitor geometries by adding a fitting factor G

$$G = \frac{C}{C_{parallel}} \tag{65}$$

The exact value of this fitting factor is obtained through numerical simulation using e.g. FEM methods.

From (64), it can be seen that a change in the dielectric properties $\Delta\epsilon$ will yield a corresponding change in the capacitance $\Delta C_{parallel}$. The ratio of the two can be expressed as

$$\frac{\Delta C}{\Delta \epsilon} = G\frac{A}{d}. \tag{66}$$

It hence becomes apparent that either the electrode area A must be maximized or the electrode distance d must be minimized to maximize the capacitance change and, thus, the signal of a capacitive sensor. This is a critical consideration when designing micromachined capacitors. Electrode materials are typically thin-film metals or polysilicon. The ability to maximize the area of electrodes constructed of these materials relies on the ability to deposit thick layers of high-quality thin films or to etch deep trenches anisotropically. The minimization of electrode distance in the case of thin-film metals relies on high-precision photolithography and lift-off processes to prevent shorting of the electrodes.

For capacitive electrodes implemented using a liftoff process, the effective electrode area

A is the film thickness multiplied by the electrode length. For a given electrode distance d, achieving high capacitances with thin-film electrodes implemented using a liftoff process requires either a thick metal film or long electrodes. Liftoff can become difficult with high film thicknesses, and long electrodes require a large sensor footprint. Choosing the correct approach to achieve a large electrode area is therefore subject to optimization.

In order to use a thin-film capacitor as a VOC vapor sensor, the thin-film capacitor structure is coated with a polymer film [110]. Analyte sorption into the polymer layer causes a change in the overall capacitance of the capacitor structure due to two effects: a) a change in capacitance due to swelling of the polymer layer, and b) a change in the bulk dielectric permittivity of the polymer layer. The dominance of either of these two effects is dependent on the thickness of the polymer layer and the degree to which the electric field lines of the capacitor are initially contained in the polymer layer. Figure 47 illustrates this concept for the two effects.

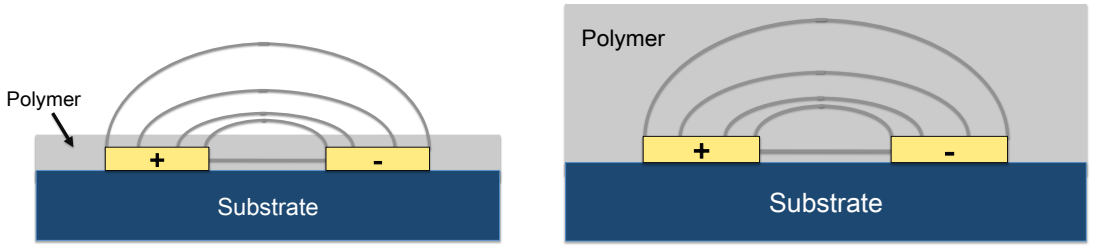

Figure 47: Diagram representing the polymer thickness regimes corresponding to the dominance of either the swelling effect (left) or bulk dielectric effect (right). The dominance of the bulk dielectric effect depends on the degree to which the electric field lines of the capacitor are initially contained in the polymer layer.

The swelling effect is due to the swelling of the polymer layer during analyte sorption. The sorption of analyte into the polymer layer causes a finite volume change of the polymer layer. This results in the electric field lines of the capacitor being subsumed into the polymer layer at the polymer-air interface, producing a capacitance change due to the difference in dielectric constants between the air and polymer. This effect is dominant when the electric field line density at the polymer-air interface is high. This condition corresponds to small polymer layer thicknesses. For large polymer layer thicknesses, the electric field line density

at the polymer-air interface is small, resulting in the capacitance change from swelling effects being reduced.

The bulk dielectric effect is dominant at large polymer thicknesses, and is due to the change of the bulk dielectric properties of the polymer layer during analyte sorption. The diffusion of the analyte into the bulk of the polymer layer causes a change in the overall dielectric permittivity of the polymer layer, thereby affecting a change in the capacitance of the structure.

The following sections will theoretically describe the swelling and bulk dielectric effects.

5.2.1.1 The Swelling Effect

A number of quantities must be defined to fully quantify the contribution of the swelling effect to the capacitance change of the capacitive sensor structure. The percentage of the polymer layer into which the analyte is absorbed is one of the factors that determines the amount of swelling. Thus, it is necessary to define the volume fraction

$$\phi_L^A = \frac{V_{l^*}^A}{V_{l_o}^{tot} + V_{l^*}^A}, \tag{67}$$

where $V_{l^*}^A$ is the volume the absorbed analyte would occupy if it were in the liquid phase, and $V_{l_o}^{tot}$ is the polymer layer volume without any analyte absorbed. In this analysis, liquid properties of the analyte are used when the polymer-analyte mixture is considered. The volume fraction quantifies the fraction of the volume occupied by the analyte in the polymer-analyte mixture after analyte sorption under ideal mixture assumptions. The volume fraction is expressed more directly in terms of the physical properties of the analyte by

$$\phi_L^A = \frac{c_L^A}{\frac{\rho_{l_o}^A}{M^A}}, \tag{68}$$

where M^A is the molar mass of the analyte, $\rho_{l_o}^A$ is the density of the analyte in the liquid phase, and c_L^A is the concentration of the analyte in the polymer layer. The concentration c_L^A is a result of gas-phase physisorption, and allows direct application of the gas-polymer

partition coefficient K for the given analyte. Under the assumptions of the ideal gas law, the final expression for volume fraction becomes [110]

$$\phi_L^A = p^a \frac{K}{RT\frac{\rho_{l_o}^A}{M^A}}, \tag{69}$$

where p^a is the partial pressure of the analyte, R is the ideal gas constant and T is the absolute temperature.

The volume fraction of (69) can now be used to quantify the volume increase of the polymer layer due to swelling. The final analyte-polymer mixture is most easily analyzed by considering the analyte and the polymer as liquids. The mixing of liquids is generally not volume-conserving, i.e. the volume of the final mixture will generally not be the sum of the volumes of the polymer layer and analyte. The volume fraction of (69) becomes useful in expressing the volume increase of the polymer layer in the expression [110]

$$V_L^{tot} = V_{l_o}^{tot}\left(1 + \phi_L^A Q_L^A\right), \tag{70}$$

In (70), V_L^{tot} is the final volume of the polymer layer after analyte sorption and Q_L^A is a swelling factor. The swelling factor Q_L^A quantifies the non-ideality of the polymer-analyte mixing. Under ideal mixing, where the final volume is a simple sum of the initial polymer volume and initial analyte liquid volume, Q_L^A equals 1. Assuming a uniform polymer layer, the change in the polymer thickness δt_p from the swelling effect for a given initial polymer thickness t_p can be stated as

$$\delta t_p = \phi_L^A Q_L^A t_p, \tag{71}$$

The polymer layer thickness change due to swelling effects from (71) can be expected to increase with increasing polymer thickness. The effect of this swelling-induced thickness change on the capacitance of the capacitor structure will, however, decrease with increasing polymer layer thickness. This will be shown in the FEM simulations of the multisensor structure (see Theoretical Capacitive Response).

5.2.1.2 The Overall Capacitance Change due to Analyte Sorption

The bulk dielectric change of the polymer sensing layer is the change in dielectric permittivity of the polymer sensing layer after analyte sorption. Because the bulk dielectric change is influenced by the dielectric constant of the analyte, the capacitive responses due to bulk dielectric changes are more useful for analyte sensing than capacitive responses produced by the swelling effect. The most general expression for the final permittivity of the polymer layer after analyte sorption is [110]

$$\epsilon_L = \epsilon_{L_o} + \phi_L^A \left(\epsilon_A - \epsilon_{L_o}\right), \tag{72}$$

where ϵ_A is the permittivity of the analyte in the liquid phase, ϵ_{L_o} is the permittivity of the polymer layer before analyte sorption, and ϕ_L^A is the volume fraction of (69). As can be seen from (72), the change in the permittivity of the sensing layer can be either positive or negative, depending on the difference between the polymer and analyte dielectric permittivities.

(72) does not consider the swelling of the sensing layer upon analyte sorption. To produce an expression that accounts for both the bulk dielectric change and the swelling effect, two geometry-dependent factors are introduced to account for the two effects

$$\begin{array}{ll} G_A & \text{fitting factor for capacitance change due to swelling} \\ G_V & \text{fitting factor for bulk dielectric changes} \end{array} \tag{73}$$

Both of these fitting factors are primarily a function of the ratio of polymer thickness t_p to electrode distance d (i.e. $\frac{t_p}{d}$). The factor G_A will diminish for $\frac{t_p}{d} >> 1$, as the electric field lines of the capacitor structure will increasingly be contained in the polymer sensing layer as $\frac{t_p}{d}$ increases.

The full analytical expression for the final capacitance change is stated without derivation as [110]

$$\Delta C_L^A = \phi_L^A C_{parallel} \left[G_V \left(1 + \frac{\chi_{l_o}}{3}\right)^2 \left[\frac{\chi_A}{1 + \frac{\chi_A}{3}} - Q_L^A \frac{\chi_{l_o}}{1 + \frac{\chi_{l_o}}{3}} \right] + G_A Q_L^A \chi_{l_o} \right], \tag{74}$$

where $\chi = \epsilon - 1$, with the subscript l_o referring to the polymer layer before analyte sorption, and the A subscript referring to the analyte. The capacitance change should thus be linear with analyte concentration, as the analyte concentration is only present in (74) in the volume fraction term ϕ_L^A (see (69)).

Non-linearities are introduced in the G_A term, which is a product of the average polymer thickness and the electric field density at the polymer-air interface. Thus, for very thin polymer layers ($\frac{t_p}{d} << 1$), the G_A term will be small. G_A will reach a maximal value when the polymer thickness is approximately the electrode distance d before decreasing monotonically with polymer thickness. Thus the swelling effect will tend to introduce non-linearities into the response through the G_A term. G_V will monotonically increase and saturate with polymer thickness.

As a general rule, thinner polymer layers will produce capacitive responses that are strongly influenced by the swelling effect. Thicker polymer layers will see the influence of the swelling effect reduced, with bulk dielectric changes being the dominant effect.

5.3 Multisensor Device

The gravimetric-capacitive multisensor presented in this research consists of a silicon-based resonator structure with capacitive interdigitated gold electrodes patterned on its topside. The resonator structure is a clamped-free cantilever beam with a half-disk structure on its free end. The structure is micromachined from single crystal silicon with a 1 μm layer of dielectrics and a final patterned gold layer on its topside comprising the capacitive component of the sensor. The fabrication process is a modified version of the one presented in Chapter 2. An SEM image of a fabricated multisensor structure is shown in Figure 48.

The cantilever with half-disk structure (a so-called hammerhead structure) is designed with integrated excitation resistors and a piezoresistive Wheatstone bridge towards the fixed end. Like the disk resonators of the previous chapters, the mechanical actuation scheme is electrothermal, and the mechanical sensing scheme is piezoresistive. The excitation resistors are designed to mechanically actuate the fundamental in-plane resonance mode of the structure for gravimetric sensing purposes. A FEM simulation of the in-plane resonance

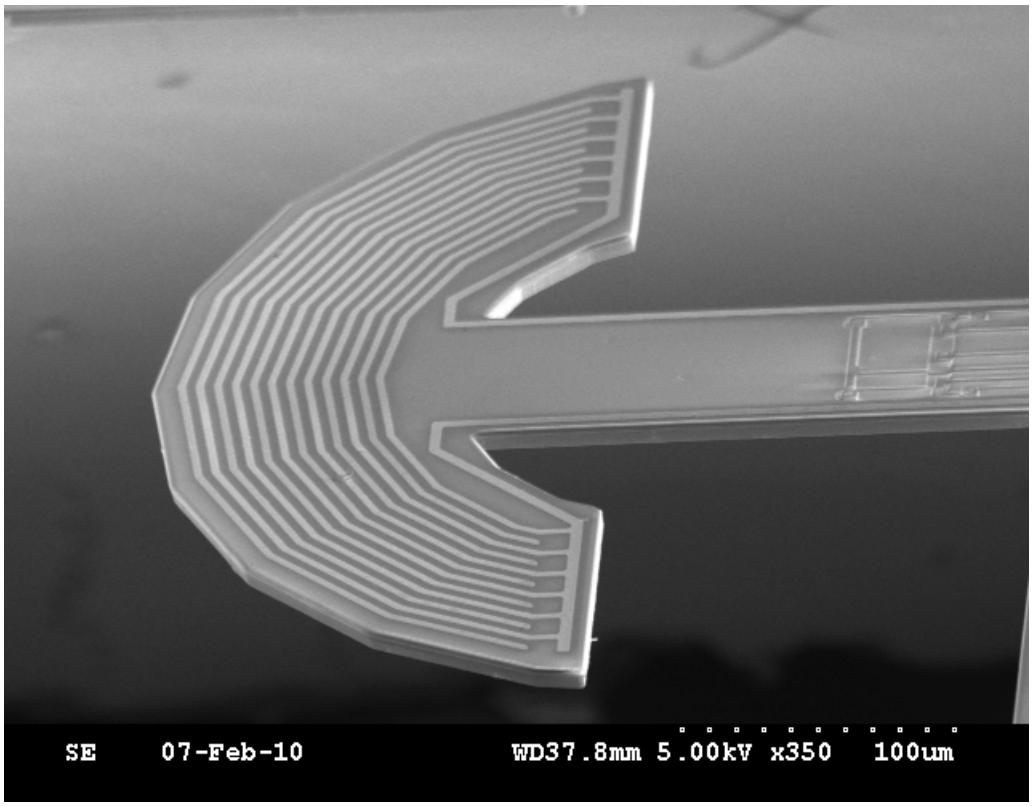

Figure 48: Gravimetric-capacitive multisensor structure. The interdigitated electrodes form the capacitive component of the sensor. The silicon thickness is 7 μm.

mode of the hammerhead structure is shown in Figure 49. The in-plane resonance mode is at a frequency of 475 kHz for the device geometry used in this research. The simulation is done for a pure isotropic silicon structure, without dielectrics and electrode structures.

A diagram of the multisensor structure is given in Figure 50. The values for the geometrical parameters are enumerated in Table 12. The capacitive aspect of the multisensor is formed by gold electrode structures implemented with a liftoff process. An SEM of the electrode structures is shown in Figure 51. The length of a single electrode finger averages 500 μm. There are a total of 12 fingers on the multisensor structure.

For the multisensor devices presented in this chapter, the fabrication process presented in Chapter 2 is modified by adding a photoresist patterning and gold liftoff step. These steps are implemented directly before KOH etching from the wafer backside. The modified

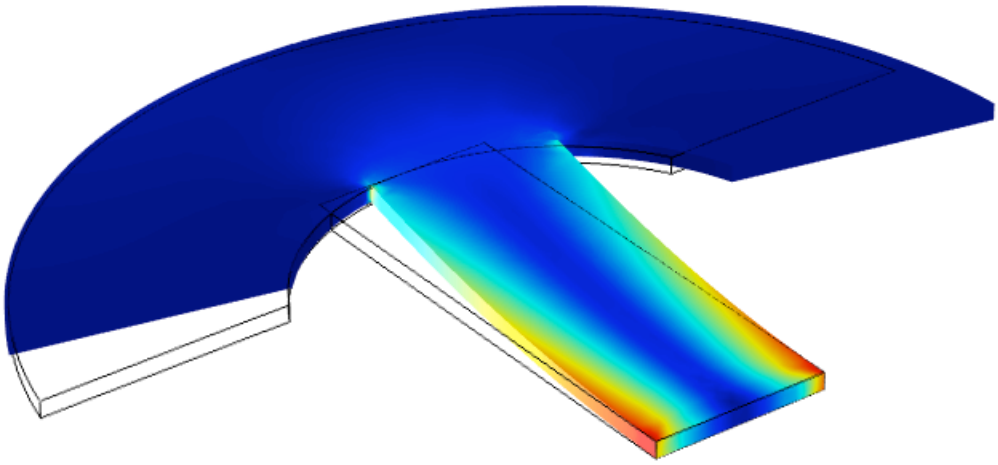

Figure 49: In-plane resonance mode of the multisensor structure. The coloring is of the von Mises stress.

fabrication process is shown in Figure 52. The gold liftoff process is achieved by spin-coating Shipley SC1827 positive tone photoresist onto the wafer at a thickness of roughly 2 μm. After patterning, development, and hard-baking, the photoresist is exposed to oxygen plasma for 15 seconds to remove residues and ensure that the deposited electrodes adhere to the exposed areas of the SiO_2 surface. A 100 $\mathring{A}$ layer of titanium is then evaporated onto the wafer to produce a seed layer for adhesion of the gold to the SiO_2 surface. A 3000 $\mathring{A}$ layer of gold is then evaporated onto the wafer. The wafer is then placed in a sonically excited acetone bath. The acetone dissolves the unexposed resist, lifting off the gold on top of it and leaving the substrate-adhering gold electrode structures behind. The remaining fabrication steps exactly match those of the disk resonator, and are described in Chapter 2.

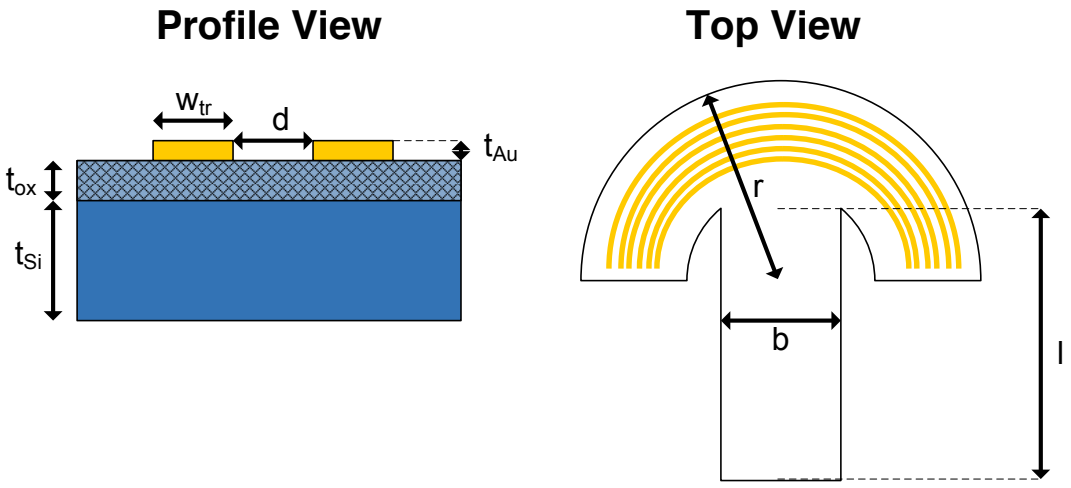

Figure 50: Geometric parameters of the capacitive multisensor.

5.4 Theoretical Capacitive Response

To asses the potential capacitive sensing performance of the multisensor structure, several estimates must be performed. Firstly, an estimate of the baseline capacitance of the sensor structure must be performed. Secondly, estimates of the capacitive change due to analyte sorption must be made.

The baseline capacitance of the sensor structure can be estimated using a 2-D FEM

Table 12: Geometrical Parameters of the Multisensor Device.

Parameter	Description	Value(s)
t_{Si}	Resonator silicon thickness	7 μm
$t_{dielectric}$	PECVD dielectric thickness	1 μm
b	Width of cantilever beam	75 μm
l	Length of cantilever beam	200 μm
r	Radius of half-disk	200 μm
f_{ip}	Resonance frequency of fundamental in-plane mode	475 kHz
d	Electrode spacing	2 μm
w_{tr}	Electrode trace width	2 μm
t_{Au}	Electrode gold thickness	0.3 μm

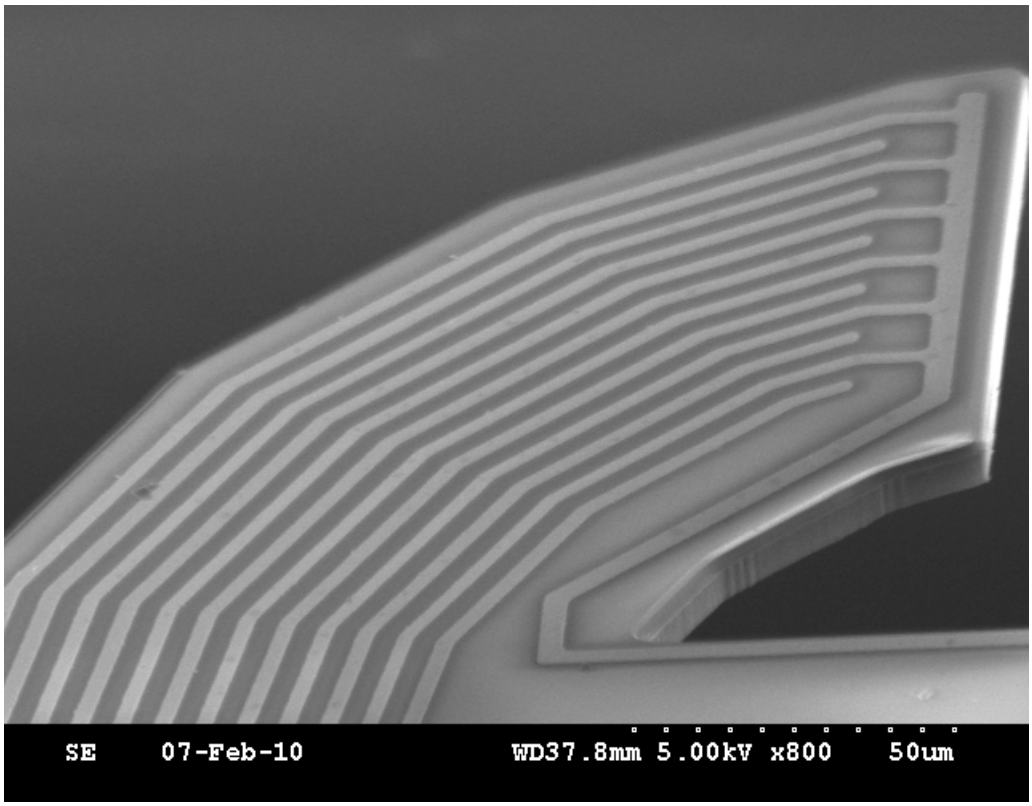

Figure 51: SEM micrograph of the capacitive electrode structure. The gold thickness is 0.3 μm. The electrode width and spacing are 2 μm.

simulation of the electric field between a single pair of gold electrodes. The baseline capacitance estimate is derived from the 2-D FEM model by using the capacitance per unit length of the model and multiplying it by the actual electrode length of the multisensor structure. This calculation does not account for fringing fields at the tips of the electrode fingers.

Figure 53 shows the material stack used in the 2-D FEM simulation of the electric field generated by the multisensor capacitor electrodes. In the simulations, the gold electrode structures are covered by a polymer layer with an additional layer of air above. The combined thickness of the polymer and air layers is 20 μm in the simulations. Below the gold electrodes is a layer of dielectrics, beneath which is the bulk silicon of the resonator structure. All geometric parameters used in the simulation for the electrodes, silicon, and dielectric layers are as in Table 12.

The FEM simulations assumed relative dielectric constants of $\epsilon_{poly} = 2.4$, $\epsilon_{Si} = 11.6$, and

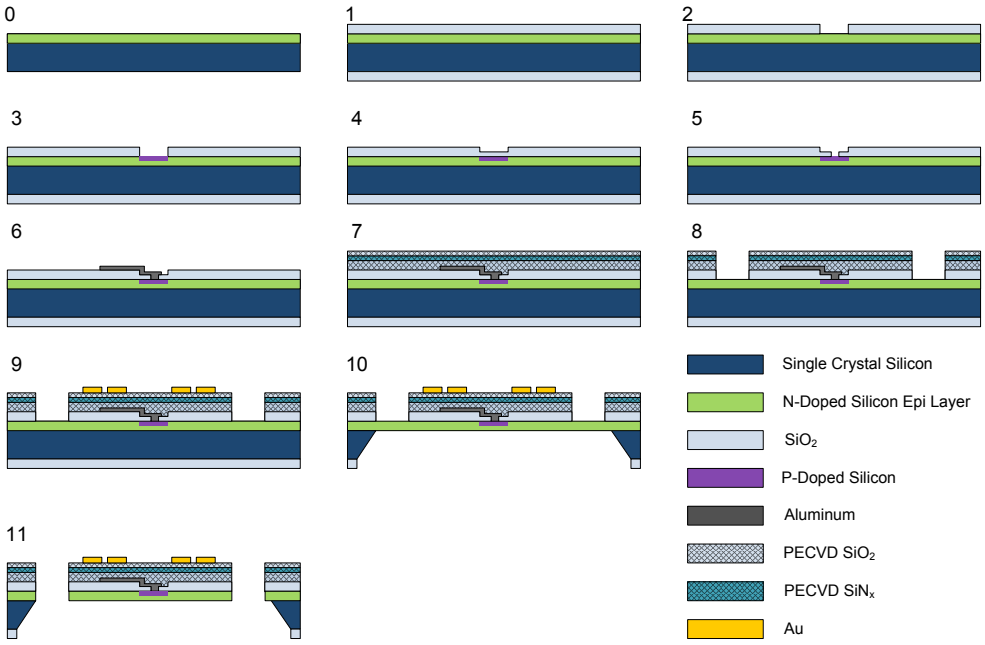

Figure 52: Fabrication process for the multisensor structure. A gold liftoff is performed in step 9.

$\epsilon_{dielectrics} = 3.9$ for the polymer, silicon, and dielectric layers, respectively. The capacitance is obtained by dividing the electrode charge Q by the electric potential applied to the electrodes V (i.e. $C = Q/V$). Figure 54 shows a 2-D FEM simulation of the electric field generated by two gold electrodes on the silicon and dielectric substrate covered by layers of polymer and air.

Figure 55 shows the FEM estimates for the baseline capacitance of the multisensor structure as a function of polymer thickness ($\epsilon_{poly} = 2.4$). The baseline capacitance with no polymer coating is roughly 170 fF for the capacitive electrodes on the multisensor structure.

The baseline capacitance C is a proxy for the G_V parameter, and the derivative of the baseline capacitance as function of polymer thickness ($\frac{dC}{dt_p}$) is a proxy for the G_A parameter of the previous section. The functional dependencies on polymer thickness for baseline capacitance C and its derivative $\frac{dC}{dt_p}$ mirror those of G_V and G_A, respectively [110].

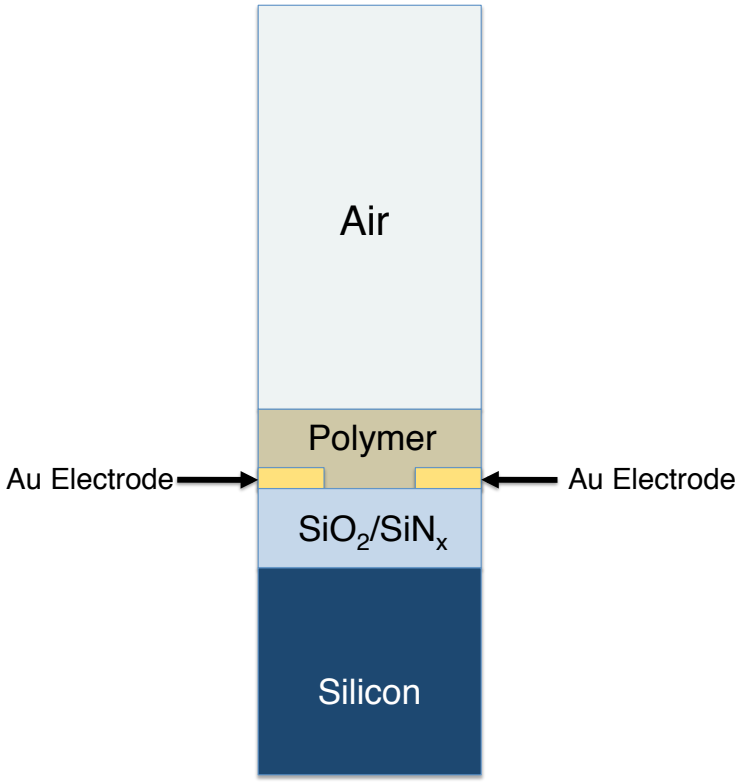

Figure 53: Diagram of the material stack used for the 2-D electric field simulation of the capacitive electrode structures. The layer thicknesses are not shown to scale.

As the polymer thickness increases, the baseline capacitance saturates to its large thickness limit of roughly 230 fF. In this regime, bulk dielectric changes will dominate the capacitive signal. Polymer swelling effects will dominate the output signal where $\frac{dC}{dt_p}$ is large. This corresponds to polymer thicknesses less than the electrode spacing of 2 μm.

Using the simulated baseline capacitance data with (72) and (69), the maximum expected capacitance change for large polymer thicknesses upon exposure to 16000 ppm of toluene vapor is expected to be 0.1 fF for the PIB-coated multisensor structure. This is an estimate for the large polymer thickness limit only, as it considers only bulk dielectric changes.

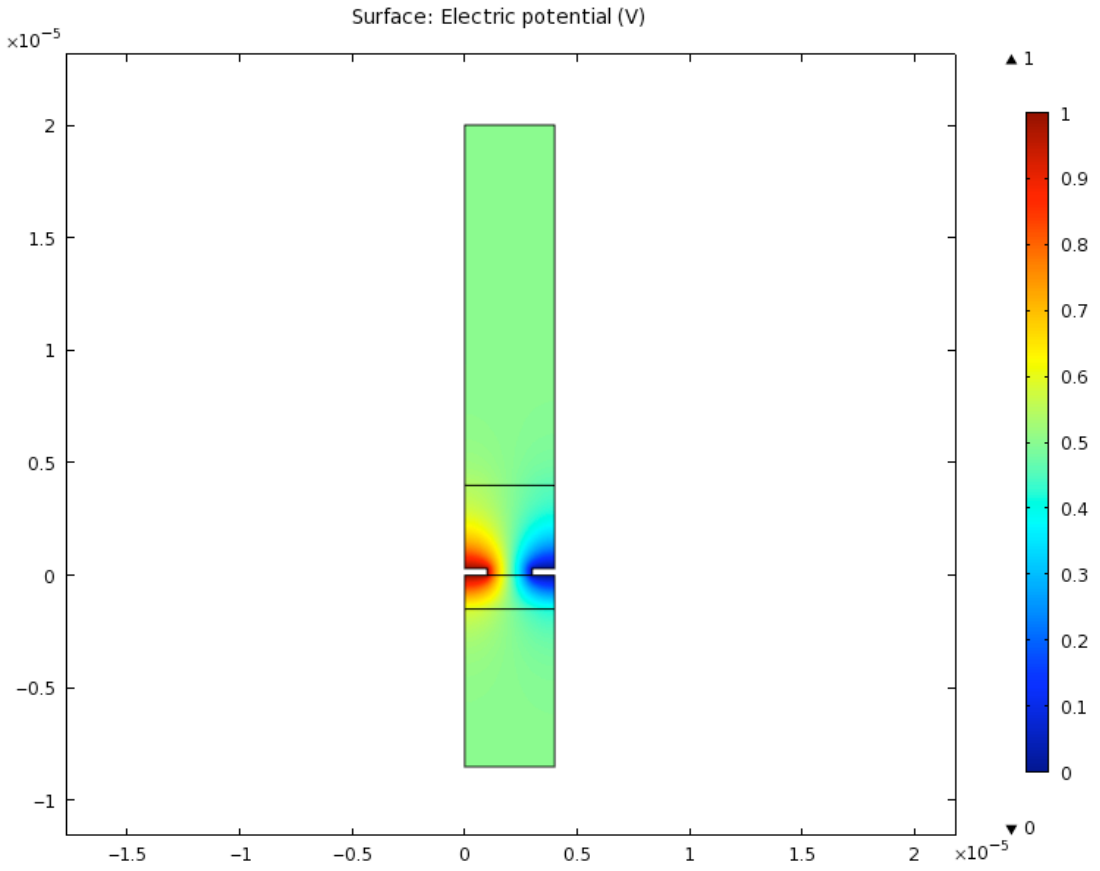

Figure 54: FEM simulation of the capacitance between two finger electrodes on the multisensor structure. The applied potential difference is 1 V, and the simulated polymer thickness is 4 μm.

5.5 Capacitive Readout and Analyte Testing

The procedure for analyte testing of the multisensor device is similar to that described in Chapter 4 for the disk resonators, with the added steps of implementing capacitive readout for the multisensor structure. The die containing the multisensor device is placed in a DIL-28 package. The die is wirebonded to the package with the corresponding pins on the package being connected to a MS3110 evaluation board by Irvine Sensors [117]. The evaluation board contains a capacitive readout IC, which provides a voltage output proportional to the measured capacitance. The noise of the IC output signal is advertised to be $4\frac{aF}{\sqrt{Hz}}$ [117]. The bandwidth of measurement is 500 Hz, giving a noise floor of at least 0.09 fF for the measurements performed in this research. For the experiments performed

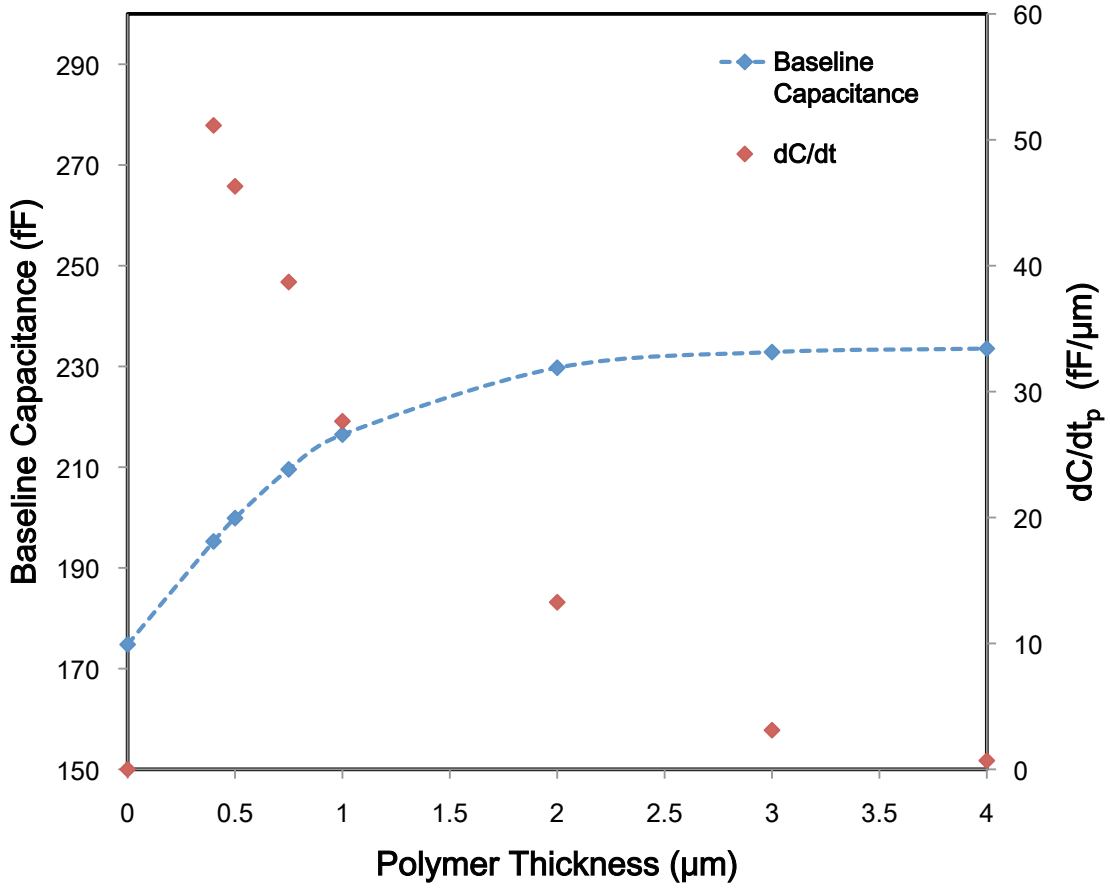

Figure 55: Simulated baseline capacitance as a function of polymer thickness for the multi-sensor structure. The derivative of the baseline capacitance with respect to polymer thickness is also plotted, and indicates the degree to which swelling effects should be dominant in the output signal for a particular polymer thickness.

in this research, a signal gain of 50V/pF is set on the readout board to obtain readable signals for the small capacitance changes measured. This gain is adjusted through the digital calibration interface of the readout IC, which allows adjustment and trimming of the capacitive readout via a parallel port interface. The voltage output of the MS3110 is read by a digital multimeter. The measurement data is then read from the multimeter via a GPIB interface and LabView software.

For analyte testing, the package is placed in the custom gas manifold system described in Chapter 4. The die is spray-coated with a polymer sensitive layer. The polymer used

is (poly)isobutylene (PIB, Sigma-Aldrich) dissolved in a 0.01% w/v solution with toluene. After each polymer coating step, an analyte test is conducted to measure the analyte response at the new polymer thickness. The thickness of the polymer is determined through mechanical profilometry performed on a reference sample. The analytes exposed to the sensor are gaseous toluene and ethanol.

For the experiments conducted in this research, only the capacitive structure is tested to verify the capacitive sensing functionality. Given the large voltages needed to actuate the gas manifold system, electric fields are often created by the metal tubing of the gas manifold system. To avoid this, the experimental setup and sensor is extensively grounded.

5.6 Analyte Response

The capacitive structures were tested without resonating the gravimetric component of the sensor structure. The uncoated capacitance of the capacitive structure was measured to be 550 fF. This measured capacitance value is large compared to that of the calculated value for the capacitive sensor structure ($\approx$ 170 fF). The additional measured capacitance is attributed to the bond wires, bond pads, and wide gold traces connecting the capacitive sensor structure to the bond pads.

The capacitor structure was exposed to several concentrations of ethanol and toluene vapor using the custom gas-manifold system. Figure 56 shows the transient responses to several concentrations of toluene for the capacitive structure when coated with 2.15 μm of PIB. Figure 57 shows the response of the same capacitive structure upon exposure to various concentrations of ethanol vapor. In Figure 57, the PIB thickness is again 2.15 μm.

The responses of the capacitive structure show a non-linear dependence on concentration (see calibration curves in Figure 58). If solely a dielectric change in the bulk were responsible for the response, one would expect a definite linear relationship due to the linearity of the physisorption process with respect to concentration. This linear process produced the linear responses of the gravimetric disk resonator in the previous chapter.

The non-linearity of the sensor response is not fully understood, but could be attributed to the swelling effect at higher concentrations. Due to this non-linearity, the analysis of

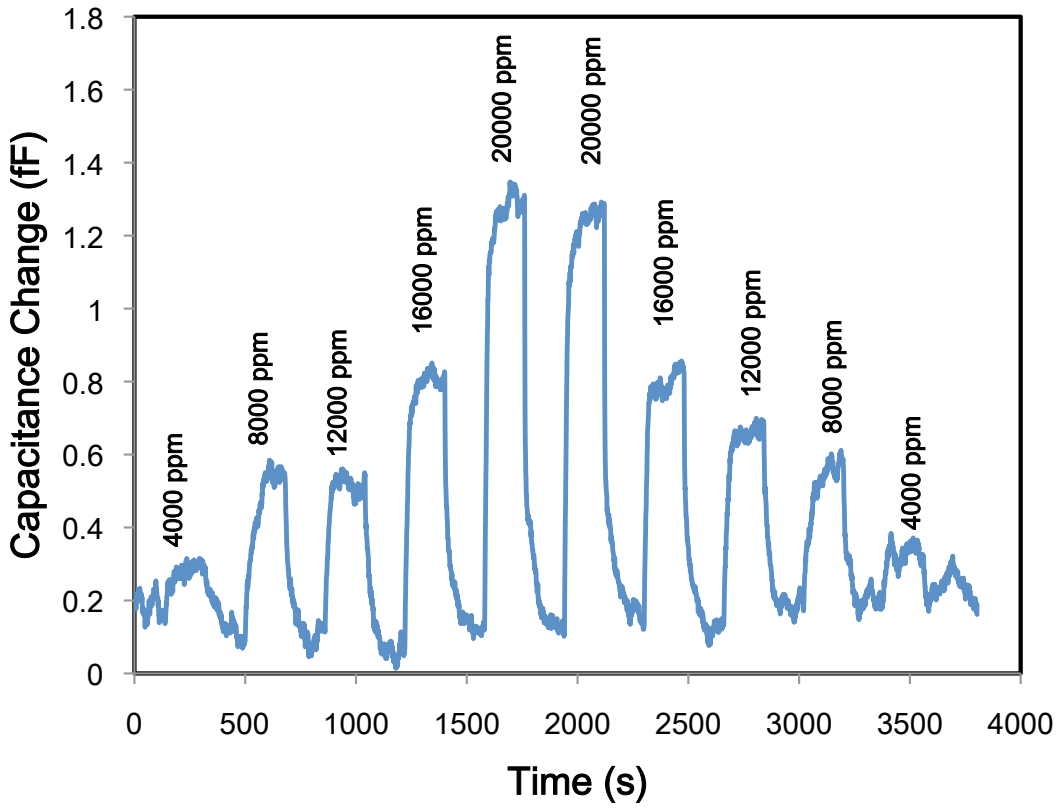

Figure 56: Measured capacitance change of the capacitive structure when exposed to several concentrations of toluene vapor. The PIB thickness is 2.15 μm.

the chemical sensitivity must be performed at a fixed concentration of analyte. To analyze the sensitivity of the structure across polymer thicknesses, a single concentration must be chosen for comparison. Figure 59 shows the response of the capacitive structure to 16000 ppm of ethanol vapor as a function of PIB thickness and 16000 ppm of toluene vapor as a function of PIB thickness (t_p). The capacitive noise level for each polymer thickness is also shown. The noise is taken from the standard deviation of the baseline capacitive signal without any analyte exposure. The noise floor was measured to be roughly 0.03 fF.

The responses of Figure 59 hint further at the role of the swelling effect in the sensor response. The responses measured at a PIB thickness of 26 μm were below the noise level, and thus could not be plotted with certainty. The capacitive response decreases for both analytes beyond a 2 μm PIB thickness. This is consistent with a response attributable to the swelling effect, as the swelling effect should have a diminishing effect on the capacitive

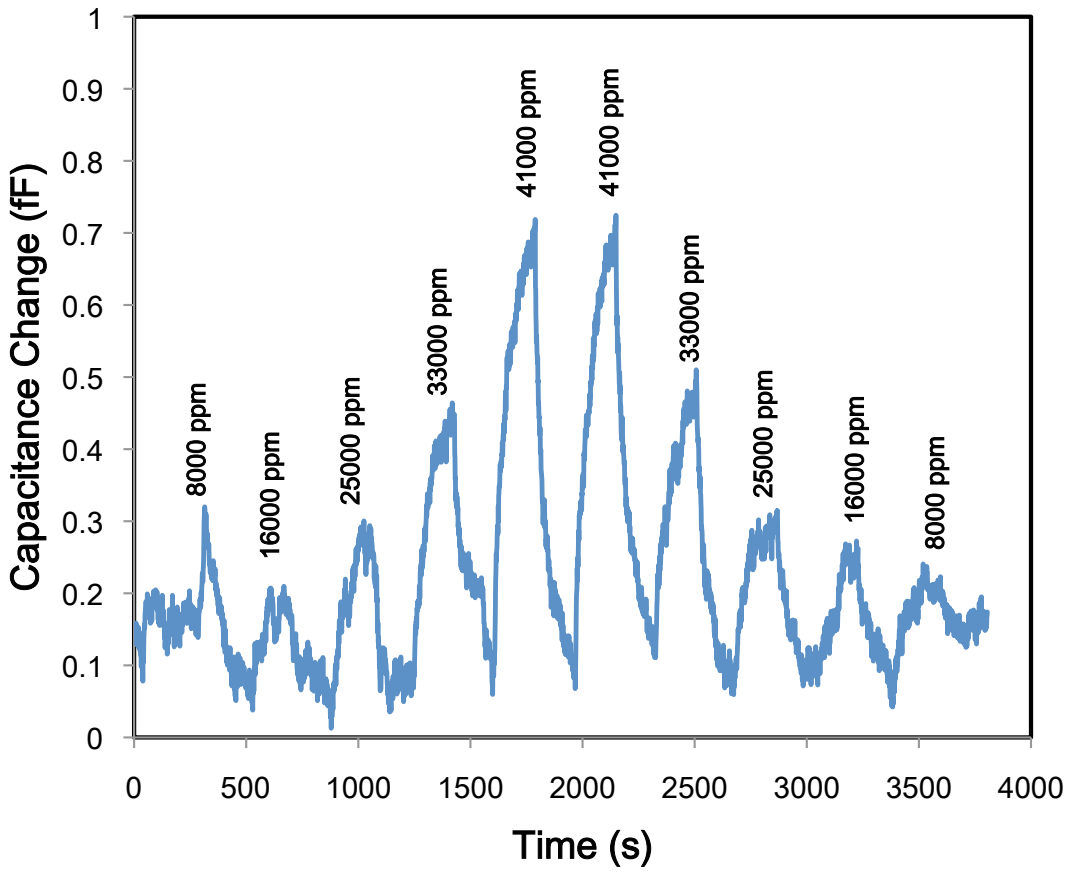

Figure 57: Measured capacitance change of the capacitive structure when exposed to several concentrations of ethanol vapor. The PIB thickness is 2.15 μm.

response for thick polymer layers (i.e. polymer layers greater than the electrode spacing). For a PIB thickness of 2.15 μm, the limits of detection for the toluene and ethanol vapors are 2300 ppm and 14700 ppm, respectively. This calculation is based on the responses to 16000 ppm of either vapor, as shown in Figure 59.

The toluene response shows a slight increase at the 2.15 μm PIB thickness, which is also consistent with a response due to the swelling effect [110]. The swelling effect will affect a larger response for layers on the order of the electrode spacing d (2 μm in this case). When $t_p > d$, the influence of the swelling effect on the capacitive response should then decrease monotonically.

Thus, for the specific system configuration explored in this research, the most visible capacitive response is the one due to the swelling effect. The capacitive response due to

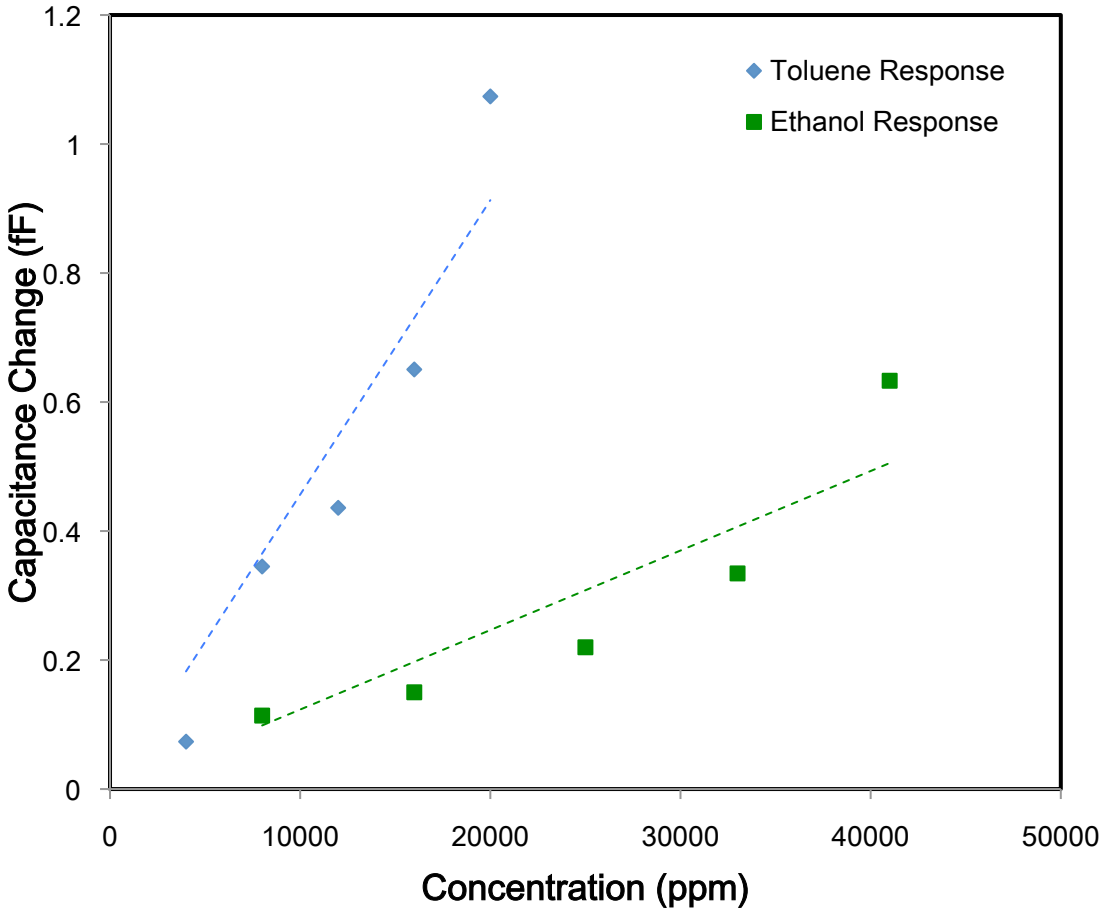

Figure 58: Calibration curves for the capacitive structure when exposed to toluene and ethanol vapor. The PIB thickness is 2.15 μm. The lines are a guide to the eye.

bulk dielectric changes appears to lie below the noise level for this specific implementation. Since the response due to bulk dielectric changes is the more immediately useful one for chemical sensing applications, the following section outlines various steps that can be taken to obtain the bulk dielectric response from analyte sorption.

5.7 Further Improvements

The sensing system developed around the capacitive structure can be further optimized to achieve better performance. The main difficulty with the current scheme is in obtaining a signal from the bulk dielectric effect due to analyte sorption. The results presented in this research show that the measured capacitive signal is mainly due to the swelling effect.

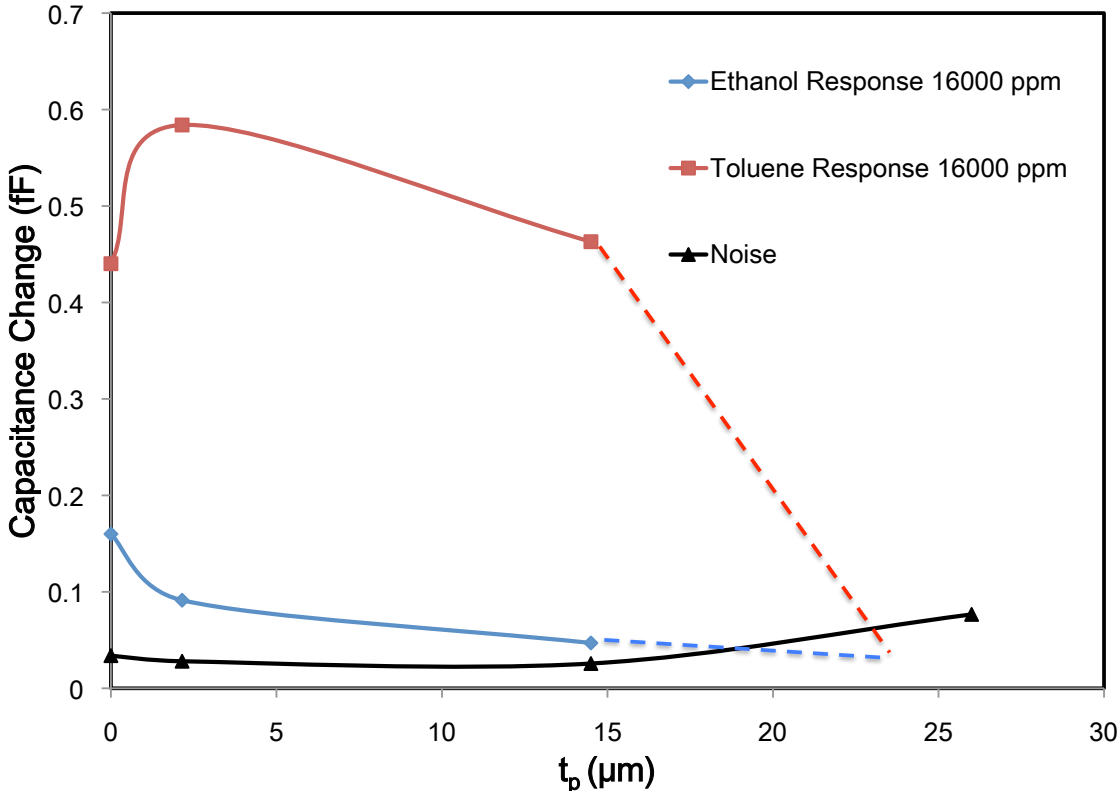

Figure 59: Capacitive responses to 16000 ppm of toluene and ethanol vapor as a function of PIB thickness t_p. The black line is the noise level of the sensor system. Both responses vanish into the noise before a PIB thickness of 26 μm.

There are three recommended approaches to fixing this, each with their own advantages and disadvantages.

- **Smaller Electrode Distance**. The magnitude of the capacitive signal is dependent on the magnitude of the baseline capacitance (see (74)). By decreasing the electrode distance, the baseline capacitance of the interdigitated electrodes can be increased. Additionally, smaller electrode distances allow the swelling effect to diminish at thinner polymer thicknesses. For the implementation of the full gravimetric-capacitive multisensor, this allows thinner polymer layers to be used, and thus the Q-factor of the resonator structure is preserved for the mass-sensing of chemical analytes. With the current fabrication process, this requires photolithography with smaller allowable feature sizes. For the mask sets used in this research, electrode structures with

distances below 2 μm could not be reliably fabricated.

- **Multisensor Array**. Another approach for increasing the baseline capacitance of the capacitor structure is to distribute a single capacitor structure across several cantilever structures to increase the capacitor size. Placing a single large capacitor on a single resonant structure would require a large resonant structure (potentially with dimensions on the order of millimeters with the current fabrication process). The distributed capacitor array approach would produce a large baseline capacitance without constraining the underlying resonant structures. The capacitor array approach is the most straightforward way to implement the multisensor with limited fabrication facilities, but does not overcome the problem of requiring thick polymer layers to reduce the influence of the swelling effect.

- **Integrated Readout Circuitry** The noise in the capacitive signal prevents the bulk dielectric effect from being observed in the appropriate polymer thickness regime. To reduce this noise, the use of readout circuitry integrated with the sensor structure is a possibility. For capacitive readout, a sigma-delta analog-to-digital converter is typically employed [49]. This approach would require access to a CMOS fabrication process.

5.8 Chapter Summary

This chapter presented characterization and VOC vapor sensing results for a gravimetric-capacitive multisensor platform. The platform consisted of a silicon resonator structure with a capacitive gold interdigitated electrode structure deposited on its topside. The platform was implemented using a modified version of the fabrication process described in Chapter 2.

The capacitive aspect of the system was characterized and the sensor was exposed to toluene and ethanol vapors. The results of these experiments have the following major points:

- The swelling effect, caused by electric field lines being captured and released by the

sensing layer during analyte sorption, is the dominant effect in the observed capacitive signal. For the electrode distance and baseline capacitance used (2 μm and $\approx$ 170 fF, respectively), the swelling effect appears to remain dominant for polymer thicknesses greater than 14 μm.

- The signal resulting from the bulk dielectric effect due to analyte sorption, which is the effect of greatest interest for chemical sensing, is below the noise level for the system used. The bulk dielectric effect should be observable when the influence of the swelling effect on the sensor signal has diminished at thick polymer thicknesses.

- Several strategies exist for obtaining a signal representing the bulk dielectric effect for the system investigated. These include a) using smaller electrode distances, b) distributing the capacitor structure onto several resonator structures in a multisensor array, and c) using integrated readout circuitry to reduce the noise in the capacitive signal.

CHAPTER VI

CONCLUSIONS AND OUTLOOK

6.1 Conclusions

The main objective of this research was to investigate the application of silicon disk microresonators as gas-phase VOC sensors, a critical application area in environmental monitoring. Gas-phase chemical testing of the disk resonators was performed, and characterization of the disk resonators was undertaken to support their optimization for gas-phase chemical sensing. Additionally, a gravimetric-capacitive multisensor structure was fabricated, characterized, and tested as a VOC vapor sensor. This section will summarize the underlying accomplishments for each of these areas of research. It will then be followed by sections describing the future outlook for each area.

The silicon disk resonators presented in this research were fabricated using a CMOS-compatible microfabrication process, allowing for future integration with CMOS readout circuitry. The silicon disk microresonators were characterized in terms of their Q-factor and the dynamic behavior of their rotational in-plane resonance mode. The Q-factor at atmospheric pressure for the rotational in-plane resonance mode of the disk resonators ranged from 2600 to 5600 for resonators with silicon thicknesses between 7 μm and 25 μm. The amount of viscous energy loss to the air for the disk resonators was found to be on the same order of magnitude as that of silicon microcantilevers with similar resonance frequencies. Due to the in-plane resonance mode of the disk resonators, the amount of viscous loss could be modulated by changing the resonator silicon thickness. It was also found that for the devices with the highest Q-factor in air, anchor losses become the dominant loss mechanism, indicating that future device optimization must consider anchor losses in addition to viscous losses.

The magnitude of the in-plane deflection of the disk resonator at its rotational in-plane resonance mode was measured using stroboscopic methods. For dynamic input excitation

powers ranging from 20.5 mW rms to 82.2 mW rms, this deflection ranged from 0.7 to 2.3 μm at the half-disk tip. When compared to the out-of-plane deflection of the rotational in-plane resonance mode for the same dynamic input power, the in-plane deflection is shown to be 100x greater than the out-of-plane deflection. This proves the effectiveness of the actuation scheme for the rotational in-plane resonance mode.

In the VOC vapor-sensing role, the disk resonators were coated with layers of PIB polymer, which acted as a sorbent film. The disk resonators were exposed to varying concentrations of toluene, benzene, and m-xylene using a custom gas manifold system. The minimal LODs for toluene, benzene, and m-xylene were extracted to be 1.2 ppm, 5.3 ppm, and 600 ppb, respectively. These LODs represent the state-of-the-art for VOC sensing using resonant gravimetric microsensors.

The chemical sensitivity and LOD of the disk resonators were modeled. Once the heating effect by the integrated excitation and sensing elements was considered, the chemical sensitivity and LOD models were found to predict the measured chemical sensitivity and LOD well. The dependence of resonator Allan variance on polymer thickness was found to be exponential in nature, which allowed the modeling of the LOD. Additionally, the optimal amount of static input power for minimizing LOD was found, balancing the needs of low temperature elevation and frequency noise.

Lastly, a gravimetric-capacitive multisensor was introduced. The multisensor consisted of a capacitive gold interdigitated electrode structure patterned on a silicon-based resonator structure. The multisensor structure was coated with PIB polymer and exposed to toluene and ethanol vapors. The capacitive response of the multisensor structure was demonstrated to be sensitive to the swelling-induced capacitance change from analyte sorption. Further optimization of the noise floor and baseline capacitance of the sensor is required to obtain the desired sensor response stemming from a change in dielectric properties. The baseline capacitance of the structure was estimated to be around 170 fF.

The following sections will present an outlook for the silicon disk resonator and the gravimetric-capacitive multisensor.

6.2 Outlook for the Silicon Disk Microresonators

The silicon disk microresonators presented in this research have been characterized in two different ways. First, the dynamic behavior of the disk resonator when operating in its rotational in-plane resonance mode was presented. Secondly, the chemical sensing behavior of the polymer-coated disk microresonator was presented. Both of these characterizations can collectively hint at the future directions to be taken with silicon disk microresonators in the chemical sensing application domain.

In Chapter 3, the silicon disk microresonators were characterized in terms of their Q-factor and their dynamic displacement in their rotational in-plane resonance mode. The rotational in-plane resonance mode has two distinct characteristics:

- The anchor loss for the rotational in-plane resonance mode of the silicon disk microresonator is invariant with the silicon thickness t_{si}. The anchor loss-limited Q-factor of the presented disk resonator is on the order of 10000.
- According to the theory of (26), the viscous loss $Q_{viscous}^{-1}$ decreases with the resonator silicon thickness t_{si}.

Using these two facts, it becomes apparent that an upper limit for Q-factor should exist for the silicon disk microresonators if the silicon thickness is increased. Figure 60 shows the measured Q-factor data of the rotational in-plane resonance mode in air for disk resonators of all lateral geometries with silicon thicknesses of 7 μm, 18 μm and 25 μm. Along with the data, the model of (26) is shown as a function of silicon thickness for a fixed frequency of 500 kHz and assuming a fluid ambient of air at atmospheric pressure. The frequency of 500 kHz lies in the middle of the range of resonance frequencies for the rotational in-plane mode of the tested disk resonators, and is chosen as a representative resonance frequency. The range of Q_{anchor} values from Figure 22 in Chapter 3 are also shown in Figure 60.

The rotational in-plane resonance modes of the disk resonators in this research have measured Q-factors below those predicted by the viscous damping theory of (26). The measured atmospheric Q-factor values appear to approach the anchor loss-limited Q-factors

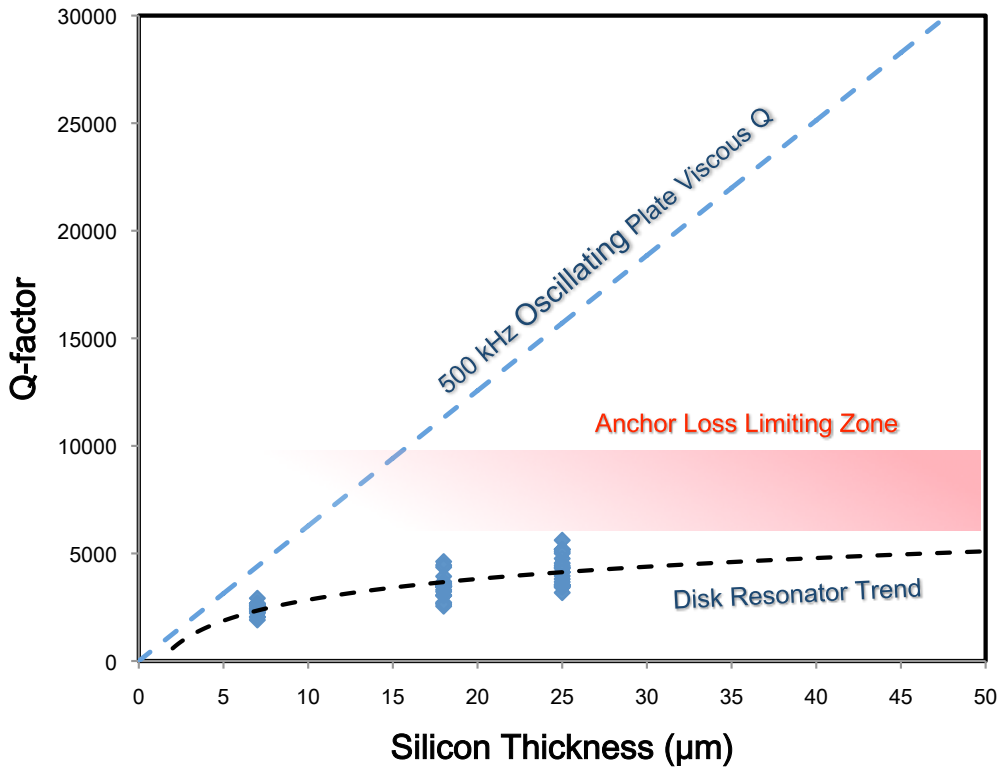

Figure 60: Q-factors of the rotational in-plane resonance mode of the silicon disk resonators as a function of resonator silicon thickness at atmosphere. All lateral geometries are represented. The model of (26) is presented as a function of resonator silicon thickness for a fixed frequency of 500 kHz. The anchor loss data of Chapter 3 shows the practical Q-factor limit.

for large silicon thicknesses. As mentioned before, this suggests that future optimization must at least include the anchor loss in addition to viscous losses. It should be noted that for operation in water, however, viscous losses will be by far the dominating loss mechanism.

The anchor-loss limited Q-factor of ≈ 10000 is mainly determined by the lateral geometry of the disk resonator. To a first order, either increasing the main anchor beam length L or decreasing the main anchor beam width w would help reduce the anchor loss and improve the maximum attainable Q-factor for the rotational in-plane resonance mode. For the research presented in this thesis, these lateral geometric parameters remain constant, and their optimization is a possible direction for future work. Alternatively, different in-plane resonance modes that minimize anchor loss could be explored.

For the case of viscous damping, the small but finite out-of-plane displacement of the

rotational in-plane resonance mode could also be further minimized to improve the Q-factor. This could be accomplished through the design of structures with out-of-plane resonance modes that are far-removed in frequency from the rotational in-plane resonance mode . This would possibly reduce the superposition of the out-plane mode shapes onto the rotational in-plane resonance mode, thus leading to a reduction in viscous damping associated with the out-of-plane displacement.

The above estimate for maximum Q-factor can serve as a quick way to quantify the predicted performance of the physical transducers without functionalization. The introduction of the polymer coating, however, demands the most attention and future investigation.

To an extent, the advantage of optimizing the Allan variance of the uncoated resonator for chemical sensing applications is questionable due to the effects of the polymer layer on the frequency noise of the resonator. In Chapter 4, PIB-coated disk resonators with the same lateral geometry but different silicon thicknesses were shown to achieve roughly the same minimal toluene LOD at the same PIB thickness t_{poly} of 2.6 μm. This invariance in the polymer thickness for minimal toluene LOD is attributed to the much faster degradation of the Allan variance, with increasing polymer thicknesses, for the thicker resonator, which had a lower initial Allan variance. This degradation seems to be better predicted by the absolute polymer thickness t_{poly} than the normalized polymer thickness $\frac{t_{Si}}{t_{poly}}$, which hints that the energy loss to the polymer layer deserves more in-depth modeling and investigation.

The amount of energy loss to the polymer layer could be minimized through the use of localized polymer deposition methods. In the presented research, the resonators were spray-coated with a polymer-solvent solution, resulting in a uniform polymer deposition across the entire device. All parts of the disk resonator that undergo deformation in the rotational in-plane resonance mode therefore transfer mechanical energy to the polymer layer, resulting in energy loss. By locally depositing polymer on select parts of the structure, it is predicted that much of the Q-factor decrease associated with uniform polymer coatings would be avoided. Figure 61 shows a conceptual image of a locally deposited polymer for the disk resonator. In addition to mitigating the Q-factor decrease, locally deposited polymers would also enable arrays of closely-packed transducers to be functionalized with different films.

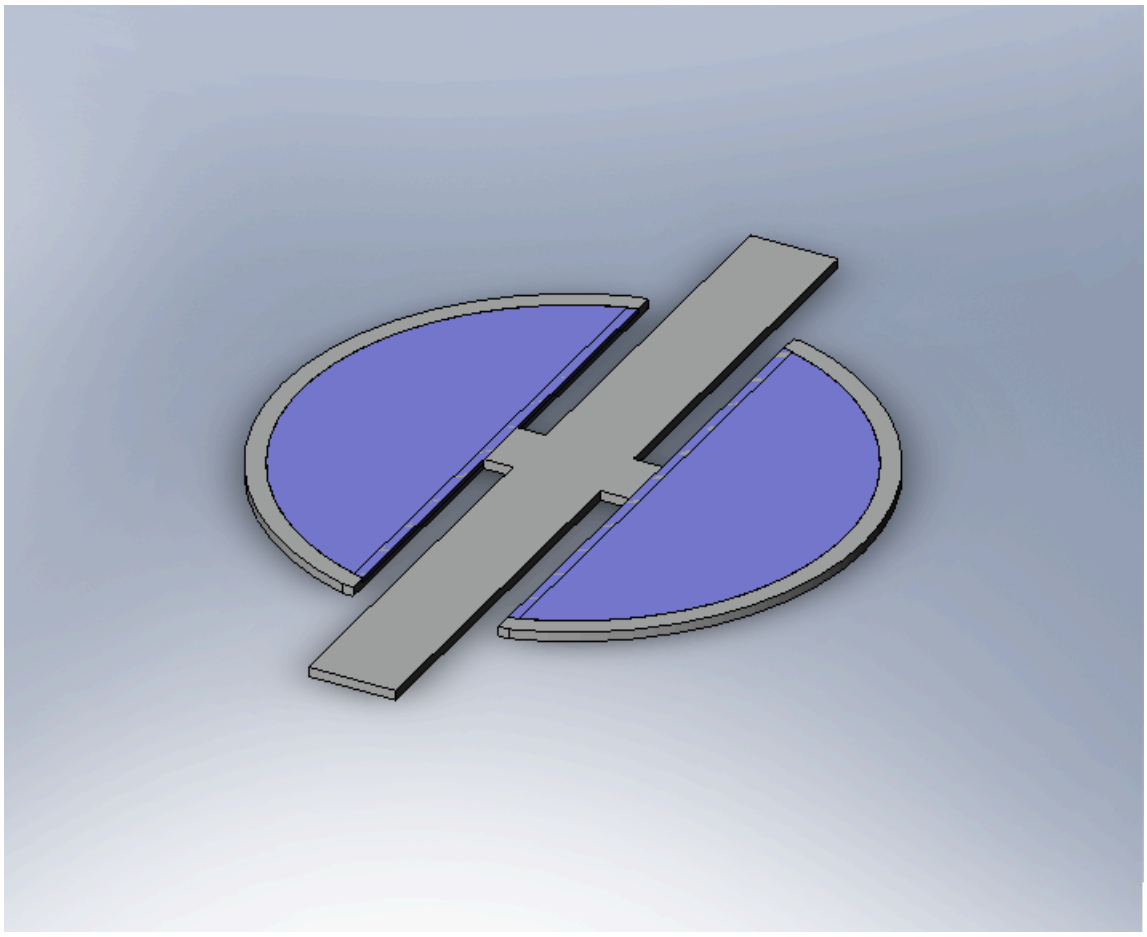

Figure 61: Concept of a locally-deposited polymer layer on the disk resonator. Blue areas represent the polymer.

Another immediate area for optimization is the reduction of heat dissipation on the surface of the silicon disk microresonator. In Chapter 4, it was shown that the experimentally measured chemical sensitivity was 3-5x below that of the ideal room temperature chemical sensitivity for the device tested. This was explained by the heat dissipation and resulting temperature elevation occurring on the surface of the disk due to the integrated excitation and sensing resistors. The optimal placement of the resistive elements for the chemical sensing application would be in a location where the polymer film is not affected by the heat dissipation associated with these elements. As an example, the temperature increase would be minimized if the resistive excitation and detection elements were located close to the thick silicon substrate, as in the case of the multisensor discussed in Chapter 5 (see

Figure 48).

If the optimizations described in the preceding paragraphs are carried to their maximal extent, low or single ppb LODs for the VOCs used in this research should be feasible with the disk resonator devices. This is based on the current chemical sensing performance of the disk resonators, which can detect m-xylene vapor with an LOD of 600 ppb. The optimizations, combined with the low power, batch fabrication, and CMOS integration capabilities of the silicon disk resonators described in this research, would make the disk devices potentially viable candidates as components in future miniaturized first-response VOC monitoring systems.

6.3 Outlook for the Gravimetric-Capacitive Multisensor

In Chapter 5, initial results demonstrating the fabrication feasibility and capacitive response of a gravimetric-capacitive multisensor were presented. The further development of this novel sensor concept relies on the solution to one or both of the following challenges

- Increasing the baseline capacitance of the capacitive sensor structure to illicit a larger capacitive output signal from bulk analyte sorption.
- Decreasing the noise floor of the capacitive sensor system and readout circuitry.

Although a response from swelling-induced changes in capacitance can be observed in the presented sensor response, the bulk dielectric change of the polymer sensing film cannot be detected due to the fact that it is below the noise floor of the capacitive readout IC used in this research. The use of an integrated capacitive readout IC could solve this problem, due to the generally reduced noise floor of integrated readout circuity placed on the same silicon die as the sensor structure. However, better results can be obtained with less engineering effort by increasing the capacitance of the sensor structure through smaller electrode distances or greater total capacitive area.

Based on calculation, capacitive responses on the order of fF for 16000 ppm of toluene vapor on a PECH-coated structure can be obtained for a capacitive sensor structure with a baseline capacitance on the order of picofarads. This would require the baseline capacitance

of the structures used in this research to be increased by 10x. Given that the surface area of the underlying gravimetric structure cannot be increased by such a factor, effort could be focused on the reduction of electrode distance to increase the capacitance of the multisensor structures used in this research. Alternatively, a capacitor structure distributed over several resonant structures could be implemented.

When realized, the gravimetric-capacitive multisensor has the potential to deliver greater sample analysis capability on a smaller sensor footprint by offering an analyte response based on multiple simultaneous transduction principles. Additionally, the added capability of humidity-based compensation signals provided by the capacitive structure is another promising possibility.

APPENDIX A

Q-FACTOR DATA FOR THE SILICON DISK RESONATORS AT ATMOSPHERE AND 2 μBAR

Silicon Thickness (μm)	**Outer Radius (μm)**	**Inner Radius (μm)**	**Resonance Frequency (Hz)**	**$Q_{atmosphere}$**	**$Q_{2\mu Bar}$**
7	130	0	756120	2367	5134
7	130	0	754270	1908	4340
7	130	50	737430	2057	3761
7	130	50	734340	2030	3662
7	150	0	536090	2430	3716
7	150	0	539065	2289	3096
7	150	0	537840	2222	2906
7	150	50	528710	2600	4384
7	150	50	526055	2457	4580
7	170	0	408710	2668	6336
7	170	50	395780	2917	6599
7	170	50	395020	2671	6568
7	200	0	280040	2578	6193
7	200	0	279520	2409	6378
7	200	50	271670	2519	6328

Silicon Thickness (μm)	**Outer Radius (μm)**	**Inner Radius (μm)**	**Resonance Frequency (Hz)**	**$Q_{atmosphere}$**	**$Q_{2\mu Bar}$**
18	130	0	760890	3456	7035
18	130	0	770160	3690	8373
18	130	50	742140	2721	3646
18	130	50	754320	3063	5631
18	150	0	539630	3222	4980
18	150	0	547200	2646	3486
18	150	50	531780	3496	6081
18	150	50	539947	3031	4321
18	170	0	407860	4456	11088
18	170	0	422430	4360	11890
18	170	0	412861	4621	11839
18	170	50	411434	3933	11730
18	170	50	398297	2549	6635
18	170	50	404620	3467	7980
18	200	0	281950	3456	8382
18	200	0	292209	3614	8770
18	200	0	288210	3487	7258
18	200	50	276930	3313	7469
18	200	50	283990	3575	8973
18	200	50	282430	3499	7128

APPENDIX B

Q-FACTOR DATA FOR SILICON CANTILEVERS AT ATMOSPHERE AND 2 μBAR

Silicon Thickness (μm)	**Length (μm)**	**Width (μm)**	**Fundamental In-plane Resonance Frequency (Hz)**	**$Q_{atmosphere}$**	**$Q_{2\mu Bar}$**
8.3	400	45	349080	3026	11215
8.3	800	45	89259	1039	9397
8.3	1000	45	60590	1247	7870
21.5	200	45	1242745	3397	8260
21.5	400	45	338500	2810	10827
21.5	800	45	91135	1499	7690
21.5	1000	45	58590	1206	7981
20.9	400	60	436920	3032	7392
20.9	400	90	636281	3143	5686
20.9	800	60	120490	2190	10953
20.4	800	90	179622	1140	1688
20.9	1000	60	76414	1597	9605
20.9	1000	90	114060	2308	12003

Silicon Thickness (μm)	**Length (μm)**	**Width (μm)**	**Fundamental Out-of-plane Resonance Frequency (Hz)**	$\mathbf{Q_{atmosphere}}$	$\mathbf{Q_{2\mu Bar}}$
8.3	200	45	674212	1450	2245
8.3	400	45	145715	1158	3207
8.3	1000	45	26773	719	11579
21.5	200	45	568610	1554	2364
21.5	400	45	142300	1147	2998
21.5	800	45	40430	665	11425
21.5	1000	45	25640	506	16689
20.9	200	60	559382	1034	1443
20.9	400	60	140802	962	1838
20.9	800	60	41409	952	9297
20.4	800	90	42548	1040	9743
20.9	1000	60	25356	657	6050
20.9	1000	90	27280	839	8120

REFERENCES

[1] J. Janata, M. Josowicz, P. Vanysek, and D. M. DeVaney, "Chemical sensors," *Analytical Chemistry*, vol. 70, no. 12, pp. 179–208, 1998.

[2] (2011) List of hazardous air pollutants. [Online]. Available: http://www.epa.gov/ttn/atw/orig189.html

[3] (2011) Toluene. [Online]. Available: http://www.epa.gov/ttnatw01/hlthef/toluene.html

[4] (2011) Benzene. [Online]. Available: http://www.epa.gov/ttnatw01/hlthef/benzene.html

[5] (2011) Xylenes. [Online]. Available: http://www.epa.gov/ttnatw01/hlthef/xylenes.html

[6] J. M. Daisey, A. T. Hodgson, W. J. Fisk, M. J. Mendell, and J. Ten Brinke, "Volatile organic compounds in twelve california office buildings: Classes, concentrations and sources," *Atmospheric Environment*, vol. 28, no. 22, pp. 3557–3562, 1994.

[7] C. W. Spicer, B. E. Buxton, M. W. Holdren, D. L. Smith, T. J. Kelly, S. W. Rust, A. D. Pate, G. M. Sverdrup, and J. C. Chuang, "Variability of hazardous air pollutants in an urban area," *Atmospheric Environment*, vol. 30, no. 20, pp. 3443–3456, 1996.

[8] S. N. Matsunaga, S. Chatani, T. Morikawa, S. Nakatsuka, J. Suthawaree, Y. Tajima, S. Kato, Y. Kajii, and H. Minoura, "Evaluation of non-methane hydrocarbon (nmhc) emissions based on an ambient air measurement in tokyo area, japan," *Atmospheric Environment*, vol. 44, no. 38, pp. 4982–4993, 2010.

[9] N. K. Tran, S. M. Steinberg, and B. J. Johnson, "Volatile aromatic hydrocarbons and dicarboxylic acid concentrations in air at an urban site in the southwestern us," *Atmospheric Environment*, vol. 34, no. 11, pp. 1845–1852, 2000.

[10] S. P. Karakitsios, V. K. Delis, P. A. Kassomenos, and G. A. Pilidis, "Contribution to ambient benzene concentrations in the vicinity of petrol stations: Estimation of the associated health risk," *Atmospheric Environment*, vol. 41, no. 9, pp. 1889–1902, 2007.

[11] H. Bravo, R. Sosa, P. Snchez, E. Bueno, and L. Gonzlez, "Concentrations of benzene and toluene in the atmosphere of the southwestern area at the mexico city metropolitan zone," *Atmospheric Environment*, vol. 36, no. 23, pp. 3843–3849, 2002.

[12] C.-C. Chan, S.-H. Lin, and G.-R. Her, "Office workers's exposure to volatile organic compounds while commuting and working in taipei city," *Atmospheric Environment*, vol. 28, no. 14, pp. 2351–2359, 1994.

[13] *Code of Federal Regulations, 40 , Maximum contaminant level goals for organic contaminants, 141.50.* Office of the Federal Register, 2004.

[14] S. A. Ramsey, R. V. Mustacich, P. A. Smith, G. L. Hook, and B. A. Eckenrode, "Directly heated high surface area solid phase microextraction sampler for rapid field forensic analyses," *Analytical Chemistry*, vol. 81, no. 21, pp. 8724–8733, 2009.

[15] N. Yamamoto, T. Matsubasa, N. Kumagai, S. Mori, and K. Suzuki, "A diffusive badge sampler for volatile organic compounds in ambient air and determination using a thermal desorption-gc/ms system," *Analytical Chemistry*, vol. 74, no. 2, pp. 484–487, 2001.

[16] H. A. Soini, K. E. Bruce, I. Klouckova, R. G. Brereton, D. J. Penn, and M. V. Novotny, "In situ surface sampling of biological objects and preconcentration of their volatiles for chromatographic analysis," *Analytical Chemistry*, vol. 78, no. 20, pp. 7161–7168, 2006.

[17] F. L. Dorman, J. J. Whiting, J. W. Cochran, and J. Gardea-Torresdey, "Gas chromatography," *Analytical Chemistry*, vol. 82, no. 12, pp. 4775–4785, 2010.

[18] (2011) Sampling and analytical methods: Benzene. [Online]. Available: http://www.osha.gov/dts/sltc/methods/organic/org012/org012.html

[19] (2011) Sampling and analytical methods: Toluene. [Online]. Available: http://www.osha.gov/dts/sltc/methods/organic/org111/org111.html

[20] (2011) Sampling and analytical methods: Xylenes (o-, m-, p-isomers). [Online]. Available: http://www.osha.gov/dts/sltc/methods/mdt/mdt1002/1002.html

[21] "Phone inquiries," Personal Communication.

[22] A. Hierlemann and R. Gutierrez-Osuna, "Higher-order chemical sensing," *Chemical Reviews*, vol. 108, no. 2, pp. 563–613, 2008.

[23] C. McDonagh, C. S. Burke, and B. D. MacCraith, "Optical chemical sensors," *Chemical Reviews*, vol. 108, no. 2, pp. 400–422, 2008.

[24] B. Mizaikoff, "Peer reviewed: Mid-ir fiber-optic sensors," *Analytical Chemistry*, vol. 75, no. 11, pp. 258 A–267 A, 2003.

[25] O. S. Wolfbeis, "Fiber-optic chemical sensors and biosensors," *Analytical Chemistry*, vol. 80, no. 12, pp. 4269–4283, 2008.

[26] M. Karlowatz, M. Kraft, and B. Mizaikoff, "Simultaneous quantitative determination of benzene, toluene, and xylenes in water using mid-infrared evanescent field spectroscopy," *Analytical Chemistry*, vol. 76, no. 9, pp. 2643–2648, 2004.

[27] M. Lamotte, P. de Violet, P. Garrigues, and M. Hardy, "Evaluation of the possibility of detecting benzenic pollutants by direct spectrophotometry on pdms solid sorbent," *Analytical and Bioanalytical Chemistry*, vol. 372, no. 1, pp. 169–173, 2002.

[28] P. Kurzawski, C. Hagleitner, and A. Hierlemann, "Detection and discrimination capabilities of a multitransducer single-chip gas sensor system," *Analytical Chemistry*, vol. 78, no. 19, pp. 6910–6920, 2006.

[29] J. Lerchner, D. Caspary, and G. Wolf, "Calorimetric detection of volatile organic compounds," *Sensors and Actuators B: Chemical*, vol. 70, no. 1-3, pp. 57–66, 2000.

[30] W. H. King, "Piezoelectric sorption detector," *Analytical Chemistry*, vol. 36, no. 9, pp. 1735–1739, 1964.

[31] R. J. Lipert, R. Shinar, B. Vaidya, A. D. Pris, M. D. Porter, G. Liu, T. D. Grabau, and J. P. Dilger, "Thin films of block copolymer blends for enhanced performance of acoustic wave-based chemical sensors," *Analytical Chemistry*, vol. 74, no. 24, pp. 6383–6391, 2002.

[32] J. D. N. Cheeke and Z. Wang, "Acoustic wave gas sensors," *Sensors and Actuators B: Chemical*, vol. 59, no. 2-3, pp. 146–153, 1999.

[33] S. J. Martin, A. J. Ricco, T. M. Niemczyk, and G. C. Frye, "Characterization of sh acoustic plate mode liquid sensors," *Sensors and Actuators*, vol. 20, no. 3, pp. 253–268, 1989.

[34] R. Patel, R. Zhou, K. Zinszer, F. Josse, and R. Cernosek, "Real-time detection of organic compounds in liquid environments using polymer-coated thickness shear mode quartz resonators," *Analytical Chemistry*, vol. 72, no. 20, pp. 4888–4898, 2000.

[35] Z. Li, Y. Jones, J. Hossenlopp, R. Cernosek, and F. Josse, "Analysis of liquid-phase chemical detection using guided shear horizontal-surface acoustic wave sensors," *Analytical Chemistry*, vol. 77, no. 14, pp. 4595–4603, 2005.

[36] K. Bodenhöfer, A. Hierlemann, G. Noetzel, U. Weimar, and W. Göpel, "Performances of mass-sensitive devices for gas sensing: thickness shear mode and surface acoustic wave transducers," *Analytical Chemistry*, vol. 68, no. 13, pp. 2210–2218, 1996.

[37] A. Hierlemann, D. Lange, C. Hagleitner, N. Kerness, A. Koll, O. Brand, and H. Baltes, "Application-specific sensor systems based on cmos chemical microsensors," *Sensors and Actuators B: Chemical*, vol. 70, no. 1-3, pp. 2–11, 2000.

[38] A. Boisen, J. Thaysen, H. Jensenius, and O. Hansen, "Environmental sensors based on micromachined cantilevers with integrated read-out," *Ultramicroscopy*, vol. 82, no. 1-4, pp. 11–16, 2000.

[39] J. Fritz, M. K. Baller, H. P. Lang, H. Rothuizen, P. Vettiger, E. Meyer, H. J. Güntherodt, C. Gerber, and J. K. Gimzewski, "Translating biomolecular recognition into nanomechanics," *Science*, vol. 288, no. 5464, pp. 316–318, 2000.

[40] P. Li, X. Li, G. Zuo, J. Liu, Y. Wang, M. Liu, and D. Jin, "Silicon dioxide microcantilever with piezoresistive element integrated for portable ultraresoluble gaseous detection," *Applied Physics Letters*, vol. 89, no. 7, p. 074104, 2006.

[41] P. Li and X. Li, "A single-sided micromachined piezoresistive sio2 cantilever sensor for ultra-sensitive detection of gaseous chemicals," *Journal of Micromechanics and Microengineering*, no. 12, p. 2539, 2006.

[42] Y. T. Yang, C. Callegari, X. L. Feng, K. L. Ekinci, and M. L. Roukes, "Zeptogram-scale nanomechanical mass sensing," *Nano Letters*, vol. 6, no. 4, pp. 583–586, 2006.

[43] I. Voiculescu, M. E. Zaghloul, R. A. McGill, E. J. Houser, and G. K. Fedder, "Electrostatically actuated resonant microcantilever beam in cmos technology for the detection of chemical weapons," *Sensors Journal, IEEE*, vol. 5, no. 4, pp. 641–647, 2005.

[44] A. Qazi, D. Nonis, A. Pozzato, M. Tormen, M. Lazzarino, S. Carrato, and G. Scoles, "Asymmetrical twin cantilevers for single molecule detection," *Applied Physics Letters*, vol. 90, no. 17, pp. 173 118–3, 2007.

[45] D. Lange, C. Hagleitner, A. Hierlemann, O. Brand, and H. Baltes, "Complementary metal oxide semiconductor cantilever arrays on a single chip: Mass-sensitive detection of volatile organic compounds," *Analytical Chemistry*, vol. 74, no. 13, pp. 3084–3095, 2002.

[46] C. Vancura, Y. Li, J. Lichtenberg, K.-U. Kirstein, A. Hierlemann, and F. Josse, "Liquid-phase chemical and biochemical detection using fully integrated magnetically actuated complementary metal oxide semiconductor resonant cantilever sensor systems," *Analytical Chemistry*, vol. 79, no. 4, pp. 1646–1654, 2007.

[47] S. Joo and R. B. Brown, "Chemical sensors with integrated electronics," *Chemical Reviews*, vol. 108, no. 2, pp. 638–651, 2008.

[48] H. Baltruschat, I. Kamphausen, R. Oelgeklaus, J. Rose, and M. Wahlkamp, "Detection of volatile organic solvents using potentiodynamic gas sensors," *Analytical Chemistry*, vol. 69, no. 4, pp. 743–748, 1997.

[49] A. M. Kummer, A. Hierlemann, and H. Baltes, "Tuning sensitivity and selectivity of complementary metal oxide semiconductor-based capacitive chemical microsensors," *Analytical Chemistry*, vol. 76, no. 9, pp. 2470–2477, 2004.

[50] S. V. Patel, T. E. Mlsna, B. Fruhberger, E. Klaassen, S. Cemalovic, and D. R. Baselt, "Chemicapacitive microsensors for volatile organic compound detection," *Sensors and Actuators B: Chemical*, vol. 96, no. 3, pp. 541–553, 2003.

[51] (2011) Product listing. [Online]. Available: http://www.figarosensor.com/gaslist.html

[52] M. C. Lonergan, E. J. Severin, B. J. Doleman, S. A. Beaber, R. H. Grubbs, and N. S. Lewis, "Array-based vapor sensing using chemically sensitive, carbon black polymer resistors," *Chemistry of Materials*, vol. 8, no. 9, pp. 2298–2312, 1996.

[53] F. I. Bohrer, E. Covington, C. Kurdak, and E. T. Zellers, "Characterization of dense arrays of chemiresistor vapor sensors with submicrometer features and patterned nanoparticle interface layers," *Analytical Chemistry*, vol. 83, no. 10, pp. 3687–3695, 2011.

[54] F. Rock, N. Barsan, and U. Weimar, "Electronic nose: Current status and future trends," *Chemical Reviews*, vol. 108, no. 2, pp. 705–725, 2008.

[55] T. K. Alkasab, J. White, and J. S. Kauer, "A computational system for simulating and analyzing arrays of biological and artificial chemical sensors," *Chem. Senses*, vol. 27, no. 3, pp. 261–275, 2002.

[56] J. Park, W. A. Groves, and E. T. Zellers, "Vapor recognition with small arrays of polymer-coated microsensors. a comprehensive analysis," *Analytical Chemistry*, vol. 71, no. 17, pp. 3877–3886, 1999.

[57] C. Hagleitner, A. Hierlemann, D. Lange, A. Kummer, N. Kerness, O. Brand, and H. Baltes, "Smart single-chip gas sensor microsystem," *Nature*, vol. 414, no. 6861, pp. 293–296, 2001.

[58] M. Penza, G. Cassano, P. Aversa, F. Antolini, A. Cusano, M. Consales, M. Giordano, and L. Nicolais, "Carbon nanotubes-coated multi-transducing sensors for vocs detection," *Sensors and Actuators B: Chemical*, vol. 111-112, pp. 171–180, 2005.

[59] Y. Kunugi, K. Nigorikawa, Y. Harima, and k. Yamashita, "A selective organic vapour sensor based on simultaneous measurements of changes of mass and resistance of a poly(pyrrole) thin film," *Journal of the Chemical Society, Chemical Communications*, pp. 873 – 874, 1994.

[60] C. Jin, P. Kurzawski, A. Hierlemann, and E. T. Zellers, "Evaluation of multitransducer arrays for the determination of organic vapor mixtures," *Analytical Chemistry*, vol. 80, no. 1, pp. 227–236, 2008.

[61] N. V. Lavrik, M. J. Sepaniak, and P. G. Datskos, "Cantilever transducers as a platform for chemical and biological sensors," *Review of Scientific Instruments*, vol. 75, no. 7, pp. 2229–2253, 2004.

[62] X. Xia, Z. Zhang, and X. Li, "A latin-cross-shaped integrated resonant cantilever with second torsion-mode resonance for ultra-resoluble bio-mass sensing," *Journal of Micromechanics and Microengineering*, no. 3, p. 035028, 2008.

[63] D. Jin, X. Li, H. Bao, Z. Zhang, Y. Wang, H. Yu, and G. Zuo, "Integrated cantilever sensors with a torsional resonance mode for ultraresoluble on-the-spot bio/chemical detection," *Applied Physics Letters*, vol. 90, no. 4, pp. 041 901–3, 2007.

[64] S. E. Alper and T. Akin, "A single-crystal silicon symmetrical and decoupled mems gyroscope on an insulating substrate," *Microelectromechanical Systems, Journal of*, vol. 14, no. 4, pp. 707–717, 2005.

[65] M. F. Zaman, A. Sharma, H. Zhili, and F. Ayazi, "A mode-matched silicon-yaw tuning-fork gyroscope with subdegree-per-hour allan deviation bias instability," *Microelectromechanical Systems, Journal of*, vol. 17, no. 6, pp. 1526–1536, 2008.

[66] (2011) 330400/330425 accelerometers. [Online]. Available: http://www.ge-mcs.com/en/bently-nevada-sensors-and-transducers/acceleration-and-velocity/330400-330425-accelerometers.html

[67] (2011) Rpt350. [Online]. Available: http://www.ge-mcs.com/en/pressure-and-level/transducerstransmitters/rtp350.html

[68] J. Ginsberg, *Mechanical and Structural Vibrations*. New York: John Wiley & Sons, 2001.

[69] S. B. Truax, K. S. Demirci, L. A. Beardslee, Y. Luzinova, A. Hierlemann, B. Mizaikoff, and O. Brand, "Mass-sensitive detection of gas-phase volatile organics using disk microresonators," *Analytical Chemistry*, vol. 83, no. 9, pp. 3305–3311, 2011.

[70] L. Fadel, I. Dufour, F. Lochon, and O. Francais, "Signal-to-noise ratio of resonant microcantilever type chemical sensors as a function of resonant frequency and quality factor," *Sensors and Actuators B: Chemical*, vol. 102, no. 1, pp. 73–77, 2004.

[71] J. H. Seo and O. Brand, "High q-factor in-plane-mode resonant microsensor platform for gaseous/liquid environment," *Microelectromechanical Systems, Journal of*, vol. 17, no. 2, pp. 483–493, 2008.

[72] I. Bargatin, I. Kozinsky, and M. L. Roukes, "Efficient electrothermal actuation of multiple modes of high-frequency nanoelectromechanical resonators," *Applied Physics Letters*, vol. 90, no. 9, p. 093116, 2007.

[73] K. Naeli and O. Brand, "Dimensional considerations in achieving large quality factors for resonant silicon cantilevers in air," *Journal of Applied Physics*, vol. 105, no. 1, p. 014908, 2009.

[74] J.-H. Seo, "Silicon-based resonant microsensor platform for chemical and biological applications," Ph.D. dissertation, Georgia Institute of Technology, 2008.

[75] K. S. Demirci, J. H. Seo, S. Truax, L. A. Beardslee, Y. Luzinova, B. Mizaikoff, and O. Brand, "Frequency drift compensation in mass-sensitive chemical sensors based on periodic stiffness modulation," in *Micro Electro Mechanical Systems, 2009. MEMS 2009. IEEE 22nd International Conference on*, 2009, pp. 284–287.

[76] C. Zener, "Internal friction in solids. i. theory of internal friction in reeds," *Physical Review*, vol. 52, no. 3, p. 230, 1937.

[77] T. R. Albrecht, P. Grutter, D. Horne, and D. Rugar, "Frequency modulation detection using high-q cantilevers for enhanced force microscope sensitivity," *Journal of Applied Physics*, vol. 69, no. 2, pp. 668–673, 1991.

[78] T. H. Stievater, W. S. Rabinovich, N. A. Papanicolaou, R. Bass, and J. B. Boos, "Measured limits of detection based on thermal-mechanical frequency noise in micromechanical sensors," *Applied Physics Letters*, vol. 90, no. 5, pp. 051 114–3, 2007.

[79] I. Dufour, F. Lochon, S. M. Heinrich, F. Josse, and D. Rebiere, "Effect of coating viscoelasticity on quality factor and limit of detection of microcantilever chemical sensors," *Sensors Journal, IEEE*, vol. 7, no. 2, pp. 230–236, 2007.

[80] R. Panton, *Incompressible Flow*, 3rd ed. New York: John Wiley & Sons, 2005.

[81] L. Landau, *Fluid Mechanics*, 2nd ed. Oxford: Pergammon Press, 1987.

[82] H. Lamb, *Hydrodynamics*, 5th ed. London: Cambridge University Press, 1930.

[83] R. Cox, F. Josse, S. Heinrich, I. Dufour, and O. Brand, "Resonant microcantilevers vibrating laterally in viscous liquid media," in *Frequency Control Symposium (FCS), 2010 IEEE International*, 2010, pp. 85–90.

[84] F. R. Blom, S. Bouwstra, M. Elwenspoek, and J. H. J. Fluitman, "Dependence of the quality factor of micromachined silicon beam resonators on pressure and geometry," *Journal of Vacuum Science & Technology B: Microelectronics and Nanometer Structures*, vol. 10, no. 1, pp. 19–26, 1992.

[85] J. E. Sader, "Frequency response of cantilever beams immersed in viscous fluids with applications to the atomic force microscope," *Journal of Applied Physics*, vol. 84, no. 1, pp. 64–76, 1998.

[86] G. G. Stokes, "On the effect of the internal friction of fluids on the motion of pendulums," *Transactions of the Cambridge Philisophical Society*, vol. 9, pp. 8–106, 1851.

[87] C. Young-Ho, A. P. Pisano, and R. T. Howe, "Viscous damping model for laterally oscillating microstructures," *Microelectromechanical Systems, Journal of*, vol. 3, no. 2, pp. 81–87, 1994.

[88] I. Dufour, S. M. Heinrich, and F. Josse, "Theoretical analysis of strong-axis bending mode vibrations for resonant microcantilever (bio)chemical sensors in gas or liquid phase," *Microelectromechanical Systems, Journal of*, vol. 16, no. 1, pp. 44–49, 2007.

[89] B. Weiss, E. K. Reichel, and B. Jakoby, "Modeling of a clamped-clamped beam vibrating in a fluid for viscosity and density sensing regarding compressibility," *Sensors and Actuators A: Physical*, vol. 143, no. 2, pp. 293–301, 2008.

[90] A. Maali, C. Hurth, R. Boisgard, C. Jai, T. Cohen-Bouhacina, and J.-P. Aim, "Hydrodynamics of oscillating atomic force microscopy cantilevers in viscous fluids," *Journal of Applied Physics*, vol. 97, 2005.

[91] H. Hosaka, K. Itao, and S. Kuroda, "Damping characteristics of beam-shaped micro-oscillators," *Sensors and Actuators A: Physical*, vol. 49, no. 1-2, pp. 87–95, 1995.

[92] Y. Jinling, T. Ono, and M. Esashi, "Energy dissipation in submicrometer thick single-crystal silicon cantilevers," *Microelectromechanical Systems, Journal of*, vol. 11, no. 6, pp. 775–783, 2002.

[93] Z. Hao, A. Erbil, and F. Ayazi, "An analytical model for support loss in micromachined beam resonators with in-plane flexural vibrations," *Sensors and Actuators A: Physical*, vol. 109, no. 1-2, pp. 156–164, 2003.

[94] M. C. Cross and R. Lifshitz, "Elastic wave transmission at an abrupt junction in a thin plate with application to heat transport and vibrations in mesoscopic systems," *Physical Review B*, vol. 64, no. 8, p. 085324, 2001.

[95] D. M. Photiadis and J. A. Judge, "Attachment losses of high q oscillators," *Applied Physics Letters*, vol. 85, no. 3, pp. 482–484, 2004.

[96] C. Heer, *Statistical Mechanics, Kinetic Theory, and Stochastic Processes*. New York: Academic Press, 1972.

[97] A. N. Cleland and M. L. Roukes, "Noise processes in nanomechanical resonators," *Journal of Applied Physics*, vol. 92, no. 5, pp. 2758–2769, 2002.

[98] D. Allan, H. Hellwig, P. Kartaschoff, J. Vanier, J. Vig, G. M. R. Winkler, and N. F. Yannoni, *Standard terminology for fundamental frequency and time metrology*, 1988, pp. 419–425.

[99] E. A. Gerber, *Oscillators and Standards*, ser. Precision Frequency Control. Academic Press, 1985, vol. 2.

[100] D. W. Allan, "Statistics of atomic frequency standards," *Proceedings of the IEEE*, vol. 54, no. 2, pp. 221–230, 1966.

[101] L. A. Beardslee, A. M. Addous, S. Heinrich, F. Josse, I. Dufour, and O. Brand, "Thermal excitation and piezoresistive detection of cantilever in-plane resonance modes for sensing applications," *Microelectromechanical Systems, Journal of*, vol. 19, no. 4, pp. 1015–1017, 2010.

[102] T. S. J. Lammerink, M. Elwenspoek, and J. H. J. Fluitman, "Frequency dependence of thermal excitation of micromechanical resonators," *Sensors and Actuators A: Physical*, vol. 27, no. 1-3, pp. 685–689, 1991.

[103] A. Hierlemann, A. J. Ricco, K. Bodenhöfer, and W. Göpel, "Effective use of molecular recognition in gas sensing: Results from acoustic wave and in situ ft-ir measurements," *Analytical Chemistry*, vol. 71, no. 15, pp. 3022–3035, 1999.

[104] S. J. Patrash and E. T. Zellers, "Characterization of polymeric surface acoustic wave sensor coatings and semiempirical models of sensor responses to organic vapors," *Analytical Chemistry*, vol. 65, no. 15, pp. 2055–2066, 1993.

[105] A. Hierlemann, E. T. Zellers, and A. J. Ricco, "Use of linear solvation energy relationships for modeling responses from polymer-coated acoustic-wave vapor sensors," *Analytical Chemistry*, vol. 73, no. 14, pp. 3458–3466, 2001.

[106] P. A. Martos, A. Saraullo, and J. Pawliszyn, "Estimation of air/coating distribution coefficients for solid phase microextraction using retention indexes from linear temperature-programmed capillary gas chromatography. application to the sampling and analysis of total petroleum hydrocarbons in air," *Analytical Chemistry*, vol. 69, no. 3, pp. 402–408, 1997.

[107] Y. K. Jones, L. Zhonghui, M. M. Johnson, F. Josse, and J. M. Hossenlopp, "Atr-ftir spectroscopic analysis of sorption of aqueous analytes into polymer coatings used with guided sh-saw sensors," *Sensors Journal, IEEE*, vol. 5, no. 6, pp. 1175–1184, 2005.

[108] J. W. Grate, S. N. Kaganove, and V. R. Bhethanabotla, "Comparisons of polymer/gas partition coefficients calculated from responses of thickness shear mode and surface acoustic wave vapor sensors," *Analytical Chemistry*, vol. 70, no. 1, pp. 199–203, 1998.

[109] A. Hierlemann, A. J. Ricco, K. Bodenhöfer, A. Dominik, and W. Göpel, "Conferring selectivity to chemical sensors via polymer side-chain selection: Thermodynamics of vapor sorption by a set of polysiloxanes on thickness-shear mode resonators," *Analytical Chemistry*, vol. 72, no. 16, pp. 3696–3708, 2000.

[110] A. Kummer, "Tuning sensitivity and discrimination performance of cmos capacitive chemical microsensor systems," Ph.D. dissertation, ETH Zurich, 2004.

[111] S. Truax, K. S. Demirci, A. Hierlemann, and O. Brand, "Exploring the resolution of different disk-type chemical sensors," in *Solid-State Sensors, Actuators and Microsystems Conference, 2009. TRANSDUCERS 2009. International*, 2009, pp. 1838–1841.

[112] A. Weissberger, *Organic Solvents Volume II*, 4th ed. New York: Wiley, 1986.

[113] J. Comyn, *Polymer Permeability*. Essex: Elsevier Applied Science, 1985.

[114] K. W. Misevich, "Capacitive humidity transducer," *Industrial Electronics and Control Instrumentation, IEEE Transactions on*, vol. IECI-16, no. 1, pp. 6–12, 1969.

[115] N. F. Sheppard, D. R. Day, H. L. Lee, and S. D. Senturia, "Microdielectrometry," *Sensors and Actuators*, vol. 2, pp. 263–274, 1981.

[116] T. Boltshauser and H. Baltes, "Capacitive humidity sensors in sacmos technology with moisture absorbing photosensitive polyimide," *Sensors and Actuators A: Physical*, vol. 26, no. 1-3, pp. 509–512, 1991.

[117] (2011) Ms3110 universal capacitive readout ic datasheet. [Online]. Available: http://www.irvine-sensors.com/pdf/MS3110%20Datasheet%20USE.pdf